

FINITE ELEMENT MODELING OF BALLSCREW FEED DRIVE SYSTEMS FOR
CONTROL PURPOSES

by

CHINEDUM OKWUDIRE

B.Sc. (Mechanical Engineering)

Middle East Technical University

A THESIS SUBMITTED IN PARTIAL FULFILLMENT OF

THE REQUIREMENTS FOR THE DEGREE OF

MASTER OF APPLIED SCIENCE

in

THE FACULTY OF GRADUATE STUDIES

(MECHANICAL ENGINEERING)

THE UNIVERSITY OF BRITISH COLUMBIA

September, 2005

© Chinedum Okwudire, 2005

Abstract

This thesis details a scheme, based on finite element methods, for modeling of the ballscrew drives of Cartesian-configured machine tools. Using this scheme, the structural dynamics of the ballscrew mechanism can be incorporated into the feed drive model, and thereby considered during high-bandwidth controller design, and interactive simulation of feed drive-controller performance in the virtual environment.

The finite element method used in this thesis for modeling is a hybrid kind, whereby the more rigid components of the feed drive are modeled as lumped-parameter rigid bodies, while the flexible members, like the ballscrew, are modeled using distributed-parameter structural members. As a result, a feed drive model is developed which both maintains a reasonably low level of complexity while adequately capturing the relevant dynamics needed for controller design and simulation.

This scheme also pays close attention to the modeling of the screw-nut interface, because it plays an important role in the functioning of ballscrew drives. Two methods are proposed for deriving the stiffness matrix of this interface – the Rigid Ballscrew Method and the Shape Function Method. The former method is shown to capture interesting dynamics of the interface, while the latter is derived in anticipation of situations where the former may not perform satisfactorily.

In order to show the benefits of this modeling scheme, three high-bandwidth controllers are designed. The first controller is designed based on the traditional technique which considers only the rigid-body dynamics of the drive. On the other hand, the second and third controllers are designed considering the rigid-body and structural dynamics information obtained from the proposed modeling scheme. Analyses performed on the three controllers reveal that the two controllers designed based on the proposed scheme outperform that which is designed following the traditional technique.

Finally, a simulation strategy is designed which allows the feed drive model, together with its non-linear dynamics to be combined with the controller dynamics and other dynamics of the feed drive system. In order to reduce simulation time, a novel method of performing model reduction based on a Component Mode Synthesis technique combined

with Modal Acceleration recovery is described. This method is used to achieve an efficient reduction without compromising relevant dynamic properties of the full model.

The potentials of the scheme presented in this thesis are demonstrated partly by experiments conducted on a test bed, and in other cases, by simulations performed on a model generated from the test bed.

Table of Contents

Abstract.....	ii
Table of Contents	iv
List of Tables	viii
List of Figures.....	ix
List of Nomenclature and Acronyms	xiii
Acknowledgement.....	xx
Chapter 1 Introduction.....	1
Chapter 2 Literature Review	5
2.1 Overview	5
2.2 Modeling of Feed Drives including their Flexibilities	5
2.3 Controller Design for Flexible Feed Drives	9
2.4 Integrated Simulation of Control Loop and Flexible Feed Drive Model	11
2.5 Summary	12
Chapter 3 Modeling of Ballscrew Drive Mechanism.....	13
3.1 Introduction and Overview.....	13
3.2 General Structure of a Typical Ballscrew Drive	14
3.3 Modeling of Drive Components.....	15
3.3.1 Ballscrew	16
3.3.2 Rotor, Nut and Table	18
3.3.3 Couplings, Bearings, Fasteners and Guideways.....	19
3.3.3.1 Couplings	20
3.3.3.2 Bearings	20
3.3.3.3 Fasteners	21
3.3.3.4 Guideways.....	21

3.3.4 Screw-Nut Interface.....	23
3.3.4.1 Modeling of Interface Stiffness	24
3.3.4.2 First Stage of Transformation: Local to Global Coordinates.....	25
3.3.4.3 Second Stage of Transformation: Lumping to Nodes.....	28
3.3.4.4 Derivation of Interface Stiffness Matrix	36
3.3.4.5 Determination of Ball Stiffness	39
3.4 Overall Structure of the Mathematical Model.....	40
3.5 Experimental Verification of Model	40
3.5.1 Description of the Experimental Test-Bed	40
3.5.2 Step-by-Step Verification of Model	44
3.5.2.1 Free-Free Ballscrew	44
3.5.2.2 Ballscrew and Nut.....	46
3.5.2.3 Full System without Table, Coupling and Rotor	51
3.5.2.4 Full System	54
3.6 Summary	56
Chapter 4 Model Analysis and Controller Design	58
4.1 Overview	58
4.2 Extraction of Open Loop Transfer Function of Feed Drive Model	58
4.2.1 Rigid-Body Dynamics	60
4.2.2 Inclusion of Structural Dynamics	60
4.3 High-Bandwidth Controller Design Based on Rigid-Body Dynamics	64
4.3.1 Design of the Analog PI-Controller.....	65
4.3.2 Design of the Digital P-Controller.....	68
4.4 Mitigation of Effects of Structural Dynamics on Controller Performance	70
4.4.1 Modification of the Mechanical Design	73
4.4.2 Application of Notch Filter.....	75
4.5 Mode-Compensating Pole-Placement Controller.....	80
4.6 Summary	89
Chapter 5 Interactive Simulation of Feed Drive-Controller Performance	90
5.1 Overview	90

5.2 Generation of Simulation Model of Feed Drive.....	90
5.2.1 State-Space Representation of the Linear Dynamics	90
5.2.2 Incorporation of the Non-Linear Dynamics	93
5.2.2.1 Coulomb and Static Friction	94
5.2.2.2 Backlash.....	96
5.2.2.3 Position-Dependent Structural Dynamics Variations	99
5.2.3 Model Reduction	100
5.2.3.1 Component Mode Synthesis	100
5.2.3.2 Reduction Using Constraint Modes	102
5.2.3.3 Response Recovery Using Modal Acceleration	103
5.3 Sample Implementation of Simulation Model	105
5.3.1 Interaction between Non-Linear and Higher Order Dynamics	105
5.3.2 The Impact of Model Reduction.....	109
5.3.3 Coupled Simulation of Controller, Process and Feed Drive Systems	112
5.4 Summary	119
Chapter 6 Conclusions.....	120
6.1 Conclusions	120
6.2 Future Research Directions	121
Bibliography	123
Appendix A Beam Element, Current-Frame Rotation and Modal Damping	
Formulations	127
A.1 Beam Element Formulations	127
A.2 Current-Frame Rotation Formulations	131
A.3 Modal Damping Formulations	132
Appendix B Determination of Parameters of Experimental Test-Bed.....	133
B.1 Ballscrew	133
B.2 Nut	134
B.3 Rotor and Table	134
B.4 Coupling	135

B.5 Bearings	136
B.6 Screw-Nut Interface.....	138
Appendix C Simulation Study on Cross-Coupling Terms of Screw-Nut Interface	
Stiffness Matrix	141
C.1 Purpose of Study.....	141
C.2 Description of Simulation Test Set-up	141
C.3 Effects of Cross-Coupling between the Bending Deformations	142
C.4 Effects of Cross-Coupling between the Axial/Torsion and Bending Deformations ..	143
C.5 Summary.....	146

List of Tables

Table 3.1: Parameters for Model of Experimental Test-Bed.....	42
Table 3.2: Position-Dependent Variation of First Axial Natural Frequency.....	51
Table 3.3: Position-Dependent Variation of First Torsional Natural Frequency.....	51
Table 4.1: Parameters for Mechanical Sub-System Transfer Functions.....	63
Table 4.2: Parameters for Mechanical Sub-System Transfer Functions (After Modification).....	75
Table 4.3: Coefficients of Notch Filter $G_M(z)$	77
Table 4.4: Coefficients of Polynomials A and B	84
Table 4.5: Coefficients of Desired Characteristic Equation, A_{cl}	86
Table 4.6: Coefficients of the R, S and T Polynomials.....	86
Table 5.1: Description of Sub-Models of Set-up.....	106
Table 5.2: Friction and Backlash Parameters for Set-up.....	106
Table 5.3: Comparison of Natural Frequencies of the Full and Reduced Sub-Models.....	110
Table 5.4: Parameters for Reference Trajectory Generation.....	113
Table 5.5: Parameters for Cutting Process Simulation.....	113
Table B.1: Dimensions of Ballscrew Sections.....	133
Table B.2: Parameters used in SpindlePro [®] Bearing Models.....	137
Table B.3: Parameters used to Obtain Interface Stiffness Matrix for Test-Bed.....	140
Table C.1: Inertia Properties of Table and Stiffness Properties of Guideway.....	142

List of Figures

Figure 1.1: Modeling of a Feed Drive based on Rigid-Body Assumptions.....	1
Figure 1.2: Modeling Scheme for Ballscrew Drives Presented in this Thesis.....	3
Figure 3.1: Sub-Systems of a Typical Feed Drive.....	13
Figure 3.2: Mechanical Components of a Ballscrew Feed Drive	15
Figure 3.3: Overview of Hybrid-Finite-Element Ballscrew Drive Model.....	16
Figure 3.4: Ballscrew Geometry	16
Figure 3.5: Timoshenko Beam Element	17
Figure 3.6: Rigid-body Transformations from the COM to any Point P.....	18
Figure 3.7: Model of a Typical Coupling	20
Figure 3.8: A Linear Guide Unit Consisting of a Slide and Rail.....	22
Figure 3.9: Model of Linear Guides using Vertical and Lateral Springs.....	22
Figure 3.10: Common Preload Mechanisms used in Machine Tool Feed Drives	23
Figure 3.11: Spring Model of Balls in the Screw-Nut Interface.....	24
Figure 3.12: Orientation of Contact Normal.....	25
Figure 3.13: Inclined Plane Representation of Ballscrew Thread	26
Figure 3.14: Relationship between Ball Coordinates and Screw Coordinates	27
Figure 3.15: Rigid-Ballscrew Method	29
Figure 3.16: Position Vectors for Ball Contact Points.....	30
Figure 3.17: Shape-Function Method	31
Figure 3.18: More Details of Shape-Function Method.....	32
Figure 3.19: Experimental Test-Bed.....	41
Figure 3.20: Axial FRF of Free-Free Ballscrew	45
Figure 3.21: Torsional FRF of Free-Free Ballscrew.....	45
Figure 3.22: Radial FRF of Free-Free Ballscrew.....	46
Figure 3.23: Axial FRF for Free-Free Ballscrew-Nut Assembly	47
Figure 3.24: Torsional FRF for Free-Free Ballscrew-Nut Assembly	47
Figure 3.25: Radial FRF for Free-Free Ballscrew-Nut Assembly	48
Figure 3.26: FRF Between Torque at Screw End and Axial Displacement at Nut	49
Figure 3.27: Position-Dependent Dynamics (Measured).....	50

Figure 3.28: Position-Dependent Dynamics (Simulated)	50
Figure 3.29: Axial FRF of Full System Except Table, Coupling and Rotor	52
Figure 3.30: Torsional FRF of Full System Except Table, Coupling and Rotor	53
Figure 3.31: Radial FRF of Full System Except Table, Coupling and Rotor	53
Figure 3.32: FRF from Excitation at Motor to Angular Acceleration at Ballscrew End.....	55
Figure 3.33: FRF from Excitation at Motor to Linear Acceleration at Table.....	55
Figure 4.1: Open-Loop Dynamics of Feed Drive Axis.....	59
Figure 4.2: Magnitudes of the FRFs between Feed Drive Inputs and Outputs.....	61
Figure 4.3: P-PI Control Scheme	64
Figure 4.4: Unit Step Response of Rigid-Body-Based PI-Controlled Velocity Loop.....	66
Figure 4.5: Response Functions for Rigid-Body-Based PI-Controlled Velocity Loop.....	67
Figure 4.6: Open-Loop Bode Diagram for Position Loop of Rigid-Body-Based P-PI Controller Combined with Rigid-Body-Based Feed Drive Model.....	69
Figure 4.7: Unit Step Response of Position Closed-Loop of Rigid-Body based P-PI Controller Combined with Rigid-Body-Based Feed Drive Model.....	69
Figure 4.8: Sensitivity and Complementary Sensitivity Functions of Position Loop for Rigid- Body based P-PI Controller Combined with Rigid-Body-Based Feed Drive Model.....	70
Figure 4.9: Open-Loop Bode Diagram for Position Loop of Rigid-Body-Based P-PI Controller Combined with Flexible Feed Drive Model	71
Figure 4.10: Unit Step Response for Position Loop of Rigid-Body based P-PI Controller Combined with Flexible Feed Drive Model.....	71
Figure 4.11: Sensitivity and Complementary Sensitivity Functions for Position Loop of Rigid-Body based P-PI Controller Combined with Flexible Feed Drive Model	72
Figure 4.12: Axial Mode Shape of Ballscrew for First Normal Mode (C-Position)	73
Figure 4.13: Torsional Mode Shape of Ballscrew for Second Normal Mode (C-Position) ...	74
Figure 4.14: Digital Notch Filter in Position Loop.....	76
Figure 4.15: Bode Diagram of Notch Filter.....	77
Figure 4.16: Open-Loop Bode of Position Loop for Re-designed P-PI Controller and Flexible Feed Drive with and without the Notch Filter.....	78

Figure 4.17: Unit Step Response of Position Loop for Re-designed P-PI Controller and Flexible Feed Drive with and without the Notch Filter.....	79
Figure 4.18: Sensitivity and Complementary Sensitivity Functions of Position Loop for Re-designed P-PI Controller and Flexible Feed Drive with and without the Notch Filter	80
Figure 4.19: Topology of Pole-Placement Controller.....	81
Figure 4.20: Pole-Placement Control Scheme	83
Figure 4.21: Pole-Zero Map of $B(z)/A(z)$	84
Figure 4.22: Open-Loop Bode of Position Loop Controlled with the PPC.....	87
Figure 4.23: Unit Step Response for Position Closed-Loop of PPC and Re-designed P-PI Controller with Notch Filter	87
Figure 4.24: Sensitivity and Complementary Sensitivity Functions for Position Loop of PPC and Re-designed P-PI Controller with Notch Filter	88
Figure 4.25: Unit Step Disturbance Response for Position Closed-Loop of PPC and Re-designed P-PI Controller with Notch Filter.....	89
Figure 5.1: Diagrammatic Representation of State-Space Model	92
Figure 5.2: Sample Implementation of Joint Stiffness and Damping Matrices.....	93
Figure 5.3: The Stribeck Friction Curve	94
Figure 5.4: Incorporation of Friction into Simulation Model	96
Figure 5.5: Classical Dead-Zone Backlash Model	97
Figure 5.6: Incorporation of Backlash into Simulation Model	98
Figure 5.7: Movement of Screw-Nut Interface Joint along Ballscrew	99
Figure 5.8: Incorporation of Position-Dependent Structural Dynamics Variations into Simulation Model	100
Figure 5.9: Implementation of CMS Reduction and MA Recovery Scheme	105
Figure 5.10: Excitation Signal Applied to Motor	106
Figure 5.11: Simulated Responses of the Table with and without Non-linearities	107
Figure 5.12: Simulated Responses of the Table Measured at the C and R-Positions.....	108
Figure 5.13: Comparison of the Rigid-Body and FE Models with Experiments.....	109
Figure 5.14: Comparison of the Simulated Responses from the Full and Reduced Models	111

Figure 5.15: Zoomed View of the Simulated Responses from the Full and Reduced Models	112
Figure 5.16: Slotting Operation	112
Figure 5.17: Reference Trajectories for Slotting Operation	114
Figure 5.18: Feed Cutting Forces over One Spindle Revolution.....	114
Figure 5.19: Simulated Responses of Feed Drive Controlled with Rigid-Body Based P-PI Controller.....	115
Figure 5.20: Simulated Responses of Feed Drive Controlled with P-PI+Notch Filter.....	115
Figure 5.21: Simulated Responses of Feed Drive Controlled with PPC	116
Figure 5.22: Comparison of Simulated Acceleration Responses of Feed Drive controlled by Various Controllers under Effects Cutting Force Disturbances	118
Figure A.1: Timoshenko Beam Element	127
Figure B.1: Pictorial Representation of FE Model of Ballscrew	133
Figure B.2: Nut and Hollow-Cylinder Approximation for Calculating Its Inertias.....	134
Figure B.3: Test-Bed's Table.....	135
Figure B.4: Jaw-Type Coupling Between Motor Shaft and Ballscrew	135
Figure B.5: Torsional FRF between a Point on J_1 to a Point on J_2	136
Figure B.6: Model of Angular-Contact Bearing generated using SpindlePro®	137
Figure C.1: Simplified Rigid-Body Model of Table and Nut.....	141
Figure C.2: 9 th Mode Shape of Set-up for Case A at 659 [Hz].....	142
Figure C.3: 9 th Mode Shape of Set-up for Case B at 659 [Hz]	143
Figure C.4: Variation of Cross-Coupling Terms with Ballscrew's Pitch	144
Figure C.5: 19 th Mode Shape of Set-up for Case A at 1470 [Hz]; pitch = 10 [mm].....	144
Figure C.6: 19 th Mode Shape of Set-up for Case B at 1470 [Hz]; pitch = 10 [mm].....	145
Figure C.7: 19 th Mode Shape of Set-up for Case A at 1385 [Hz]; pitch = 45 [mm].....	145
Figure C.8: 19 th Mode Shape of Set-up for Case B at 1382 [Hz]; pitch = 45 [mm].....	146

List of Nomenclature and Acronyms

Nomenclature

A	system matrix in state-space representation
a (superscript)	indicates a parameter pertaining to an attachment point
$A(z), B(z)$	denominator and numerator polynomials for plant transfer function
$A^-(z), B^-(z)$	factors of A and B that cannot be cancelled
$A^+(z), B^+(z)$	factors of A and B that can be cancelled
$A_c(z), A_o(z)$	controller and observer polynomials
$A_{cl}(z)$	desired closed-loop characteristic polynomial
A_x (subscript)	indicates a parameter pertaining to the axial direction
B	input matrix in state-space representation
B	viscous damping constant of rigid-body mode
$Ball$ (subscript)	indicates a parameter pertaining to the balls
BS (subscript)	indicates a parameter pertaining to the ballscrew
BS_i (subscript)	indicates a parameter pertaining to the i^{th} node of the ballscrew
$BS\xi$ (subscript)	indicates a parameter pertaining to a location at a distance ξ within an element of the ballscrew
c	y-intercept for a linear function; viscous damping constant of a mechanical element
C	elastic coefficient from Hertzian contact formula
C	viscous damping matrix; output matrix in state-space representation
CS	coordinate system
d	diameter

d	generalized vector of displacements
D	matrix between inputs and outputs in state-space representation
d_1, d_2	coefficients for denominator of notch filter
d_{in}, d_{out}	displacements of input and output elements in backlash model
E	Young's modulus
E, I	exterior and interior DOF
e, i (subscript)	indicate parameters pertaining to exterior and interior DOF, respectively
Elm (subscript)	indicates a parameter pertaining to an element of the ballscrew
$Elmi$ (subscript)	indicates a parameter pertaining to the i^{th} element of the ballscrew
End (subscript)	indicates an ending position
F	force in a specified direction
F	vector of forces at a specified point; generalized vector of forces
F_{coul}^+, F_{coul}^-	positive and negative coulomb friction forces
F_{stat}^+, F_{stat}^-	positive and negative static friction forces
F_f	friction force
f_n, ω_n	natural frequency
G	shear modulus of elasticity
g, G	acceleration due to gravity
$G(s), G(z)$	transfer function
$G_d(s)$	transfer function between the table disturbance force and table position
$G_e(s)$	transfer function pertaining to the feed drive's electrical subsystem
$G_m(s)$	transfer function between the motor torque and table position
$G_N(z)$	transfer function of digital notch filter
$G_v(s)$	transfer function of velocity closed-loop dynamics

$G_x(s)$	transfer function between the motor's angular velocity and table position
$G_\omega(s)$	transfer function between the motor torque and motor's angular velocity
H	height
H_g	tachometer constant
I	moment of inertia or second moment of area
i, j, k (subscript)	index counters
J	moment inertia about an axis of rotation
<i>joint</i> (subscript)	indicates a parameter pertaining to a joint
k	stiffness of a mechanical component
\mathbf{K}	stiffness matrix
K_i, K_v, K_p	integral and proportional gains of PI controller, and proportional gain of P controller, respectively
K_N	adjustment factor for notch filter
L	length
L (subscript)	indicates the L contact configuration
L_{lead}, L_{lag}	instantaneous lead and lag distances of output element in backlash model
m	Mass; slope for a linear function
M	moment about a specified axis
\mathbf{M}	mass matrix
<i>model</i> (subscript)	indicates a parameter pertaining to the full feed drive model
N	number, in terms of counts, of a parameter
$n(z)$	measurement noise
N, nut (subscript)	indicates a parameter pertaining to the nut
n_1, n_2	coefficients for numerator of notch filter

N_L, N_R	nodes to the left and right of nut attachment point on ballscrew
$Node$ (subscript)	indicates a parameter pertaining to the ballscrew nodes
$Node_i$ (subscript)	indicates a parameter pertaining to i^{th} node of the ballscrew
p	pitch of ballscrew
P	mode shape matrix
P	number of modes retained in a modal truncation; point on a body
p (subscript)	indicates the number of modes retained in a modal truncation
prd (subscript)	indicates a parameter pertaining to an applied preload
q	vector of modal displacements
q (subscript)	indicates a modal parameter
r	position vector from the origin of a coordinate system to a specified location
r	scalar position from the origin of a coordinate system to a specified location
R	pitch radius of ballscrew; residue of a transfer function
r (subscript)	indicates a parameter pertaining to the root of the ballscrew's threads; indicates a reference parameter
r (superscript)	indicates a transfer function based on only rigid-body dynamics
$R(z), S(z), T(z)$	transfer functions for pole-placement controller
$R^*(z), S^*(z)$	remainders of the R and S polynomials after being divided by their respective desired factors
Rad (subscript)	indicates a parameter pertaining to the radial direction
$R_d(z), S_d(z)$	desired factors for the R and S polynomials, respectively
red (superscript)	indicates a reduced parameter
r_g	ballscrew's gear reduction ratio

r^G	radius of gyration
Rot	rotation operator
s	Laplace operator
$S(\cdot)$	operator which expresses the vector enclosed in the parenthesis in its tensorial form
$S(s), S(z)$	sensitivity function
sm (subscript)	indicates a parameter pertaining to a sub-model
SN (subscript)	indicates a parameter pertaining to the screw-nut interface
St (subscript)	indicates a starting position
T	transformation matrix
$T(s), T(z)$	complementary sensitivity function
thr (subscript)	indicates a parameter pertaining to the ballscrew threads
To (subscript)	indicates a parameter pertaining to the torsional direction
T_s	servo sampling time
$T_{spindle}$	spindle's period of rotation
u	vector of translational displacements; inputs vector in state-space representation
U (subscript)	indicates the U contact configuration
$u(s), u(z)$	control signal
u, v, w	translational displacements in the x, y and z directions, respectively
V	volume
v	sliding velocity
$V^{+/-}_1, V^{+/-}_2$	positive and negative velocity thresholds for Stribeck friction curve
x	state vector in state-space representation

$x(s), x(z)$	table's actual position
x, y, z (subscript)	indicate parameters pertaining to the x, y and z directions
y	output vector in state-space representation
Z	z-transform operator
z	z operator for sampled-data systems
α, β	pitch and thread angles of ballscrew, respectively
δ	incremental offset used to apply preload in the offset preload mechanism
ζ	damping ratio
ζ_N, ζ_D	damping ratios for numerator and denominator of notch filter transfer function, respectively
θ	vector of rotational displacements
$\theta_x, \theta_y, \theta_z$	rotational displacements about the x, y, and z axes, respectively
ξ	non-dimensional distance from one end of an element to a specified point within the element
ρ	density
$\pi(s), \pi(z)$	motor torque
ϕ	azimuth angle about ballscrew's axis
Φ	constant in Timoshenko beam formulations
ϕ	matrix of constraint modes
χ	mass-normalized mode shape matrix
ψ	recovery matrix for MD method
$\omega(s), \omega(z)$	motor's angular velocity
ω_N, ω_D	natural frequencies for numerator and denominator of notch filter transfer function, respectively

Acronyms

CAD	Computer-Aided Design
CL	Closed-Loop
COM	Center of Mass
CMS	Component Mode Synthesis
DOF	Degree of Freedom
FE	Finite Element
FEM	Finite Element Method
FRF	Frequency Response Function
GM	Gain Margin
I.D	Inner Diameter
LTI	Linear Time-Invariant
MA	Modal Acceleration
MD	Modal Displacement
NF	Notch Filter
O.D	Outer Diameter
OL	Open-Loop
PID	Proportional, Integral and Derivative
PM	Phase Margin
PPC	Pole-Placement Controller
P-PI	Proportional-Proportional Integral
SMC	Sliding Mode Controller
SS	State-Space
TF	Transfer Function

Acknowledgement

I would like to express my sincere gratitude and appreciation to my supervisor, Dr. Yusuf Altintas who to me is an epitome of a knowledgeable, considerate and caring professor. His support, guidance and, most of all his, personality have provided a source of inspiration throughout my masters program here at UBC.

In the same vein, I also want to thank my colleagues at the Manufacturing Automation Laboratory (MAL) for their warmth and friendliness. They have created a wonderful atmosphere of openness and cooperative assistance in the lab that has left a lasting impression on my heart. MAL is a great place to be.

I would like to cease this opportunity to express my sincere appreciation to my beloved family for being a great source of encouragement to me. I am proud to have such a loving and caring family. My heartfelt gratitude also goes to my lovely girlfriend and her family whose care and companionship have helped to provide the inner strength I needed to carry on.

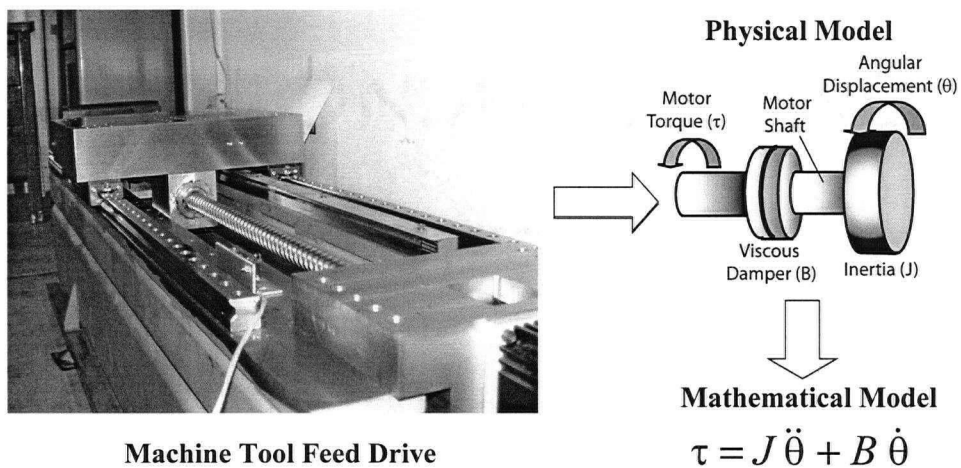
I also want to say a big thank you to my friends who in various ways have supported me and brought joy to my heart, directly or indirectly.

Finally, I want to express my deepest thankfulness to my Father in Heaven who has given me life and every thing I need to enjoy it.

Chapter 1

Introduction

For many years, control engineers in the machine tool sector have assumed that the coupling between feed drive structural dynamics and controls is negligible, permitting them to model the dynamics of feed drives based on rigid-body assumptions. A very common example of such rigid-body models is shown in Figure 1.1, where a ballscrew feed drive mechanism is modeled as a lumped inertia, J and equivalent viscous damping, B , both reflected at the motor shaft. As a result, the dynamics of the mechanism can be mathematically expressed as an uncomplicated linear differential equation (Figure 1.1). Such models, even though simple, have been successfully used for controller design, analysis and simulation, and have yielded excellent results because of the validity of the rigid-body assumptions under which they were derived.



Machine Tool Feed Drive

Figure 1.1: Modeling of a Feed Drive based on Rigid-Body Assumptions

However, the growing pressure in recent years towards increased productivity and reduced time-to-market has created enormous demands on the manufacturing industry for faster machine tools which can increase the metal removal rates in machining operations. On the other hand, demands for higher part tolerances and better surface quality of machined products have provoked a conflicting requirement for the highest tool positioning accuracy in such operations. In response to these demands, machine tool producers have pushed the frontiers of High Speed Machining (HSM) to a point beyond which these desirable but

otherwise unattainable results can be reached. This has come as a result of advances in various areas of machine tool engineering. For instance, the advent of tooling materials such as carbide, ceramic, polycrystalline diamond, and cubic boron nitride, has significantly increased metal removal rate potential. In a similar vein, the use of ceramic balls in spindle bearing systems have increased the achievable speeds of machine tool spindles to values exceeding 20,000 [rpm].

In order to compliment the advances in these other areas, machine tool feed drives have also been improved such that they are able to achieve high feedrates (typically greater than 50 [m/min]) and accelerations that exceed 1 [G] while aiming to attain sub-micron positioning accuracy. These improvements are realized by designing rigid but light mechanical structures actuated by high-bandwidth drives and equipped with low-friction roller or hydrostatic guideways. Furthermore, these feed drives are furnished with high-resolution feedback devices and controlled with sophisticated hardware and software.

However, higher feedrates and, in particular, higher accelerations lead to a proportional increase in the amount of inertial reactions borne by the drives. On the other hand, reduction in material usage may lead to loss of stiffness in some parts of the mechanical structure, while low friction in the guideways reduces the amount of damping in the system. All these factors put together result in increase in the oscillatory excitations of the drives and structural components which are easily picked up by the feedback devices and fed into the controllers. The result of this is that structural vibrations and controls become closely coupled and rigid-body models become unable to provide an accurate model of feed drive dynamics for control purposes.

Consequently, in order to exploit the full potential of such machines, the structural dynamics of the feed drives have to be identified and modeled in such a way that this dynamic interaction between structural vibrations and controls to be analyzed and incorporated into controller design and performance simulation.

Moreover, because of the increasing power of computer tools, the growing trend these days in machine tool engineering is to shift the validation of machine design and process optimization to so called virtual prototypes through numerical simulation. In this way, costly and time-consuming experimental validation on actual prototypes can be reduced. Therefore,

in order for feed drive dynamics and numeric control to be incorporated in such a virtual prototype, the feed drive modeling has to be performed using Computer-Aided Engineering (CAE) tools as opposed to experiments. Furthermore, the modeling has to be carried out in such a way that the feed drive model, together with the controls for each axis can be integrated into the virtual prototype to interact with its other subsystems, for instance the process dynamics.

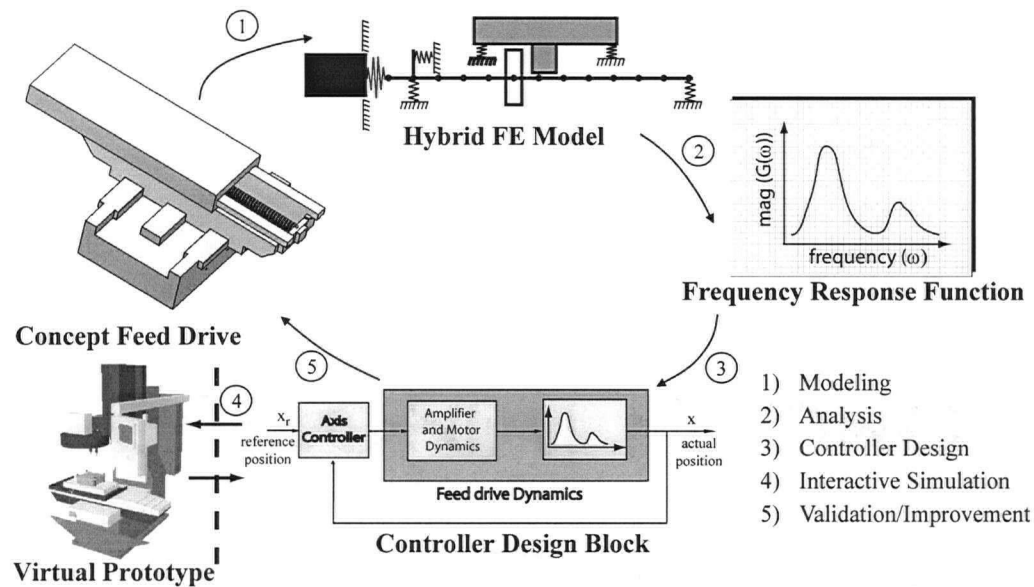


Figure 1.2: Modeling Scheme for Ballscrew Drives Presented in this Thesis

In response to the aforementioned challenges, this thesis proposes a modeling scheme (shown in Figure 1.2) for Cartesian-configured ballscrew feed drives, whereby the dynamics of the concept feed drive for a high-speed machine tool can be modeled using a hybrid finite element technique, resulting in both lumped rigid-body components and distributed-parameter components. In this way, the structural dynamics of the feed drive can be captured in the model, while endeavouring to keep the model complexity minimal. Such a model can then be analyzed in order to extract the relevant dynamic information (for instance, in the form of frequency response functions) needed for controller design. By introducing this information into a controller design block, a suitable controller can be designed that will achieve the desired performance specifications of the drive. In addition, the model can be reconfigured in such a way that it is able to interact with a virtual prototype of the machine

tool, along with the controller dynamics, in order to perform time-domain performance simulations. The results of such simulations can then be used to validate or improve the feed drive design by iterating through the entire process until optimum performance characteristics are obtained.

Henceforth, the thesis is organized as follows: Firstly, a review of related literature is presented in Chapter Two, then a full description of the hybrid finite element modeling scheme for ballscrew drives is given in Chapter Three. Chapter Four then shows how the model resulting from Chapter Three can be analyzed and used to design high-performance controllers. Following this, Chapter Five gives a detailed methodology for generating a comprehensive simulation model based on the hybrid finite element model of Chapter Three, and using it for time-domain simulations of feed drive-controller performance. Finally, the conclusions and possible research directions are discussed in Chapter Six, while additional pieces of information needed to understand the content of the thesis are detailed in the ensuing bibliography and appendices.

Chapter 2

Literature Review

2.1 Overview

In the previous chapter, the challenge faced by machine tool designers and control engineers, due to the enormous demands from high-speed machine tools, was explained in detail. Machine tool designers were seen to be striving to reach a compromise between increasing the metal removal rates and satisfying the high-precision requirements for their machine tools. On the other hand, machine tool control engineers were coming to a realization that the ambitions of their colleagues in the design team render their simplified models for controller design and simulation invalid.

As is always the case, these needs in the industry have aroused the interest of researchers in the concerned fields of study in a bid to find solutions to the problems arising from them. This chapter is therefore aimed at reviewing the work done by other researchers, which bear relevance to the topics and contributions of this thesis. Section 2.2 takes a look at research in the area of modeling of feed drives, including their flexibilities, while Section 2.3 covers research related to controller design based on these improved models. Work done on the integrated simulation of feed drive and controller performance is reviewed in Section 2.4, and then a summary of the contents of this chapter is presented in the last section.

2.2 Modeling of Feed Drives including their Flexibilities

As the speed and precision requirements from machine tools increase, the effects of the structural flexibility of the drives on controller performance are becoming increasingly significant. This trend has prompted researchers to look into ways of identifying and incorporating drive flexibility into feed drive model for controls.

Allotta et al [1] used modal identification and updating techniques to identify the position dependent boundary conditions of a ballscrew system. This they achieved by first creating a free-free finite element (FE) model (without physical constraints) of the screw. Then, using scalar springs with unknown stiffness in different directions, they applied

boundary conditions corresponding to the bearings and nut supports. By matching the resonance and anti-resonance frequencies of the model and experimental measurements, using an iterative technique, the unknown stiffness coefficients of the constraints were identified. This model was then used to demonstrate, by simulation, a possible vibration suppression technique using derivative control, with piezo-actuators placed at the bearing locations. Also using experimental techniques, Erkormaz [13] identified the inertia, damping parameters, guideway friction and the structural dynamics of a ballscrew feed drive. Based on this information, he derived a comprehensive model, suitable for controller design and simulation, which includes all these effects. Lee et al [28] proposed an experimental technique for identifying the parameters of a feed drive model including some structural dynamics based on contour error measurements using a cross grid encoder. Using this model, and the same contour error measurements, they outlined a procedure for tuning the controller parameters in order to reduce the structural vibrations of the machine tool in order to improve its overall contouring accuracy.

Reinhart and Weissenberger [38] explain that the interaction between controls and mechanical structure in present-day machine tools makes them characteristic examples of complex mechatronic systems and so they have to be designed as such. They suggest a two-stage process in the early phases of design where firstly, various functional subsystems are designed separately, and then, these separate subsystems are combined and optimized integrally as a complete mechatronic system using a Multi-Body System (MBS) modeling and simulation approach.

Varanasi [47] has derived a feed drive model, which considers the distributed inertia and compliance of the ballscrew together with the compliance and damping of all of the major elements of the feed drive. This distributed-parameter beam model of the ball screw drive system is reduced to a low-order model using a Galerkin's procedure based on shape functions derived from the quasi-static deformation of the system, and is shown to give good prediction of the open-loop transfer function of the drive when compared to experimental results. Following simplifying assumptions made on the design, he applies a perturbation expansion to obtain approximate expressions relating the open-loop poles to the design parameters, thereby forming a link between the mechanical and controller design. This then

enables him to derive relationships which enable optimal drive structural design parameters to be selected based on the desired closed-loop performance characteristics.

Pislaru et al [35] suggest a hybrid methodology for modeling machine tool feed drives whereby the ballscrew is modeled using distributed parameters while the other components are modeled using lumped parameters. The distributed-parameter model of the ballscrew consists of a bunch of masses/inertias and springs which represent various sections of the ballscrew. One problem with this method however is that it cannot capture the changing dynamics of the feed drive system as the nut moves along the ballscrew due to the fact that the value of the ballscrew's parameters are apparently obtained for only one position of the nut.

As an alternative or complement to the methods for modeling machine tools proposed by the researchers mentioned above, finite element methods (FEM) have attracted the attention of many researchers. Van Brussel et al [46] employed FEM to model a three-axis milling machine including the feed drive. Using component mode reduction procedures in two steps, the original FE model was reduced to a state-space model suitable for control design and simulation. Their model was able to capture the position-dependent dynamics of the drives. Zaeh, Oertli and Milberg [51] picked up the challenge of creating a more realistic FE model of ballscrews using universal FEM codes. They aimed at adequately capturing the force/torque straining during transmission, and also incorporating the total stiffness of the rolling balls between the ballscrew and the nut. Based on a reduced state-space model derived from their FE model, they also simulated the behavior of the control loop.

As a step towards predicting the thermal behavior of ballscrews, Holroyd et al [18] also used FEM to model and simulate the dynamics of a ballscrew, taking into account the time-changing boundary conditions. By assuming that the displacement response at each time step can be approximated by a power series, the coefficients of the series were determined based on mass, damping and stiffness matrices, which were assumed to remain constant during each time step but were updated after the step. The analysis accuracy, which was improved by integrating data acquired from experimental modal analysis, gave results that show a close match to experimental measurements. Smith [42], Berkemer [4] and Schafers et al [40], have also used FEM in modeling machine tool feed drives for control purposes.

One aspect of ballscrew drives that requires a great deal of attention when modeling is the interface between the ballscrew and nut. This is because it plays an important role in the transmission of motion, vibrations and forces from the ballscrew to the table. Lin et al [31], by studying the kinematics of the balls as they travel within the raceways of a ballscrew mechanism have established that the balls always undergo micro-scale slip along constant sliding lines during motion transmission. Wei and Lin [48] have furthered this study by modifying the assumptions made with regard to the friction coefficients, normal forces and contact angles created at the ball/screw and ball/nut contact interfaces. Furthermore, they have included the effects of the drag force generated as the ball moves in an oil lubricant in their model. Based on these modifications, they have noted significant differences between the modified model and the previous model by Lin et al [31], particularly at high rotational speeds. In the same vein, Cuttino et al [9,10] have used FEM to derive a relationship between the torque generated as the ball rotates in the raceway and the angle of rotation. Relying on this relationship, they have successfully predicted the micro-scale hysteretic behavior observed in the torque and displacement transmission characteristics of the preloaded nut interface.

In deriving a stiffness for the screw-nut interface, many of the researchers mentioned above [1,4,18,35,42,47] have considered only the axial and/or torsional deflections of the ballscrew. Zaeh et al [51] go a step further to include the effects of the ballscrew's bending deformations through 3-D transformations of the stiffness of each individual ball. However, their method falls short of determining some cross coupling terms between deformations in the bending, axial and torsional directions of the ballscrew and nut which may be significant to the dynamics of ballscrew drives.

In modeling ballscrew drives, this thesis employs a hybrid FE methodology whereby the ballscrew is modeled as a Timoshenko beam, while the other more rigid components are modeled as lumped masses/inertias connected by springs. Furthermore, the screw-nut interface formulations are derived in such a way that they include the bending deformations of the ballscrew, and also capture the additional cross coupling terms between the deformations in the bending, axial and torsional directions of the ballscrew and nut.

2.3 Controller Design for Flexible Feed Drives

Controller designs considering the mechanical resonances of the controlled system have been widely performed on robot manipulators with flexible joint and/or links [5,11,20,26,27]; however, their application to machine tool feed drives is a more recent development. Lim et al [29] have reported that a torsional displacement feedback control scheme similar to the joint torque feedback method in robot systems, which is based on an estimation of torsional displacement of flexible ballscrews with known stiffness properties, leads to a significant reduction in the error of the table position. Chen and Tlustý [7] showed by simulation that applying accelerometric feedback combined with a feed-forward compensator on a flexible feed drive improved the transient response at the machine tool table and chatter vibration characteristics between the cutting force and machined part.

Erkorkmaz [13] designed two controllers based on his feed drive model described in the previous section. The first was an elaborate Sliding Mode Controller (SMC) designed to actively compensate the effect of the first torsional mode of the ball screw. The second was much simpler than yet as effective as the first. It was performed by filtering out the first torsional mode using a notch filter and then designing a SMC based on rigid body dynamics alone. Both controllers were shown to improve the high speed tracking and contouring performance of the drives significantly when compared to similar designs which did not consider the flexibility of the drives. Smith [42] has also implemented notch filtering of the problematic modes arising from the ballscrew, making it possible to increase the bandwidth of the feed drive, hence improve its performance. Another method of reducing the vibrations of the drive, utilized by researchers, is the shaping of input commands in order to remove the frequency contents in the axis commands that may excite the structural resonances of the feed drive system [22].

Due to the changing support conditions as the table moves within the workspace, the structural dynamics of flexible feed drives change depending on the position of the table. This poses a great challenge from the controller design stand point, as the plant can no longer be characterized as a Linear Time-Invariant (LTI) system. In order to achieve robust stability and high-performance control for a direct driven machine tool, Symens et al [45] have applied gain-scheduling as an alternative to classical fixed-parameter controllers which do

not perform well for such machine tools with varying structural flexibility. They employed two different scheduling schemes – one ad-hoc and the other analytically derived – on H_∞ controllers designed for various positions of a machine tool with position-dependent structural dynamics. Their experiments yield good results from the ad-hoc scheme but the analytically derived Linear Parameter Varying (LPV) scheduling scheme requires some improvements.

Instead of scheduling the controller parameters, Van Brussel et al [46] capitalize on the robustness of the H_∞ controller, by performing a design based on the nominal position of the machine tool, while factoring in the information regarding the position-dependent variation of dynamics into the uncertainty model of the controller. This controller, which considers the flexibilities of the machine, is shown to outperform a reference PID controller which is designed based on only rigid-body dynamics, in tracking performance. However, when it comes to disturbance rejection, the H_∞ controller is seen to perform poorly. Its disturbance rejection performance is improved by building it around a velocity loop closed with a PI-Controller which adds more damping to the system.

Smith et al [43], also on the control of machine tools with changing or unknown parameters, designed three adaptive controllers – an adaptive PID, an adaptive phase compensator and an adaptive phase compensator that explicitly consider input constraints (saturation) – which they implemented on a prototype machine tool axis. The results show that the adaptive control schemes offer greater robustness to parameter variation and better overall performance than an ordinary PID controller. Furthermore, implementing them does not involve much more than a PID controller. However, their controllers did not include the structural dynamics of the feed drive.

Schafers et al [40] explain that while tackling the problems caused by structural dynamics interacting with controls, control related measures are not enough. They suggest making improvements on the mechanical design of the machine tool as an alternative means of dealing with these problems.

This thesis shows that considering the flexibility of drives in controller design through either mode compensation or notch filtering, together with modifying the mechanical design,

go a long way to improve the performance of the feed drive, when compared to a design based on rigid-body dynamics.

2.4 Integrated Simulation of Control Loop and Flexible Feed Drive Model

In order to better analyze the interaction between the control and structural dynamics of a flexible feed drive, it is desirable to incorporate the flexible feed drive model into the control loop in a way that both the mechanical design and control design can be optimized as a whole. Yeung [49] has developed a comprehensive design and simulation environment for CNC machine tools with Cartesian drive configurations, which includes trajectory generations modules, feed drive rigid-body dynamic properties, system nonlinearities (such as Coulomb friction, actuator saturation and backlash), and various axis control laws. Using this simulation scheme, various feed drive performance criteria can be investigated in the virtual environment.

A similar venture was undertaken by Pislaru et al [35], using the hybrid model they developed for feed drive systems. They also accounted for the distributed loads, explicit damping factors and measured non-linear effects like friction and backlash of the various components of the drive system. In addition to obtaining simulation results which compared favorably with experimental results, their model was able to produce data useful for the prediction of interactions between components, which is needful for the mechanical design. In describing the MBS simulation approach, Reinhart and Weissenberger [38] suggest that the control loop could be reconfigured such that it acts as an external force element with in-built dynamics that can interact with the MBS. In this way, the actuation force is made to act on the MBS and, in return, state variables like position, velocity and acceleration are returned to the control loop as feedback. Thereby, an interactive simulation scheme between the control loop and mechanical structure can be achieved.

In order to successfully incorporate a prototype of a real-time virtual machine tool, which is capable of simulating the drive dynamics and mechanical components, into the control loop, Pritschow and Rock [36] have pinpointed that the simulation step must be kept constant. However, this gives rise to certain hardware and algorithmic challenges. They tackled the hardware problems by inserting a second real-time extension kernel between the hardware and kernel of standard operating systems. On the other hand, the algorithmic

difficulties were solved by predetermining a step-size and algorithm order that will ensure absolute numerical stability in the chosen algorithm, while keeping the step-size and number of operations within the simulation step constant. With these problems overcome, they were able to perform real-time simulations using a virtual prototype planted within the control loop of an actual CNC machine and obtain results comparable with those from the real machine.

The issue of lessening of simulation time through model reduction is also an important issue in performance simulation of feed drives, this is particularly so for FE models which are usually large and complex with a lot of redundant information. Van Brussel et al [46] have used Component Mode Synthesis (CMS) methods with Modal Displacement (MD) recovery to achieve a reduction of their FE model of a machine tool. However, they encounter a problem because the MD recovery method does not allow for a full reduction of the model due to the need to capture the changing dynamics of the machine tool, as the position of the table varies.

In this thesis, a simulation strategy which allows the incorporation of the drive's non-linear effects, including the position-dependent variations in structural dynamics, and at the same time permits a full reduction of the FE model is presented. This is achieved by using a CMS method together with Modal Acceleration (MA) recovery.

2.5 Summary

In this chapter, literature related to modeling, control and simulation of flexible feed drives has been highlighted. The motivation for research into this area has been explained and various alternatives put forward by other researchers have been mentioned in order to place the work that follows in perspective, and provide a background for further research into this area.

Chapter 3

Modeling of Ballscrew Drive Mechanism

3.1 Introduction and Overview

Feed drives constitute one of the core systems in machine tools because they are responsible for the rapid and accurate realization of the complex motion commands required in High Speed Machining (HSM). At the same time, they also have to withstand the high forces resulting from this motion, and from the machining process being carried out.

A typical feed drive can be divided into two main sub-systems which perform complimentary functions – the electrical and mechanical sub-systems. As shown in Figure 3.1, the electrical sub-system is responsible for converting control signals coming from the CNC (Computer Numerically Controlled) unit into some kind of actuation force. It usually consists of components such as Digital-to-Analog (D/A) conversion circuitry, servo-amplifiers, and an actuator which could be a linear or rotary motor.

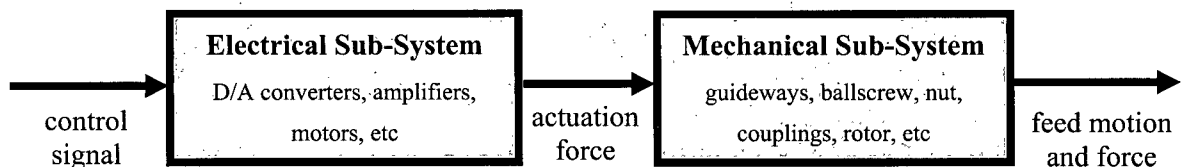


Figure 3.1: Sub-Systems of a Typical Feed Drive

The mechanical sub-system, on the other hand, serves the purpose of transforming the actuation force into useful motion and force at the machine tool table where it is needed. Its configuration and constituent components highly depend on what kind of drive technique is employed in the feed drive. The two most commonly used techniques are the direct drives, based on linear motor technology, and the indirect or ballscrew drives.

Direct drives, as the name suggests, directly supply linear motion and force at the machine tool table without any need of an intermediary conversion. Therefore they have an advantage over the ballscrew drives because they involve fewer components and so are simpler to design and assemble. In addition, they can achieve higher speeds and accelerations

with minimal backlash and friction, and they have an unlimited travel range. However, they have some significant drawbacks. The absence of a gear reduction between the linear motor and table, in direct drives, makes them sensitive to changes in workpiece inertia and disturbance forces. Furthermore, their stiffness depends mainly on the controller settings, and has little re-enforcement from the mechanical structure. The deceleration of the drive in a case of power outage is also a challenge when using linear drives, since they do not generate any back thrust and only depend on guideway friction for deceleration forces. This can result in destructive collisions with the spindle, workpiece and tooling.

The ballscrew drive overcomes most of the shortcomings of the direct drive because it provides thrust and linear motion at the table by converting power from a rotary motor through a ballscrew mechanism. This gives it the ability to be relatively insensitive to changes in workpiece inertia and disturbance forces, while deriving some stiffness from the mechanism. In addition, in the case of a power outage, the mechanical system back-drives the ballscrew and motor causing the drive to decelerate rapidly.

The characteristics mentioned above, coupled with improvements in indirect drive technology which have resulted in ballscrew drives that can attain up to 60 [m/min] rapid traverse speeds and accelerations that exceed 1 [G], have made ballscrew feed drives to remain a favourable choice for many machine tool designers. However, these improvements have also necessitated a modeling scheme which addresses the dynamic interactions, discussed in Chapter One, between their mechanical structure and controllers.

Consequently, this chapter describes the components of a typical ballscrew drive in Section 3.2, followed by a hybrid finite element methodology for modeling these components using a combination of structural members and rigid bodies, in Sections 3.3 to 3.4. This is followed by a step-by-step experimental validation of the model in Section 3.5, and then some concluding remarks in Section 3.6.

3.2 General Structure of a Typical Ballscrew Drive

A diagram of one axis of a ball screw drive is shown in Figure 3.2. Its main component is the ballscrew which is attached to the rotor through a coupling. The screw is usually supported at both ends. At the end proximal to the motor, it is supported by thrust bearings

which constrain it axially and radially. On the other side distal to the motor, it is either unsupported or is supported by a radial bearing which is axially unconstrained in order to permit the thermal expansion of the screw. Pre-tensioned ballscrews also exist for which the distal end of the screw is also supported axially in order to keep it in tension. This way, stresses resulting from thermal growth are reduced.

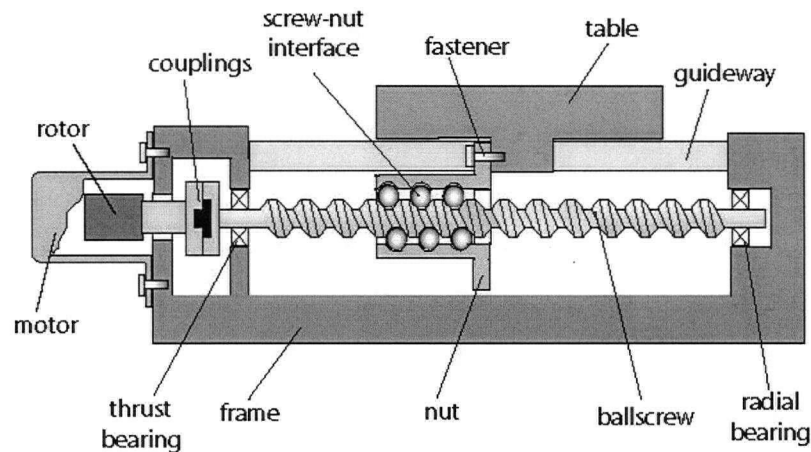


Figure 3.2: Mechanical Components of a Ballscrew Feed Drive

As depicted in the figure, the rotary motion from the screw is converted to a translation at the nut through the constrained relative motion of the screw-nut interface. Fasteners are used to connect the nut to the table, while the guideways direct and support the table. The machine tool frame provides the supporting structure for all the components in the assembly. The components are either rigidly connected to the frame, or they are connected to it using fasteners.

3.3 Modeling of Drive Components

In modeling the drive components described above, a hybrid finite element method consisting of structural members for flexible components and lumped-parameter models for relatively more rigid parts has been employed. Figure 3.3 gives a schematic overview of the method, for a single-axis ballscrew drive.

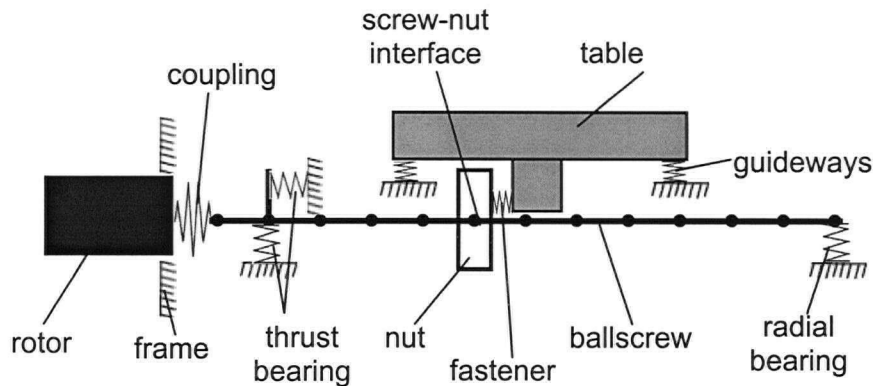


Figure 3.3: Overview of Hybrid-Finite-Element Ballscrew Drive Model

As shown in the figure, the ballscrew is modeled using Timoshenko beam finite elements, while the rotor, table and nut are modeled as lumped masses and inertias. The couplings, bearings, fasteners and guideways are modeled using linear and rotary spring elements. As for the frame, it is assumed to be rigid and fixed to the ground since all measurements are taken relative to it. The interface between screw and nut is modeled using a special spring element having 6 degrees-of-freedom (DOF).

A detailed breakdown of this methodology is presented in the following sections.

3.3.1 Ballscrew

The ballscrew has a simple geometry for most of its cross-sections; therefore, it can be readily modeled using beam finite elements. However, the threaded section, as shown in Figure 3.4 poses a significant challenge because the threads create a varying and complicated cross-section which can only be captured using 3-D finite elements.

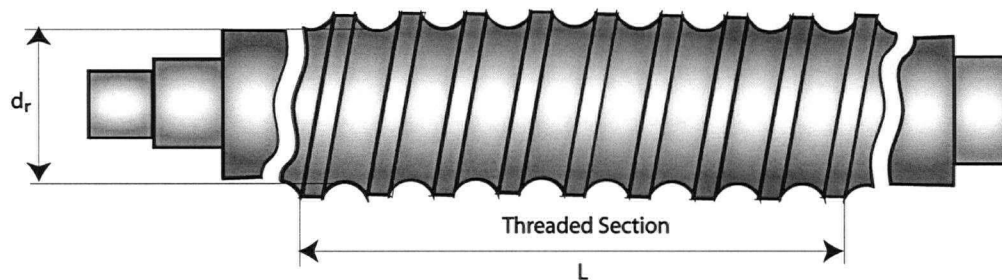


Figure 3.4: Ballscrew Geometry

However, previous researchers [42] have found out that the threads do not make any substantial contribution to the stiffness of the ballscrew; although, they affect its inertia properties significantly. Consequently, the threaded section can be approximated using beam elements by introducing the mass of the threads into the mass matrix calculations while excluding their effects from the stiffness matrix calculations.

In order to do this, for the threaded section, the root diameter, d_r is used to derive the stiffness matrix of the finite element, while an equivalent diameter; d_e is used to calculate the mass matrix. The equivalent diameter is obtained by equating the mass of a cylinder having a diameter, d_e to the mass of the threaded section including the threads. It is expressed as,

$$d_e = \sqrt{\frac{4 \left(\frac{\pi d_r^2}{4} L + V_{threads} \right)}{\pi L}} \quad (3.1)$$

where L represents the length of the threaded section, and $V_{threads}$ is the total volume of the threads which can be estimated from the geometry of the thread.

The Timoshenko beam element is preferred over its Euler-Bernoulli counterpart because it considers shear effects in its bending deformation formulations. Stemming from this, the Timoshenko beam elements yield more accurate results at higher frequencies, than the Euler-Bernoulli beam elements. Furthermore, they can be used to model short and stubby beams more accurately.

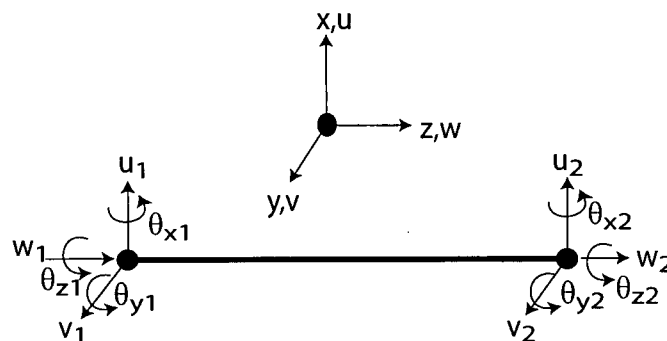


Figure 3.5: Timoshenko Beam Element

Each beam element has six DOF on each of its two nodes; three translations, u , v , w , and three rotations θ_x , θ_y , θ_z , as shown in Figure 3.5. Each section of the ballscrew is divided into equal-sized elements. Element sizes with a length-diameter ratio of 0.3-0.5 have been found to give reasonably consistent results. The expressions for the element stiffness and mass matrices of a Timoshenko beam are given in Appendix A.

3.3.2 Rotor, Nut and Table

The rotor, nut and table, being relatively more rigid than other elements such as the ballscrew and joint interfaces, are adequately approximated by lumped inertia properties defined at their Centres of Mass (COM). In the most general case, the model for each of these elements consists of a mass matrix comprising a translating mass, m , and nine rotary inertias (I_{xx} , I_{yy} , I_{zz} , I_{xy} , I_{yx} , I_{xz} , I_{zx} , I_{yz} and I_{zy}) expressed in matrix form as,

$$\mathbf{M} = \begin{bmatrix} m & 0 & 0 & 0 & 0 & 0 \\ 0 & m & 0 & 0 & 0 & 0 \\ 0 & 0 & m & 0 & 0 & 0 \\ 0 & 0 & 0 & I_{xx} & I_{xy} & I_{xz} \\ 0 & 0 & 0 & I_{yx} & I_{yy} & I_{yz} \\ 0 & 0 & 0 & I_{zx} & I_{zy} & I_{zz} \end{bmatrix} \quad (3.2)$$

However, in specific cases like the case of the rotor which is assumed to only rotate about the z-axis (i.e. axis of rotation), the mass matrix given in Eq.(3.2) can be reduced such that only I_{zz} is retained. Furthermore, in cases where information in the form of displacements and forces are desired at locations other than the COM, as depicted in Figure 3.6, rigid-body transformations can be used to map the information at the COM to the desired location, P.

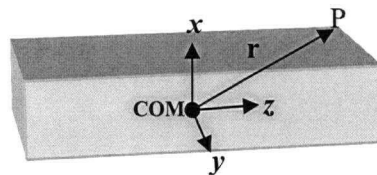


Figure 3.6: Rigid-body Transformations from the COM to any Point P

The transformation matrix, T_{P-COM} of displacements from the COM to P is derived as,

$$\begin{Bmatrix} \mathbf{u} \\ \boldsymbol{\theta} \end{Bmatrix}_P = \underbrace{\begin{bmatrix} \mathbf{I}_{3 \times 3} & -S(\mathbf{r}) \\ \mathbf{0}_{3 \times 3} & \mathbf{I}_{3 \times 3} \end{bmatrix}}_{\mathbf{T}_{P-COM}} \begin{Bmatrix} \mathbf{u} \\ \boldsymbol{\theta} \end{Bmatrix}_{COM} \quad (3.3)$$

where \mathbf{u} and $\boldsymbol{\theta}$ are the displacement and rotation vectors at a given location, expressed as $\mathbf{u} = \{u_x \ u_y \ u_z\}^T$ and $\boldsymbol{\theta} = \{\theta_x \ \theta_y \ \theta_z\}^T$, respectively. \mathbf{r} is the position vector from the COM to point P given by, $\mathbf{r} = \{r_x \ r_y \ r_z\}^T$ while $S(\mathbf{r})$ is the tensorial representation of \mathbf{r} given by,

$$S(\mathbf{r}) = \begin{bmatrix} 0 & -r_z & r_y \\ r_z & 0 & -r_x \\ -r_y & r_x & 0 \end{bmatrix} \quad (3.4)$$

The transformations used here are based on small angle rotations, since the components for which these transformations are required, namely the table and nut, do not undergo large rotations, because their only rigid-body motions are translations along the feed axis.

The generalized force vector, $\mathbf{F}_P = \{F_x \ F_y \ F_z \ M_x \ M_y \ M_z\}^T$, consisting of forces and moments applied at point P, can also be transformed from the point P to the COM by using the transpose of the transformation matrix, T_{P-COM} as,

$$\mathbf{F}_{COM} = \mathbf{T}_{P-COM}^T \mathbf{F}_P \quad (3.5)$$

3.3.3 Couplings, Bearings, Fasteners and Guideways

Joint interfaces such as couplings, bearings, fasteners and guideways are typically areas of significant compliance; therefore they play an important role in the dynamics of any mechanical system. Even though some of these elements show varying degrees of non-linear characteristics, it is customary to model them using linear spring elements. More details about the modeling of these joint interfaces are presented in the following sub-sections.

3.3.3.1 Couplings

Couplings used in machine tool feed drives vary in design. Some of the commonly used designs include jaw couplings, bellow-type couplings and disc servo couplings. However, irrespective of the design, one of the most desirable characteristic in such couplings is a high torsional stiffness, because this property plays an important role in the feed drive's dynamics. Therefore, ballscrew drive couplings are usually modeled as torsional springs with a spring constant which can be readily obtained from manufacturer catalogs.

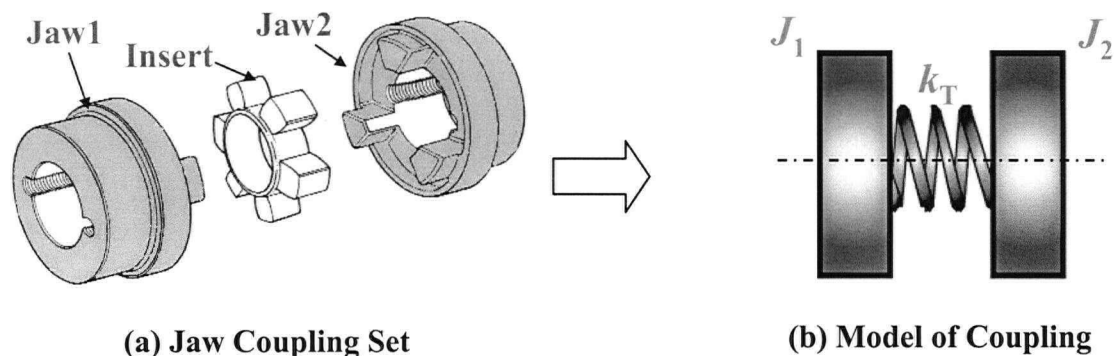


Figure 3.7: Model of a Typical Coupling

Figure 3.7 shows a jaw type coupling and how its compliance is modeled using a torsional spring with stiffness k_T . As shown in the figure, in situations where the coupling has significant inertia (for instance the jaw inertias in this case), these properties can be lumped at either end of the torsional spring as J_1 and J_2 , and then subsequently attached to the adjoining components.

3.3.3.2 Bearings

A lot of work has been done on the modeling of bearings by previous researchers [12,21,23,30,34]. These analytical models usually take the form of simple or complex non-linear expressions for bearing stiffness as a function of applied forces, the resulting deformations, and even rotation speed, if centrifugal and gyroscopic effects are included. However, when sufficient preload is applied and the rotation speeds are moderate, the non-linearity in the bearing stiffness can be neglected such that a stiffness value can be assigned to the bearing for a given preload. This information is usually available in manufacturer catalogs for various bearing types and arrangements. For angular thrust bearings, stiffness

data are available as an axial stiffness and radial stiffness as shown in Figure 3.3, while for radial bearings, they are expressed as a single radial stiffness.

As an alternative to the information provided in the bearing catalogs, bearing stiffness could be measured in various ways [19,24] or obtained using dedicated software [6,44].

3.3.3.3 Fasteners

A variety of fasteners are used joint components in a feed drive system. However, only few of these have to be considered in the model because most of them do not play a significant role in the machine's dynamics. Generally, any fastener which is considered weak enough to constitute a significant compliance between two components should be included in the model.

One fastened joint which often falls into the aforementioned category is that between the nut and table in a feed drive system. This is because the table is usually heavy; therefore the joint linking the nut to it undergoes appreciable deformations.

The most commonly used fastener in machine tool feed drives is the nut and bolt which is conveniently modeled as a linear spring having a stiffness which comprises the stiffness of the bolt and that of the bolted members combined in series. This stiffness can be calculated given all material and geometric properties of the bolts and members as explained in [41].

Experimental measurement of the joint stiffness can also be performed as an alternative to analytic methods [39].

3.3.3.4 Guideways

Traditionally, CNC machine tables have been guided using the so called *boxways* consisting of precision-ground surfaces, which provide reference edges along which the table slides. These box ways typically come in various designs, typical of which are the *dove-tail* and *square-edge* configurations.

Even though box ways are simple in operation and design, they are plagued by certain limitations like high friction and low speed capability which have made them unsuitable for high-speed machine tools. Consequently, linear guides are preferred for such machines tools.

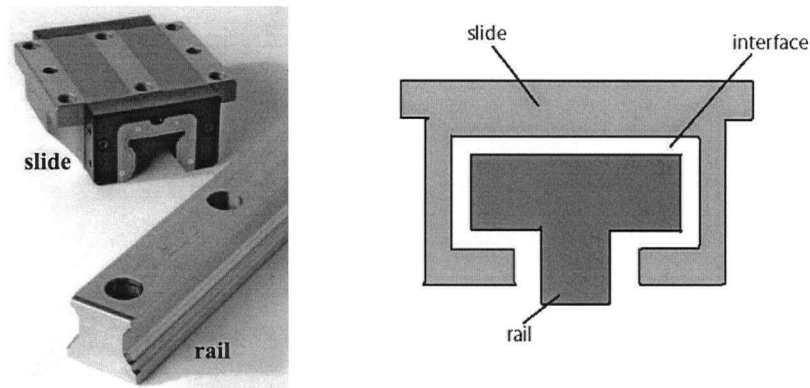


Figure 3.8: A Linear Guide Unit Consisting of a Slide and Rail

Figure 3.8 shows a typical linear guide unit which consists of a slide and rail assembled together. Depending on how the interface between the slide and rail is filled, the linear guides can be categorized as either hydrostatic or anti-friction guideways. The hydrostatic guideways employ a pressurized fluid film at the interface to reduce friction, thereby increase achievable speeds. In the case of anti-friction guideways, rollers are inserted at the interface to achieve the same purpose.

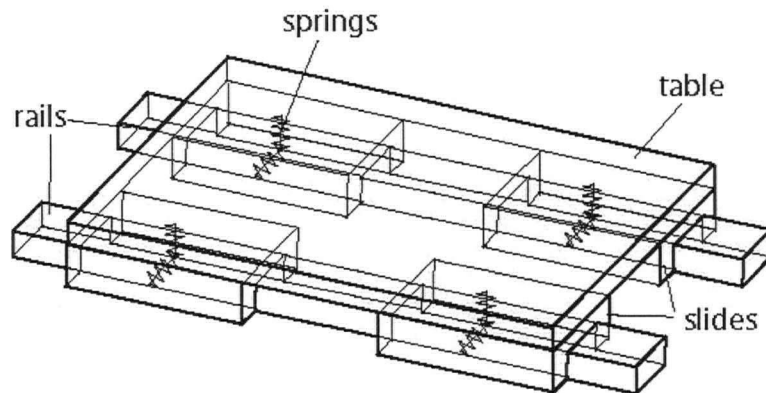


Figure 3.9: Model of Linear Guides using Vertical and Lateral Springs

Linear guides are typically modeled as linear springs in the vertical and lateral directions as shown in Figure 3.9. Even though each unit has stiffness in the three rotational directions, these are not considered since machine tools generally use two rails and four slides as shown in the figure. The stiffness constants for the springs are usually provided in manufacturers'

catalogs as a function of preload force and pressure for the anti-friction and hydrostatic guides, respectively.

3.3.4 Screw-Nut Interface

The screw-nut interface of a ballscrew drive is very important because it is where rotary motion and torques from the ballscrew are converted to linear motion and thrust that is transmitted to the table. Even though functionally similar to the interface in conventional leadscrews, the distinguishing feature in the case of a ballscrew is that balls are inserted at this interface in order to convert the sliding friction present in leadscrews to rolling friction. Due to this improvement, up to 98% reduction in friction and a proportionate increase in efficiency are achieved [33].

Moreover, a preload is often applied at this interface in order to mitigate backlash effects and increase the rigidity of the drive. Three types of preload mechanisms are typical in machine tool feed drives. They are the spacer, offset and oversize-ball preload [33].

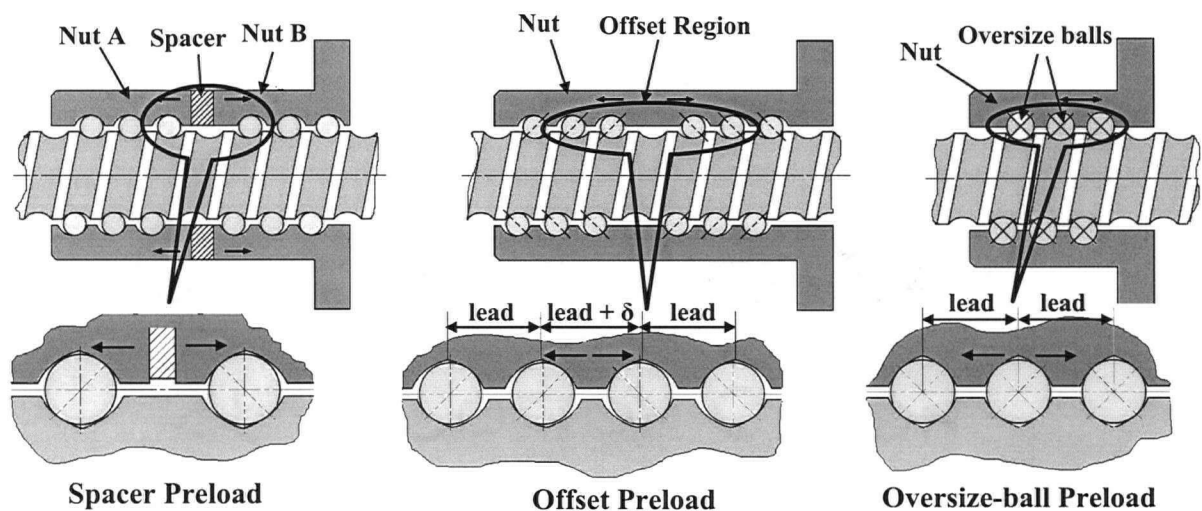


Figure 3.10: Common Preload Mechanisms used in Machine Tool Feed Drives

As shown in Figure 3.10, in the spacer preload mechanism, a spacer is inserted between two nuts in order to apply a preload. By varying the thickness of the spacer, the preload applied to the interface can be conveniently adjusted. In the offset preload, instead of two nuts, only one nut is used. However the lead is increased by a small amount, δ in the middle portion of the nut in order to achieve the same preloading effect as the spacer. In the

oversize-ball preload, as the name suggests, the balls are made a little larger in size than the grooves thereby creating a preload force at the interface.

At this juncture, it is necessary to mention that in the first two preload mechanisms, each ball has a two-point contact, while in the third, the contact is four-point (see Figure 3.10). In the mechanisms with two-point contact, half of the balls contact the ballscrew at the lower (right) side of its thread, while the other half make contact with the ballscrew thread on its upper (left) side. On the other hand, in the case of the oversize-ball preload, all the balls in contact make contact with both the lower and upper side of the ballscrew thread. The nature of the contact plays an influential role in the interface model explained in following sections.

3.3.4.1 Modeling of Interface Stiffness

In modeling the screw-nut interface, the mass of the balls is assumed to be negligible, while all the compliance is assumed to come from their point of contact with the screw and nut. Therefore, the balls are modeled as massless springs having a stiffness k_{Ball} aligned along the common line of contact (contact normal) between screw and nut as depicted in Figure 3.11.

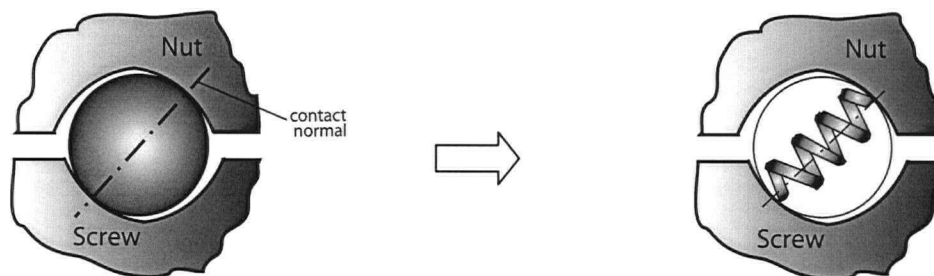


Figure 3.11: Spring Model of Balls in the Screw-Nut Interface

However, in order for this stiffness for each ball to be applied to the FE beam model of the ballscrew and lumped-inertia model of the nut, it has to undergo a two-stage transformation. The first stage of the transformation is necessary in order to convert k_{Ball} from a local coordinate system established for each ball, to the global coordinate system defined for the ballscrew drive as shown in Figure 3.5. Then, the second stage of the transformation is developed in order to lump the stiffness of all the balls distributed all around the screw-nut interface such that they can be connected to the nut node, and to one or more nodes on the ballscrew. The stiffness matrices for the screw-nut interface are then obtained by applying

this two-stage transformation to k_{Ball} . Sections 3.3.4.2 to 3.3.4.5 present a detailed explanation of these steps.

3.3.4.2 First Stage of Transformation: Local to Global Coordinates

In order to derive this transformation, it is necessary to define the orientation of the contact normal along which the spring stiffness described above is aligned. This orientation is best described by the two angles α and β shown in Figure 3.12.

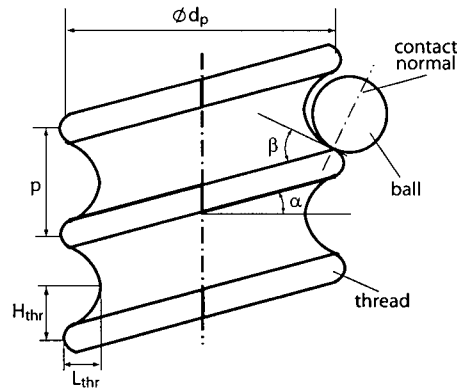


Figure 3.12: Orientation of Contact Normal

Here, α is the pitch angle of the ballscrew given by the expression,

$$\alpha = \tan^{-1} \left(\frac{p}{\pi d_p} \right) \quad (3.6)$$

where p is the pitch and d_p is the pitch diameter of the ballscrew. β , on the other hand, is the mean thread angle at the ball contact point. H_{thr} and L_{thr} are the height and length of the thread, respectively.

In order to simplify the analysis, the ballscrew thread is unwrapped and represented as a double-inclined plane, inclined at angles α and β , as shown in Figure 3.13(a). Two coordinate systems, CS_{1L} and CS_{2L} , are attached to the centre of each ball resting on the plane. CS_{1L} is aligned such that its z-axis points along the contact line of the ball, normal to the plane (i.e. the direction of k_{Ball}), while CS_{2L} is established so that its z-axis is parallel to the ballscrew's axis (global z-axis), and its y-axis lies along the radial line from the ball's centre to the axis of the ballscrew (see Figure 3.14 for clarity).

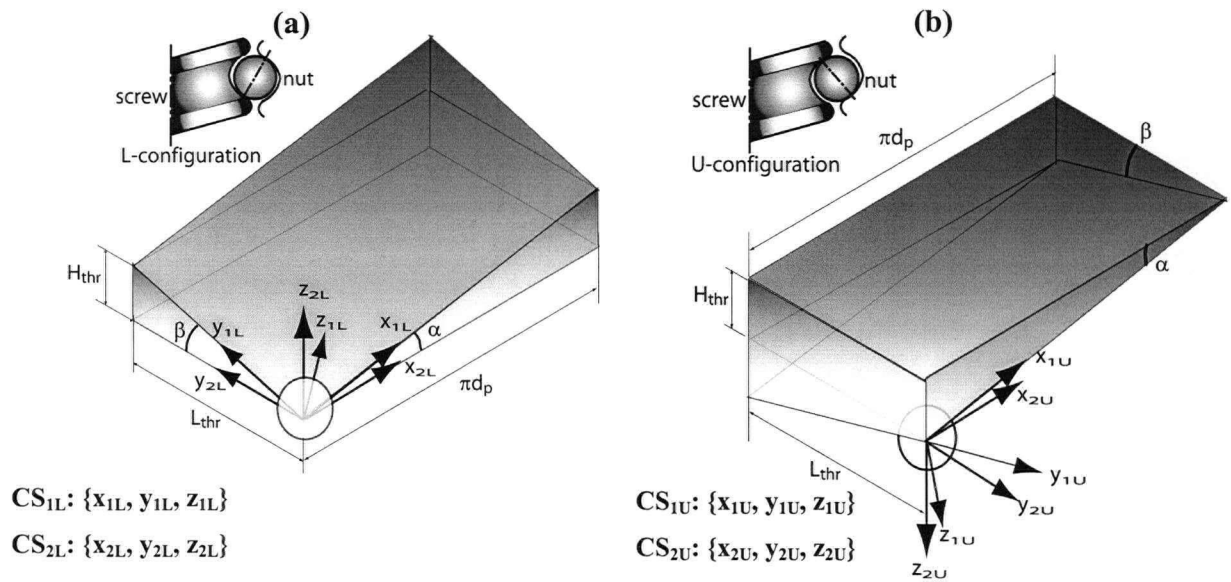


Figure 3.13: Inclined Plane Representation of Ballscrew Thread

The coordinates, CS_{1U} and CS_{2U} on Figure 3.13(b) are established following the same logic, except that they represent the case where the ball-contact configuration is reversed as shown in the figure. The subscripts L and U are used to differentiate the ball-contact configurations as “lower” and “upper” respectively.

For the L-configuration, the transformation T_{2L-1L} that obtains CS_{2L} from CS_{1L} is derived by a current-frame rotation of $-\alpha$ and β about the y and x -axis, respectively. This is represented mathematically as,

$$T_{2L-1L} = Rot_y(-\alpha) \cdot Rot_x(\beta) \quad (3.7)$$

where Rot represents a rotation matrix about the axis specified by the accompanying subscript. Their expressions and some information about current-frame rotations are given in Appendix A.

The transformation T_{2U-1U} , which obtains CS_{2U} from CS_{1U} is calculated in a similar fashion, except this time the current-frame rotation is first α about the y -axis and then $-\beta$ about the x -axis. The mathematical expression is given by,

$$T_{2U-1U} = Rot_y(\alpha) \cdot Rot_x(-\beta) \quad (3.8)$$

Since the spring deformation always occurs along the z_1 -axis in both configurations, then the transformations T_{2L-z1L} and T_{2U-z1U} are given by post-multiplying T_{2L-1L} and T_{2U-1U} by a unit vector in the z_1 -direction, as,

$$\begin{aligned} T_{2L-z1L} &= T_{2L-1L} \cdot \{0 \ 0 \ 1\}^T \\ T_{2U-z1U} &= T_{2U-1U} \cdot \{0 \ 0 \ 1\}^T \end{aligned} \quad (3.9)$$

Here T_{2L-z1L} is the transformation which obtains CS_{2L} from z_{1L} , while T_{2U-z1U} is the transformation that obtains CS_{2U} from z_{1U} . To avoid repetition, this same notation is used for all the transformation matrices in this chapter.

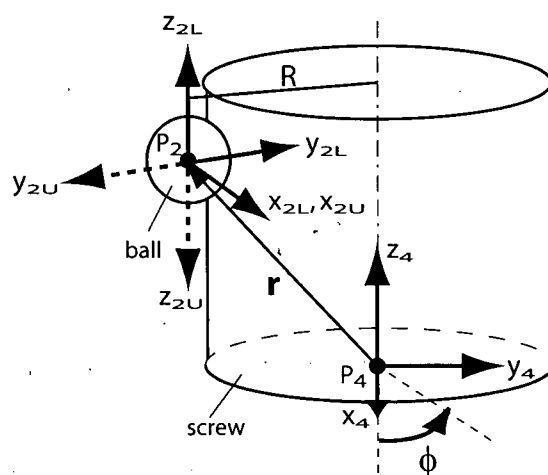


Figure 3.14: Relationship between Ball Coordinates and Screw Coordinates

Figure 3.14 shows the relationship between the previously described coordinate systems CS_{2L} and CS_{2U} and a new coordinate system, CS_4 . CS_4 is centered at a specified point, P_4 along the axis of the screw, and aligned in such a way that its three axes are parallel to the global axes of the ballscrew drive shown in Figure 3.5. Another coordinate system CS_3 (not shown in the figure) is established such that it has all its axes parallel to CS_4 but its origin is located at the centre of each ball. In other words, CS_3 is a ball-centered global coordinate system. The transformation T_{3-2L} is simply a rotation about the z_3 -axis (or z_4 -axis) by an amount ϕ . Here the azimuth angle, ϕ represents the angle measured in the counter-clockwise direction from the x_3 -axis (or x_4 -axis) to the x_{2L} or x_{2U} -axis. As will be explained later, the angle ϕ specifies the location of the centre of each ball along the ballscrew thread.

In order to obtain T_{3-2U} , first the y_{2U} and z_{2U} -axes are flipped by using a Boolean matrix so that they coincide with their corresponding axes in CS_{2L} . This is then followed by a rotation about the z_3 -axis by the angle ϕ . Mathematically, these transformations are expressed as,

$$\begin{aligned} T_{3-2L} &= Rot_z(\phi) \\ T_{3-2U} &= Rot_z(\phi) \cdot \begin{bmatrix} 1 & 0 & 0 \\ 0 & -1 & 0 \\ 0 & 0 & -1 \end{bmatrix} \end{aligned} \quad (3.10)$$

Therefore, the transformation from each local coordinate system to the global coordinate system, for the L and U-configurations, T_{3-z1L} and T_{3-z1U} , are given by multiplying all the transformations described above as,

$$\begin{aligned} T_{3-z1L} &= T_{3-2L} \cdot T_{2L-z1L} \\ T_{3-z1U} &= T_{3-2U} \cdot T_{2U-z1U} \end{aligned} \quad (3.11)$$

It is worth mentioning here that since these transformation matrices are orthonormal, the inverse transformations T_{z1L-3} and T_{z1U-3} are simply given by the transpose of their corresponding forward transforms, T_{3-z1L} and T_{3-z1U} .

3.3.4.3 Second Stage of Transformation: Lumping to Nodes

It is obvious from the previous section that each ball in the screw-nut interface has a unique local-global transformation matrix which depends on its contact configuration (L or U) and its azimuth angle, ϕ (Figure 3.14). However, the nut is modeled as a lumped mass represented by a single node located at its COM, while the ballscrew, being an FE beam, has discrete nodes along its axis. The aim of the lumping explained in this section is therefore to develop transformation matrices between the ball-centered global coordinate systems for each ball, to node-centered global coordinate systems attached to the nut and ballscrew nodes. This way, the ball stiffness matrices distributed all around the contact interface can be connected to the nodes of the nut and ballscrew.

Two methods have been developed here in order to perform this lumping – the Rigid-Ballscrew Method and the Shape-Function Method. They are described in detail below.

(A) Rigid-Ballscrew Method

In this method, the region of the ballscrew within the screw-nut interface is assumed to move as a rigid body. In other words, as shown in Figure 3.15, the motion of the screw is assumed to be characterized by a translation u_{BS} measured at a point P located within the nut, and a rotation θ_{BS} . Point P is the origin of the CS coordinate system, and represents a node on the ballscrew. Since the nut is also modeled as a rigid body, it translates and rotates by an amount u_N and θ_N measured from P , respectively. For convenience, P is chosen to coincide with the COM (node) of the nut, since this is where all its inertia properties are lumped. r is the position vector measured from P to the centre of any of the balls in the interface.

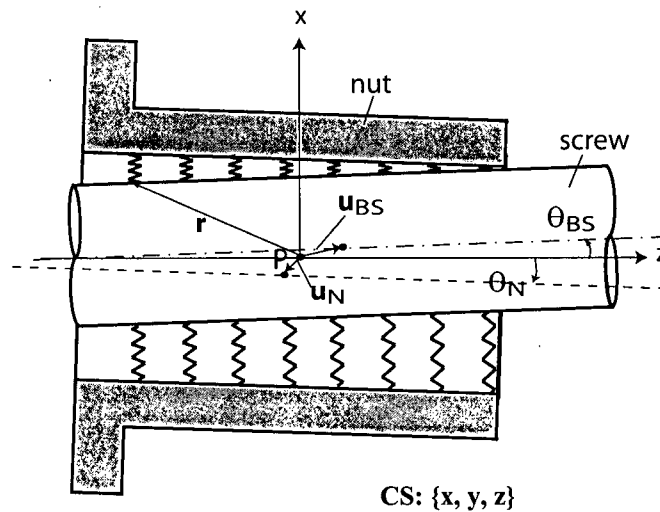


Figure 3.15: Rigid-Ballscrew Method

If the coordinate system, CS_4 in Figure 3.14 is chosen such that it coincides with CS , then the position vector, r for each ball can be expressed as a function of ϕ as,

$$\mathbf{r} = \begin{Bmatrix} r_x \\ r_y \\ r_z \end{Bmatrix} = \begin{Bmatrix} R \sin(\phi) \\ -R \cos(\phi) \\ r_g \phi \end{Bmatrix} \quad (3.12)$$

This function is derived from the parametric equation of helix having a pitch, p equal to the pitch of the ballscrew. R is the constant radius measured from the axis of the screw to the centre of each ball while r_g is the gear reduction ratio of the ballscrew given by,

$$r_g = \frac{P}{2\pi} \quad (3.13)$$

Figure 3.16 shows the relationship between r , r_N and r_{BS} for the L and U-Configurations. r_N and r_{BS} are the position vectors measured from P to the ball-nut and ball-screw contact points, P_N and P_{BS} , of each ball, respectively.

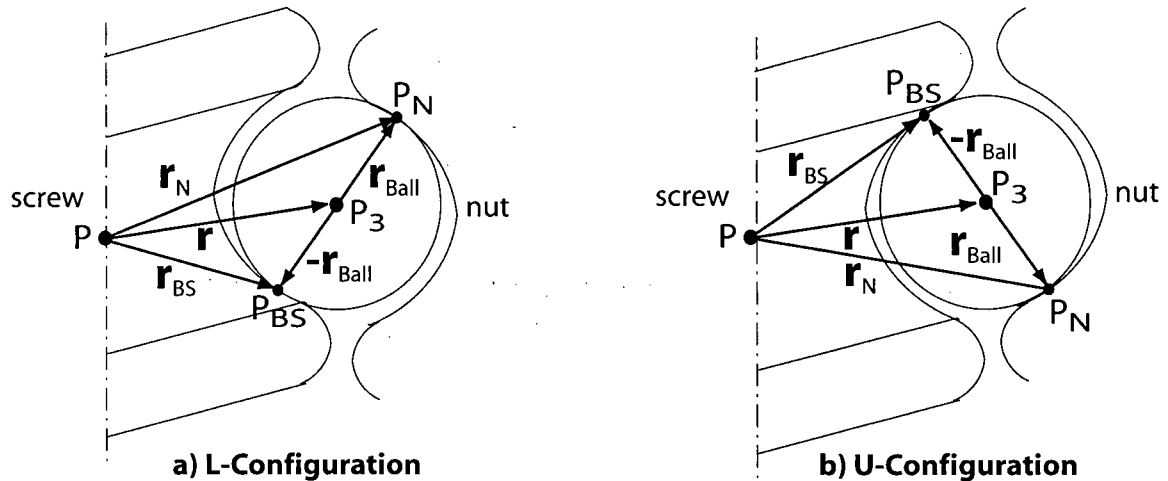


Figure 3.16: Position Vectors for Ball Contact Points

If r_{Ball} is defined as the position vector from the ball's centre, P_3 to P_N for both the L and U-Configurations, then r_{BS} and r_N are given by,

$$\begin{aligned} r_{BS} &= r - r_{Ball} \\ r_N &= r + r_{Ball} \end{aligned} \quad (3.14)$$

The vector r_{Ball} for the L and U-Configurations is obtained by transforming the radius of the ball, R_{Ball} , to the global coordinates using T_{3-z1L} and T_{3-z1U} , as,

$$r_{Ball} = \begin{cases} T_{3-z1L} \cdot R_{Ball} & \text{for the L-Configuration} \\ T_{3-z1U} \cdot R_{Ball} & \text{for the U-Configuration} \end{cases} \quad (3.15)$$

Since the ballscrew and nut are considered rigid bodies, and the rotations involved in vibratory motions are small, the transformations, $T_{3-B S}$ and T_{3-N} between the displacements in CS_3 , and displacements and rotations in CS , for the nut and ballscrew can then be written as,

$$\mathbf{u}_{3BS} = \underbrace{\begin{bmatrix} \mathbf{I}_{3 \times 3} & -S(\mathbf{r}_{BS}) \end{bmatrix}}_{\mathbf{T}_{3-BN}} \begin{Bmatrix} \mathbf{u}_{BS} \\ \theta_{BS} \end{Bmatrix} \tag{3.16}$$

$$\mathbf{u}_{3N} = \underbrace{\begin{bmatrix} \mathbf{I}_{3 \times 3} & -S(\mathbf{r}_N) \end{bmatrix}}_{\mathbf{T}_{3-N}} \begin{Bmatrix} \mathbf{u}_N \\ \theta_N \end{Bmatrix}$$

Here \mathbf{u}_{3BS} and \mathbf{u}_{3N} are the displacements of P_{BS} and P_N measured in the CS_3 coordinate system. $S(\cdot)$ is a function which converts the vector enclosed in the parenthesis to its tensorial form as explained in Section 3.3.2.

Therefore, using the transformations \mathbf{T}_{3-BN} and \mathbf{T}_{3-N} , displacements at the ball-screw and ball-nut contact points for all balls can be combined into equivalent nodal displacements and rotations at a point, P for the ballscrew and nut, respectively.

(B) Shape-Function Method

In the Rigid-Ballscrew Method described above, it was assumed that the section of the ballscrew within the screw-nut interface acts as a rigid body. However, in some cases where the nut is significantly long, for instance in the spacer and offset preload mechanisms, this assumption may not be realistic since the ballscrew may undergo significant deformations within the screw-nut interface. In such cases, the Shape-Function Method described in this section provides a more realistic means of lumping the distributed interface stiffness unto the ballscrew nodes.

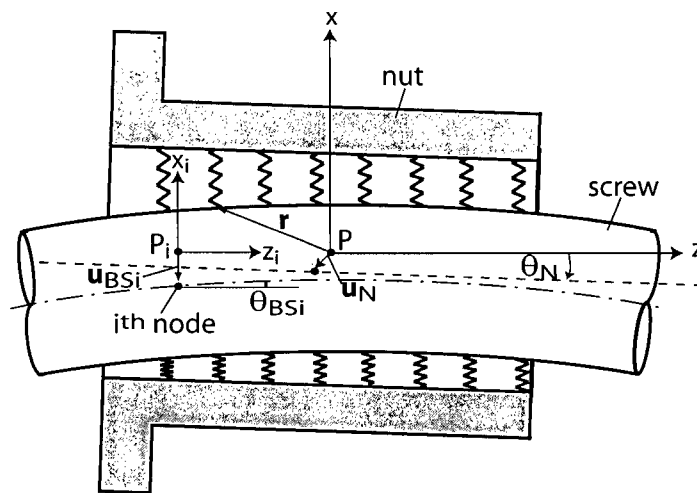


Figure 3.17: Shape-Function Method

Figure 3.17 gives a pictorial representation of the Shape-Function Method. As shown, the nut is still assumed to perform a rigid-body translation and rotation, \mathbf{u}_N and $\boldsymbol{\theta}_N$ measured from P . However, this time, the deformations of the ballscrew at each of its N_{Node} nodes within the screw-nut interface are considered. A new global coordinate system CS_i , centered at point P_i , the undeformed location of the i^{th} node of the ballscrew, has also been established. Here, \mathbf{u}_{BSi} and $\boldsymbol{\theta}_{BSi}$ are the translational and rotational displacements of the i^{th} node.

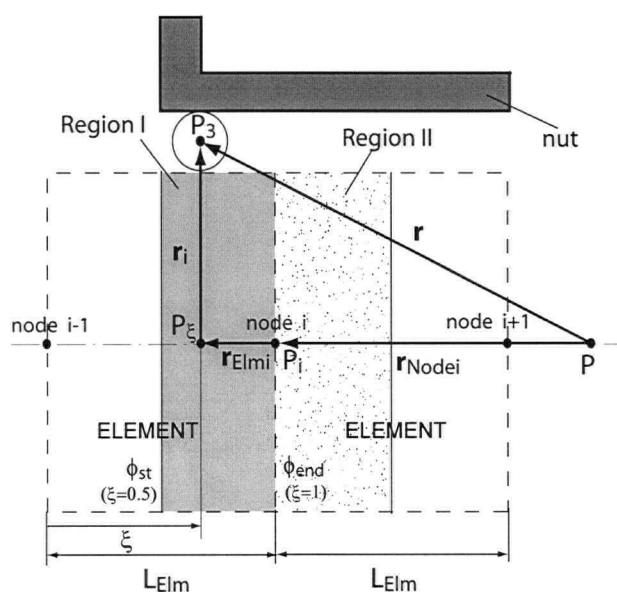


Figure 3.18: More Details of Shape-Function Method

Figure 3.18 shows a more detailed representation of the method for two adjacent FE beam elements of the ballscrew. The coordinate axes have been omitted for clarity. Here, it is assumed, without loss of generality, that the elements within the screw-nut interface have equal lengths, L_{Elm} . ξ is the non-dimensional distance measured from the left to the right node of each element such that its value ranges from 0 to 1 for a distance 0 to a distance L_{Elm} . The node of interest is labeled as the i^{th} node, while the nodes to its left and right are respectively labeled as the $i-1^{th}$ and $i+1^{th}$ nodes.

In addition to the position vector \mathbf{r} explained above, three more position vectors have been introduced here. \mathbf{r}_{Nodei} is the vector from P to the location of the node of interest P_i , \mathbf{r}_{Elmi} is the vector from P_i to an arbitrary point P_ξ within the region around each node, while \mathbf{r}_i is the vector from P_ξ to P_3 , the location of the centre of any particular ball in the interface. A

global coordinate system, CS_ξ (not shown in the figure) is established at every point P_ξ from which the displacements, $\mathbf{u}_{BS\xi}$ and rotations, $\theta_{BS\xi}$ of the ballscrew are measured. Furthermore, similar to the coordinate system CS_i , established on the i^{th} node, CS_{i-1} and CS_{i+1} have been established on the $i-1^{th}$ and $i+1^{th}$ nodes, respectively.

The region around each node is divided into two. Region I is the portion to the left of the i^{th} node up to halfway into the element on its left, while Region II is the portion on its right up to halfway into the element on the right. These two regions have to be considered separately in the analysis.

In Region I, the vector \mathbf{r}_{Elmi} is always pointing in the negative z-direction. Hence it is given by,

$$\mathbf{r}_{Elmi} = r_{Elmi} \cdot \{0 \quad 0 \quad -1\}^T \quad (3.17)$$

where r_{Elmi} is the scalar distance from P_i to P_ξ , given as a function of ξ by,

$$r_{Elmi} = L_{Elm}(1 - \xi) \quad (3.18)$$

But ξ is linearly dependent on the azimuth angle ϕ , and so can be expressed by the linear function,

$$\begin{aligned} \xi &= m\phi + c \\ m &= \frac{1}{2(\phi_{end} - \phi_{st})}; \quad c = 1 - m\phi_{end} \end{aligned} \quad (3.19)$$

ϕ_{st} and ϕ_{end} here are the azimuth angles at the start and end of Region I (Figure 3.18).

For Region II, the derivations follow the same pattern, except that \mathbf{r}_{Elmi} is now always in the positive z-direction. It is given by,

$$\mathbf{r}_{Elmi} = r_{Elmi} \cdot \{0 \quad 0 \quad 1\}^T \quad (3.20)$$

This time r_{Elmi} is expressed as,

$$r_{Elmi} = L_{Elm}\xi \quad (3.21)$$

while the constants c and m in the linear function relating ξ to ϕ is given by,

$$m = \frac{1}{2(\phi_{end} - \phi_{st})}; \quad c = -m\phi_{end} \quad (3.22)$$

This time, ϕ_{st} and ϕ_{end} are the azimuth angles at the start and end of Region II.

The vector r_{Nodei} is also always directed along the z-axis. However, its sense depends on the sign of the azimuth angle, ϕ_i , at the node of interest. Hence it is expressed for both regions as,

$$r_{Nodei} = r_{Nodei} \cdot \{0 \quad 0 \quad \text{sgn}(\phi_i)\}^T \quad (3.23)$$

Similar to the r_{Elmi} case, r_{Nodei} is the scalar displacement between P and P_i .

The vector r_i can then be expressed in terms of r_{Elmi} , r_{Nodei} and r , for both regions as,

$$r_i = r - r_{Nodei} - r_{Elmi} \quad (3.24)$$

Following the explanation in the previous method, the vectors r_{BSi} and r_N respectively from P_ξ and P , to the screw and nut contact points, as opposed to the ball-centre, can be obtained from the vectors r_i and r as,

$$\begin{aligned} r_{BSi} &= r_i - r_{Ball} \\ r_N &= r + r_{Ball} \end{aligned} \quad (3.25)$$

where r_{Ball} retains its definition as given by Eq.(3.15). This expression holds true for both regions.

From the above derivations, it can be seen that since the flexibility of the ballscrew at every point is considered, the transformation matrix given for the ballscrew in Eq.(3.16) for the rigid-ballscrew method, now becomes a transformation between displacements in CS_3 to displacements and rotations in CS_ξ . This transformation, $T_{3-BS\xi}$ for both regions becomes,

$$u_{3BS} = \underbrace{\begin{bmatrix} I_{3 \times 3} & -S(r_{BSi}) \end{bmatrix}}_{T_{3-BS\xi}} \begin{Bmatrix} u_{BS\xi} \\ \theta_{BS\xi} \end{Bmatrix} \quad (3.26)$$

The transformation T_{3-N} for the nut remains the same.

In order to lump the distributed stiffness on the ballscrew side, another transformation is needed between CS_ξ and the global coordinate systems attached to the nodes. This is achieved by making use of the Shape-Function Matrix for the FE Beam Element given by,

$$T_{BS\xi-BSi} = \begin{bmatrix} N_{ux1} & 0 & 0 & 0 & N_{ux2} & 0 & N_{ux3} & 0 & 0 & 0 & N_{ux4} & 0 \\ 0 & N_{uy1} & 0 & N_{uy2} & 0 & 0 & 0 & N_{uy3} & 0 & N_{uy4} & 0 & 0 \\ 0 & 0 & N_{uz1} & 0 & 0 & 0 & 0 & 0 & N_{uz2} & 0 & 0 & 0 \\ 0 & N_{\theta x1} & 0 & N_{\theta x2} & 0 & 0 & 0 & N_{\theta x3} & 0 & N_{\theta x4} & 0 & 0 \\ N_{\theta y1} & 0 & 0 & 0 & N_{\theta y2} & 0 & N_{\theta y3} & 0 & 0 & 0 & N_{\theta y4} & 0 \\ 0 & 0 & 0 & 0 & 0 & N_{\theta z1} & 0 & 0 & 0 & 0 & 0 & N_{\theta z2} \end{bmatrix} \quad (3.27)$$

The expression for the Shape-Function matrix, $T_{BS\xi-BSi}$ given in Eq.(3.27) is valid both Regions I and II. Its elements are all functions of ξ , and they represent spatial interpolation functions from displacements and rotations at the two nodes of an FE beam element to displacements and rotations anywhere within the element. The expressions for these functions are presented in Appendix A.

Since the Shape-Function matrix is only valid for the nodes of a particular element, in Region I, it a transformation from CS_{i-1} and CS_i to CS_ξ while in Region II it is from CS_i and CS_{i+1} to CS_ξ . Mathematically, this is expressed as,

$$\begin{cases} \mathbf{u}_{BS\xi} \\ \boldsymbol{\theta}_{BS\xi} \end{cases} = T_{BS\xi-BSi} \begin{cases} \mathbf{u}_{BSi-1} \\ \boldsymbol{\theta}_{BSi-1} \\ \mathbf{u}_{BSi} \\ \boldsymbol{\theta}_{BSi} \end{cases} \quad \text{for Region I} \quad (3.28)$$

$$\begin{cases} \mathbf{u}_{BS\xi} \\ \boldsymbol{\theta}_{BS\xi} \end{cases} = T_{BS\xi-BSi} \begin{cases} \mathbf{u}_{BSi} \\ \boldsymbol{\theta}_{BSi} \\ \mathbf{u}_{BSi+1} \\ \boldsymbol{\theta}_{BSi+1} \end{cases} \quad \text{for Region II}$$

Hence the transformation between CS_3 and the node-centered global coordinate systems CS_{i-1} , CS_i and CS_{i+1} for the ballscrew is given by,

$$\begin{aligned}
 \mathbf{u}_{3BS} &= \underbrace{\begin{bmatrix} \mathbf{T}_{3-BS\xi} \cdot \mathbf{T}_{BS\xi-BSi} & \mathbf{0}_{3 \times 6} \end{bmatrix}}_{\mathbf{T}_{3-BSi}} \cdot \begin{Bmatrix} \mathbf{u}_{BSi-1} \\ \theta_{BSi-1} \\ \mathbf{u}_{BSi} \\ \theta_{BSi} \\ \mathbf{u}_{BSi+1} \\ \theta_{BSi+1} \end{Bmatrix} && \text{for Region I} \\
 \mathbf{u}_{3BS} &= \underbrace{\begin{bmatrix} \mathbf{0}_{3 \times 6} & \mathbf{T}_{3-BS\xi} \cdot \mathbf{T}_{BS\xi-BSi} \end{bmatrix}}_{\mathbf{T}_{3-BSi}} \cdot \begin{Bmatrix} \mathbf{u}_{BSi-1} \\ \theta_{BSi-1} \\ \mathbf{u}_{BSi} \\ \theta_{BSi} \\ \mathbf{u}_{BSi+1} \\ \theta_{BSi+1} \end{Bmatrix} && \text{for Region II}
 \end{aligned} \tag{3.29}$$

Though these transformations are functions of ξ , they can easily be transformed into functions of ϕ by using the linear relationship between ξ and ϕ derived above.

3.3.4.4 Derivation of Interface Stiffness Matrix

After the necessary transformations between the ball-centered local coordinate system z_1 aligned in the direction of k_{Ball} , and the node-centered global coordinate systems have been obtained, the derivation of the interface stiffness matrix follows quite simply.

The stiffness matrix in the k_{Ball} direction between the screw-ball and screw-nut contact points, P_{BS} and P_N (see Figure 3.16) is given by,

$$\mathbf{K}_{Ball} = k_{Ball} \cdot \begin{bmatrix} 1 & -1 \\ -1 & 1 \end{bmatrix} \tag{3.30}$$

For the Rigid-Ballscrew Method, the transformation matrix between the displacements at P_{BS} and P_N in the z_1 coordinate direction, and the displacements and rotations at the screw node and nut node is expressed for the L-Configuration as,

$$\begin{aligned}
 \mathbf{T}_{z1L-BS} &= \mathbf{T}_{z1L-3} \cdot \mathbf{T}_{3-BS} \\
 \mathbf{T}_{z1L-N} &= \mathbf{T}_{z1L-3} \cdot \mathbf{T}_{3-N}
 \end{aligned} \tag{3.31}$$

Similarly, for the U-Configuration, the transformations are given by,

$$\begin{aligned} \mathbf{T}_{z1U-BS} &= \mathbf{T}_{z1U-3} \cdot \mathbf{T}_{3-BS} \\ \mathbf{T}_{z1U-N} &= \mathbf{T}_{z1U-3} \cdot \mathbf{T}_{3-N} \end{aligned} \quad (3.32)$$

As explained in Section 3.3.4.3(A), it is worth noting again that in calculating the \mathbf{r}_{Ball} used in \mathbf{T}_{3-BS} and \mathbf{T}_{3-N} , the contact configuration of the ball must also be taken into account.

The combined transformation matrix for the ballscrew and nut is given by the block diagonal matrix $\mathbf{T}_{z1L-BSN}$ for the L-Configuration, and $\mathbf{T}_{z1U-BSN}$ for the U-Configuration. Mathematically, this is expressed as,

$$\mathbf{T}_{z1L-BSN} = \begin{bmatrix} \mathbf{T}_{z1L-BS} & \mathbf{0}_{1 \times 6} \\ \mathbf{0}_{1 \times 6} & \mathbf{T}_{z1L-N} \end{bmatrix}; \quad \mathbf{T}_{z1U-BSN} = \begin{bmatrix} \mathbf{T}_{z1U-BS} & \mathbf{0}_{1 \times 6} \\ \mathbf{0}_{1 \times 6} & \mathbf{T}_{z1U-N} \end{bmatrix} \quad (3.33)$$

The screw-nut interface stiffness matrices for each ball as a function of the azimuth angle, ϕ are calculated by transforming \mathbf{K}_{Ball} . These matrices \mathbf{K}_L and \mathbf{K}_U , respectively for the L and U-Configurations are given by,

$$\mathbf{K}_L = \mathbf{T}_{z1L-BSN}^T \cdot \mathbf{K}_{Ball} \cdot \mathbf{T}_{z1L-BSN}; \quad \mathbf{K}_U = \mathbf{T}_{z1U-BSN}^T \cdot \mathbf{K}_{Ball} \cdot \mathbf{T}_{z1U-BSN} \quad (3.34)$$

Since these stiffness matrices have all been transformed into the same coordinate systems for all the balls, they can be combined by averaging each matrix over the whole motion range for the ball concerned, and then adding them all algebraically. Mathematically, this is expressed as,

$$\mathbf{K}_{SN} = \sum_{k=1}^{N_{ball}} \left(\frac{1}{\phi_{k,end} - \phi_{k,st}} \int_{\phi_{k,st}}^{\phi_{k,end}} \mathbf{K}_{L/U}(\phi) d\phi \right) \quad (3.35)$$

where \mathbf{K}_{SN} is the interface stiffness matrix and N_{Ball} is the total number of balls in contact in the interface, while $\phi_{k,st}$ and $\phi_{k,end}$ are the azimuth angles of k^{th} ball at the beginning and end of its motion range. The notation $\mathbf{K}_{L/U}$ is used to indicate a choice between \mathbf{K}_L and \mathbf{K}_U depending on the contact configuration of the k^{th} ball.

For the Shape-Function Method, the derivation follows the same sequence. To avoid repetition here, the derivations will be shown for only the L-configuration. For the U-Configuration, all that needs to be changed are the subscripts from L to U.

The transformation between the displacements at the contact points P_N and P_{BS} expressed for the Rigid-Body Method in Eq.(3.31) becomes,

$$\begin{aligned} \mathbf{T}_{z1L-BSi} &= \mathbf{T}_{z1L-3} \cdot \mathbf{T}_{3-BSi} \\ \mathbf{T}_{z1L-N} &= \mathbf{T}_{z1L-3} \cdot \mathbf{T}_{3-N} \end{aligned} \quad (3.36)$$

for the Shape-Function Method. Notice that the transformation for the nut remains the same. This is because the nut is still assumed to be a rigid-body in the Shape-Function Method.

The block diagonal matrix for the combined transformation in this case is given by,

$$\mathbf{T}_{z1L-BSiN} = \begin{bmatrix} \mathbf{T}_{z1L-BSi} & \mathbf{0}_{1 \times 6} \\ \mathbf{0}_{1 \times 12} & \mathbf{T}_{z1L-N} \end{bmatrix} \quad (3.37)$$

Using this, the i^{th} -node interface stiffness for each ball is obtained as,

$$\mathbf{K}_{Li} = \mathbf{T}_{z1L-BSiN}^T \cdot \mathbf{K}_{Ball} \cdot \mathbf{T}_{z1L-BSiN} \quad (3.38)$$

In order to combine these, again the stiffness for each ball is averaged over its motion range and then all the stiffness matrices are summed over the total number of balls. This is mathematically expressed as,

$$\mathbf{K}_{SNI} = \sum_{k=1}^{N_{Balli}} \left(\frac{1}{\phi_{ik,end} - \phi_{ik,st}} \int_{\phi_{ik,st}}^{\phi_{ik,end}} \mathbf{K}_{Li/Ui}(\phi) d\phi \right) \quad (3.39)$$

Here, \mathbf{K}_{SNI} is the interface stiffness connecting the $i-1^{th}$, i^{th} and $i+1^{th}$ nodes on the ballscrew to the nut node. N_{balli} is the number of balls in the region around the i^{th} node while $\phi_{ki,st}$ and $\phi_{ki,end}$ are the azimuth angles at the beginning and end of the motion path of the k^{th} ball within the region around the i^{th} node. Again, $\mathbf{K}_{Li/Ui}$ indicates a choice between either stiffness matrix depending on the contact configuration of the ball concerned.

Each of the N_{Node} nodes within the screw-nut interface has its \mathbf{K}_{SNI} matrix, and each matrix is derived following the steps explained above.

As can be seen, the Rigid-Body Method requires fewer computations and yields one stiffness matrix. Therefore, it provides a simple but for most cases, good enough approximation for the interface stiffness. The Shape-Function method, on the other hand,

even though more accurate, is more involved but may be necessary in situations where the Rigid-Body Method proves to be an unrealistic approximation. Therefore, by way of recommendation, it is better to consider using the Rigid-Body Method for short nuts and more rigid ballscrews, and to use the Shape-Function method for long nuts and less rigid ballscrews.

3.3.4.5 Determination of Ball Stiffness

The ball stiffness, k_{Ball} is not usually provided in the manufacturers' catalogs. However, a value is often provided for the axial stiffness of the screw-nut interface, k_{Ax} . This value can be used to calculate k_{Ball} by noting that based on the geometrical transformations described above, the direct stiffness in the axial direction always turns out to be,

$$k_{Ax} = k_{Ball} N_{Ball} \cos^2 \alpha \cos^2 \beta \quad (3.40)$$

for the spacer and offset preload mechanisms, and,

$$k_{Ax} = k_{Ball} N_{Ball} 2 \cos^2 \alpha \cos^2 \beta \quad (3.41)$$

for the oversize-balls preload mechanism because each ball consists of two springs, one in the L and the other in the U-configuration.

Consequently, given α , β and N_{Ball} , k_{Ball} can easily be estimated from k_{Ax} .

In cases where the value of k_{Ax} is not provided by the manufacturers, it can be calculated as explained in [39] based on Hertzian contact analysis as,

$$k_{Ax} = \frac{1500 N_{Ball} \cos^2 \alpha \cos^2 \beta \sqrt[3]{F_{prd}}}{C} \quad (3.42)$$

where F_{prd} [daN] is the external preload force applied to the interface and C , the elastic coefficient from Hertzian formula for contact deformation is given by,

$$C = 0.775 \sqrt[3]{\frac{E_{Ball} + E_{thr}}{E_{Ball} E_{thr}} \left(\frac{1}{R_{Ball}} - \frac{1}{R_{thr}} \right)} \quad (3.43)$$

Here, E_{Ball} and E_{thr} are the Young's Moduli for the ball and thread, while R_{Ball} and R_{thr} are the radii of curvature of the ball and thread, respectively.

3.4 Overall Structure of the Mathematical Model

At the end of all the modeling described in Section 3.3, a mathematical model is derived for the ballscrew drive which essentially consists of a mass matrix M_{model} and a stiffness matrix K_{model} for the entire model, made up of the mass and stiffness matrices of all the components in the model. The damping matrix C_{model} for the model is obtained from modal damping values obtained from experiments or experience from similar ballscrew drives. A method of transforming these modal damping constants to a damping matrix based on a proportional damping assumption is described in Appendix A.

The linear second-order differential equation for the multi-degree-of-freedom (MDOF) system is given by,

$$M_{model}\ddot{\mathbf{d}} + C_{model}\dot{\mathbf{d}} + K_{model}\mathbf{d} = \mathbf{F} \quad (3.44)$$

where \mathbf{d} is the generalized vector of displacements and rotations of all the nodes in the model, while \mathbf{F} is the generalized vector of forces applied to all the nodes in the model. From the mathematical model expressed in the above equation, information about the natural frequencies and frequency response functions (FRF) of the system can readily be obtained. This kind of information is useful for the verification of the model, as shown in Section 3.5. Furthermore, Eq.(3.44) can be converted into transfer function (TF) and state-space (SS) representations, which can be used for controller design and non-linear time-domain simulation as explained in Chapters 4 and 5, respectively.

3.5 Experimental Verification of Model

In this section, an experimental test-bed consisting of the x-axis of a 3-axis milling machine will be described, followed by a comparison of its measured to its modeled dynamics. Details on the measurement and/or estimation of the various model parameters used for the experimental test-bed are given in Appendix B.

3.5.1 Description of the Experimental Test-Bed

The experimental set-up used to verify the modeling technique presented in this chapter is the x-axis drive of the Fadal VMC 2216 three-axis milling machine shown in Figure 3.19.

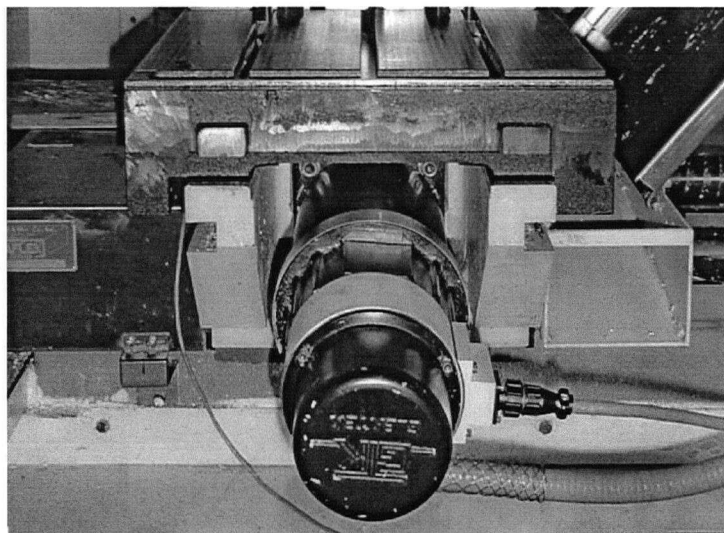


Figure 3.19: Experimental Test-Bed

This machine is capable of achieving a maximum feed rate of 23 [m/min] with a positioning accuracy of 5 [microns] on its x-axis.

The method presented in this chapter has been used to model this test-bed (refer to Figure 3.3). The ballscrew is modeled as FE beam while the nut is modeled as a 6x6 inertial matrix. The rotor is modeled as a single rotary inertia about the axis of rotation because its vibrations in the other directions are considered to be irrelevant due to the fact that the kind of coupling used does not permit the transmission of these vibrations to the rest of the system. The test-bed's jaw-type coupling is modeled as a torsional spring with spring constant k_T , together with rotary inertia J_1 and J_2 representing the inertia of the jaws. Two bearings are used to support the ballscrew – an angular-contact bearing at the end proximal to the motor and a deep-groove ball bearing at the other end. The angular-contact bearing (bearing 1) is modeled as with spring constants k_{B1ax} in the z, and k_{B1rad} in the x and y directions. The deep-groove ball bearing (bearing 2), on the other hand, is modeled with a spring constant k_{B2rad} in the x and y-directions.

The test-bed uses a box way to guide the table. Even though the box way has significant compliance, because of insufficient information from the manufacturers and the difficulty of measuring its stiffness, it is assumed to be perfectly rigid. For this reason, the table is assumed to move only in the feed (z) direction, and so is modeled as a single mass, m_{table} .

For the screw-nut interface, the rigid-ballscrew method is employed. This is because, due to insufficient information about the interface, a lot of approximations have been made. For instance, since the distribution of the balls in the interface is unknown, they have been assumed to be uniformly distributed within the entire interface. With such assumptions, the degree of modeling accuracy provided by the shape-function method is unnecessary. In fact, the shape-function method does not work as well as the rigid-ballscrew method in this situation. Furthermore, since a single nut is used in the set-up, the rigid-ballscrew method is a good enough approximation.

The values of all the model parameters are summarized in Table 3.1. Due to a lack of information from the manufacturers of the test-bed because of proprietary reasons, most of the parameters have either been measured or estimated (see Appendix B).

Ballscrew			
Total Length = 921 [mm]; $p = 10$ [mm]; $N_{Elm} = 47$; $d_r = 40$ [mm]			
Nut			
$m_{nut} = 1.49$ [kg]; $I_{xx,nut} = I_{yy,nut} = 2.56 \times 10^{-3}$ [kgm ²]; $I_{zz,nut} = 1.31 \times 10^{-3}$ [kgm ²]			
Rotor and Table			
$I_{zz,rotor} = 5.98 \times 10^{-3}$ [kgm ²]; $m_{table} = 250$ [kg]			
Coupling			
$k_T = 3.94 \times 10^3$ [Nm/rad]; $J_1 = 3.09 \times 10^{-4}$ [kgm ²]; $J_2 = 3.06 \times 10^{-4}$ [kgm ²]			
Bearings			
$k_{B1ax} = 2.70 \times 10^8$ [N/m]; $k_{B1rad} = 1.9 \times 10^8$ [N/m]; $k_{B2rad} = 4 \times 10^7$ [N/m]			
Screw-Nut Interface (Over-size Ball Preload)			
$N_{Ball} = 100$; $k_{Ball} = 20.7$ [N/ μ m]; $\alpha = 4.55^\circ$; $\beta = 50^\circ$			

Table 3.1: Parameters for Model of Experimental Test-Bed

In order to better understand the structure of the interface stiffness matrix, the first six rows and columns of the stiffness matrix \mathbf{K}_{SN} , for the interface of the experimental test-bed are given in Eq.(3.45) in terms of k_{Ball} . This portion of the matrix is sufficient to understand its structure, since the other portions have more or less the same structure and values.

$$\mathbf{K}_{SN1-6,1-6} = \begin{bmatrix} k_{x,x} & 0 & 0 & k_{x,\theta x} & 0 & 0 \\ 0 & k_{y,y} & 0 & 0 & k_{y,\theta y} & 0 \\ 0 & 0 & k_{z,z} & k_{z,\theta z} & 0 & k_{z,\theta z} \\ k_{\theta x,x} & 0 & k_{\theta x,z} & k_{\theta x,\theta x} & 0 & k_{\theta x,\theta z} \\ 0 & k_{\theta y,y} & 0 & 0 & k_{\theta y,\theta y} & 0 \\ 0 & 0 & k_{\theta z,z} & k_{\theta z,\theta z} & 0 & k_{\theta z,\theta z} \end{bmatrix}$$

Direct Terms:

$$\begin{aligned} k_{x,x} = k_{y,y} = 58.9k_{Ball}; \quad k_{z,z} = 82.1k_{Ball}; \quad k_{\theta x,\theta x} = 0.0657k_{Ball}; \\ k_{\theta y,\theta y} = 0.0653k_{Ball}; \quad k_{\theta z,\theta z} = 0.000208k_{Ball}; \end{aligned} \quad (3.45)$$

Cross-Coupling Terms:

$$\begin{aligned} k_{\theta x,x} = k_{x,\theta x} = 0.0188k_{Ball}; \quad k_{\theta y,y} = k_{y,\theta y} = 0.111k_{Ball}; \\ k_{\theta x,z} = k_{z,\theta x} = -0.0104k_{Ball}; \quad k_{\theta x,\theta z} = k_{\theta z,\theta x} = 0.0000165k_{Ball}; \\ k_{\theta z,z} = k_{z,\theta z} = -0.130k_{Ball} \end{aligned}$$

From the equation, it can be deduced that apart from the direct stiffness (diagonal terms) in each of the six directions, cross-coupling (off-diagonal) terms also exist, which couple radial and axial displacements to various rotations. Particularly, the coupling between the axial DOF and torsional DOF can be seen through the $k_{z,\theta z}$ and $k_{\theta z,z}$ terms. This coupling enables the rotary motion and vibrations of the ballscrew to be transmitted to linear motion and vibrations of the nut along the axis of the ballscrew. Most researchers ([4,42,47,51]) have also come up with this coupling in one form or the other in their screw-nut interface stiffness matrix formulations.

However, the cross-coupling terms between the axial, torsional and bending DOF ($k_{\theta x,x}$, $k_{\theta y,y}$, $k_{\theta x,z}$, $k_{\theta x,\theta z}$), have not been derived or used by these researchers. In fact, most of them have totally ignored the effects of bending, with exception of [51], who have used a screw-nut interface stiffness matrix of the form shown in Eq.(3.46), which includes all the direct terms, and only the cross-coupling terms between the axial and torsional DOF.

$$\mathbf{K}_{1-6,1-6} = \begin{bmatrix} k_{x,x} & 0 & 0 & 0 & 0 & 0 \\ 0 & k_{y,y} & 0 & 0 & 0 & 0 \\ 0 & 0 & k_{z,z} & 0 & 0 & k_{z,\theta z} \\ 0 & 0 & 0 & k_{\theta x,\theta x} & 0 & 0 \\ 0 & 0 & 0 & 0 & k_{\theta y,\theta y} & 0 \\ 0 & 0 & k_{\theta z,z} & 0 & 0 & k_{\theta z,\theta z} \end{bmatrix} \quad (3.46)$$

In order to ascertain the effect of the cross-coupling terms between the axial, torsional and bending DOF derived in this thesis, the screw-nut interface stiffness matrix of Eq.(3.45) has been compared to that of Eq.(3.46) in a study presented in Appendix C. This simulation-based study shows that the cross-coupling terms are needed to capture the influence of some of the ballscrew bending deformation modes on the table position, and also the interaction between axial/torsional and bending deformations of the ballscrew.

3.5.2 Step-by-Step Verification of Model

3.5.2.1 Free-Free Ballscrew

The first step in the verification process is to validate the Timoshenko FE beam model of the ballscrew. The figures below show FRFs of the ballscrew in its free-free condition measured in the axial, torsional and radial directions.

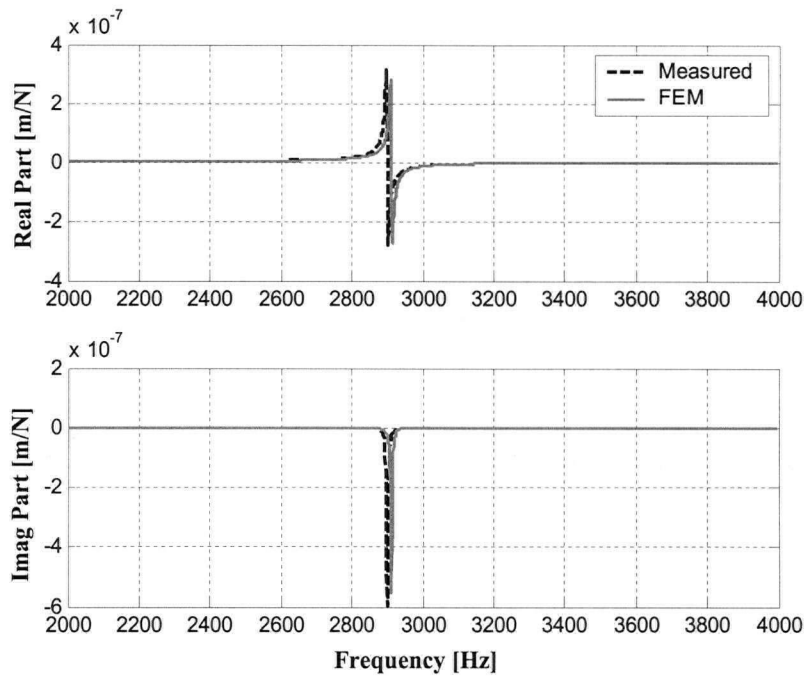


Figure 3.20: Axial FRF of Free-Free Ballscrew

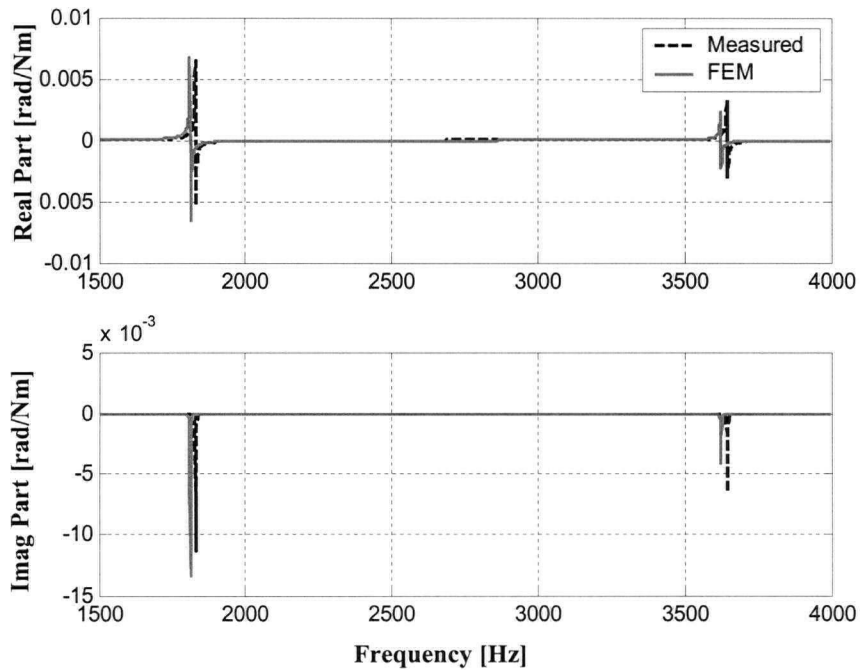


Figure 3.21: Torsional FRF of Free-Free Ballscrew

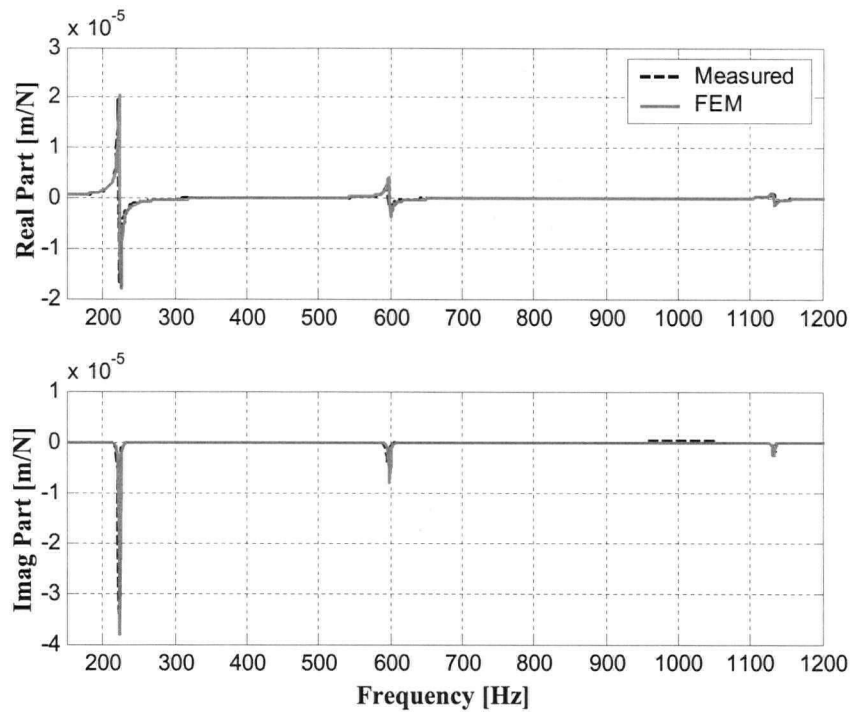


Figure 3.22: Radial FRF of Free-Free Ballscrew

The figures show a good match between experimental measurements and FEM simulation in the three directions. Hence, the FE beam approximation of the ballscrew is good enough.

3.5.2.2 Ballscrew and Nut

In order to verify the interface stiffness and nut models, the nut is attached to the free-free ballscrew and FRF measurements are made in the same three directions, as shown in the figures below.

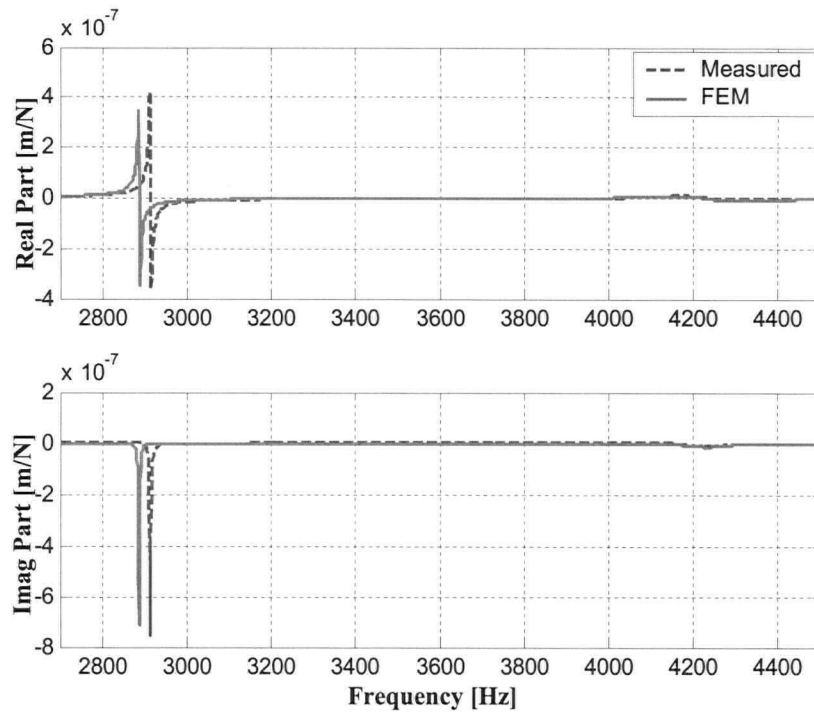


Figure 3.23: Axial FRF for Free-Free Ballscrew-Nut Assembly

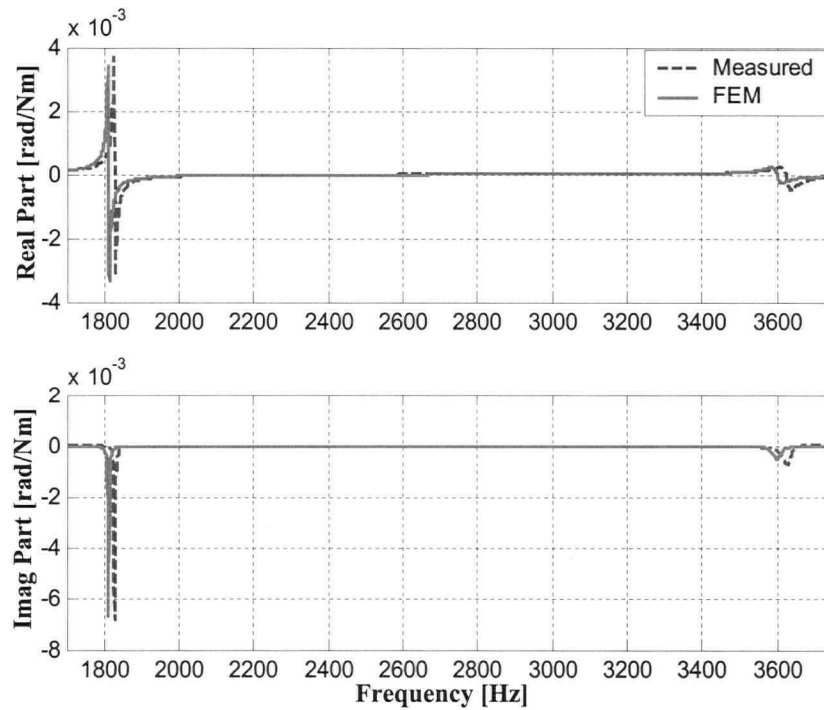


Figure 3.24: Torsional FRF for Free-Free Ballscrew-Nut Assembly

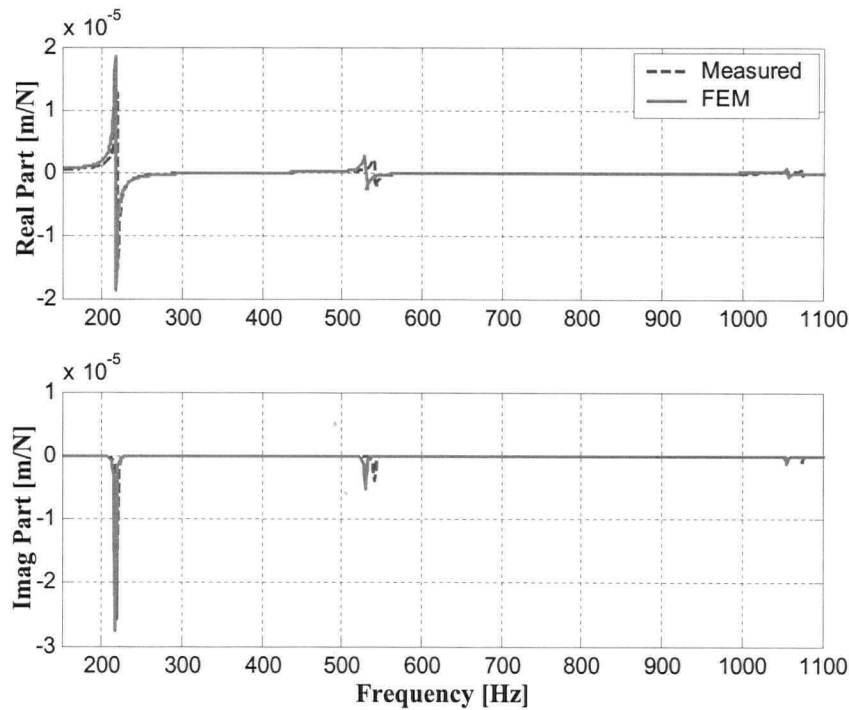


Figure 3.25: Radial FRF for Free-Free Ballscrew-Nut Assembly

As seen from the figures, FE Simulations based on the nut and interface models presented above give a good agreement with the experimental measurements in the three directions.

Since, often times, it is of interest to know the dynamic response measured from a torque applied to the ballscrew end (by the motor) to the displacement measured at the table (which is coupled to the nut), Figure 3.26 shows the FRF measured from a torque at the ballscrew end to the displacement at the nut. As seen from the figure, the axial and torsional modes (shown above) are dominant, for this particular ballscrew, while the radial modes are not. The second mode in the figure shows a mismatch between the experimental measurement and the FE simulation due to time delays stemming from the backlash in the nut.

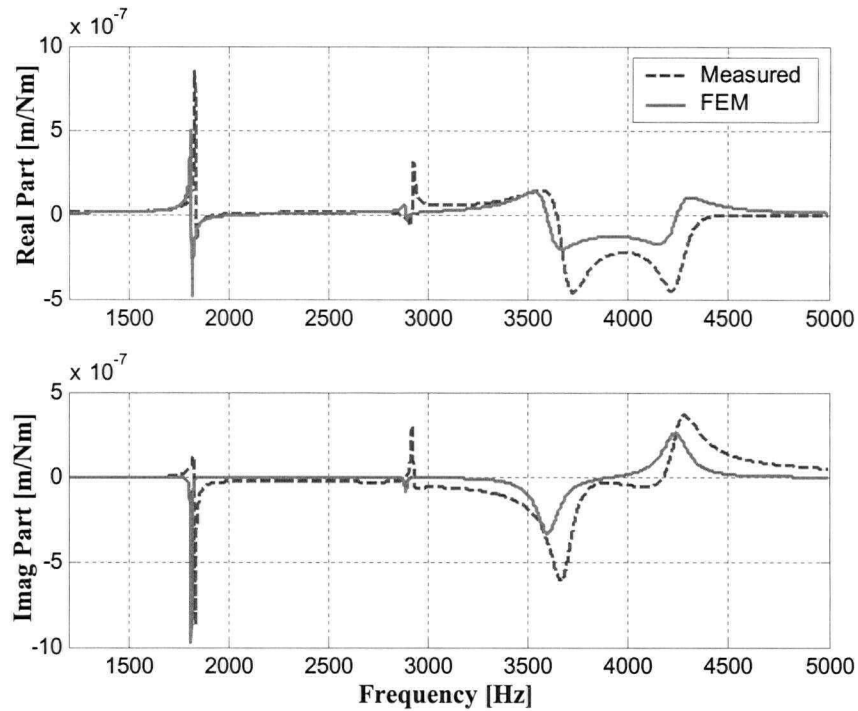


Figure 3.26: FRF Between Torque at Screw End and Axial Displacement at Nut

It is also of interest to know if the model is able to capture the changes in dynamics as the nut travels along the ballscrew. The figures below show a comparison between FRFs measured and simulated at three different nut positions (shown on the figure) on the ballscrew shaft for the first axial and torsional mode of the assembly. The radial direction is not shown because there are no significant changes in that direction.

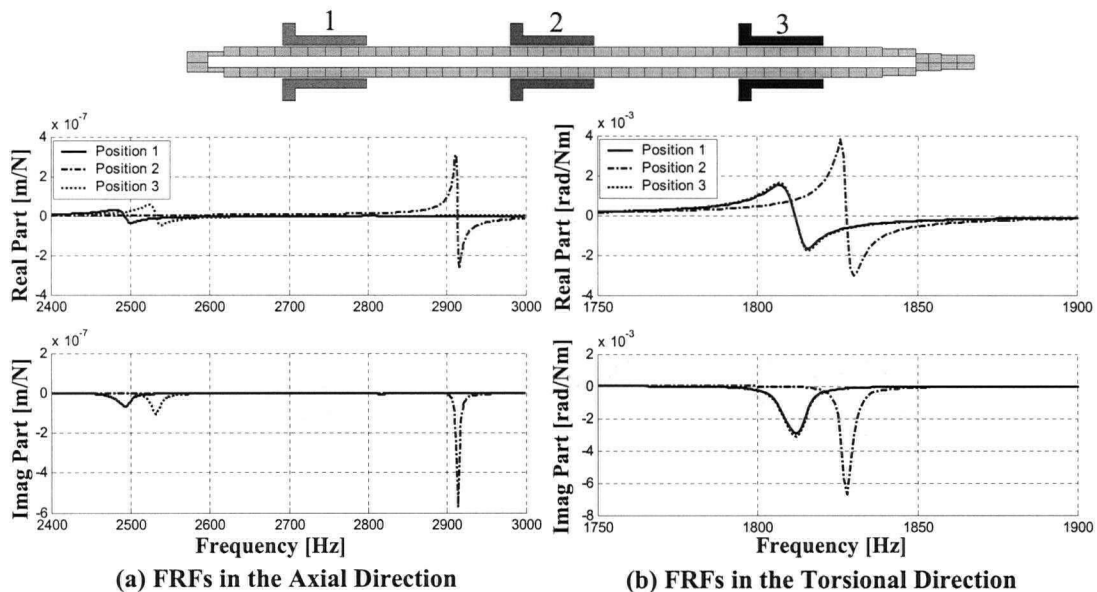


Figure 3.27: Position-Dependent Dynamics (Measured)

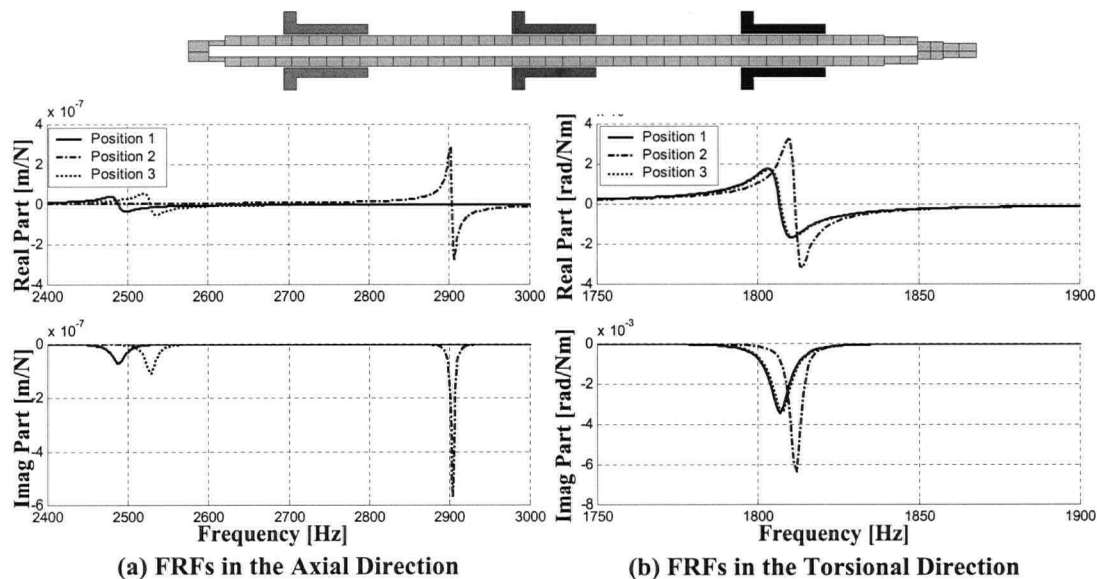


Figure 3.28: Position-Dependent Dynamics (Simulated)

As indicated by the figures, the interface model presented above is able to capture the changing dynamics of the system as the nut moves from position to position along the ballscrew.

SOURCE	Natural Frequency of First Axial Mode [Hz]		
	Position 1	Position 2	Position 3
Measurement	2493	2914	2532
Simulation	2489	2904	2528

Table 3.2: Position-Dependent Variation of First Axial Natural Frequency

SOURCE	Natural Frequency of First Torsional Mode [Hz]		
	Position 1	Position 2	Position 3
Measurement	1812	1828	1812
Simulation	1807	1812	1807

Table 3.3: Position-Dependent Variation of First Torsional Natural Frequency

Table 3.2 shows the variation of the system's axial natural frequencies from one position to the other. As seen, the measurements show a change in axial natural frequencies from 2493 to 2914 [Hz] (a difference of 421 [Hz]) as the nut moves from position 1 to 2, while the simulations capture this variation as a change from 2489 to 2904 [Hz] (a difference of 415 [Hz]). At position 3, the natural frequency drops to 2532 [Hz] in the measured FRF, and to 2528 [Hz] in the simulated one. Table 3.3 indicates that the variations in torsional natural frequencies are much smaller; which is due to the weaker stiffness coupling provided by the screw-nut interface in that direction.

As will be shown in the subsequent chapters, this position-dependent variation in structural dynamics plays an important role in controller design and performance simulation based on the feed drive model, hence the need to model the ballscrew using FEM and to elaborately derive a screw-nut interface stiffness matrix in order to capture it as precisely as possible.

3.5.2.3 Full System without Table, Coupling and Rotor

As a penultimate step, the entire system is assembled onto the frame with the exception of the table, coupling and rotor. The reason for this is to see how the model behaves before

the table, which introduces a lot of non-linearities like friction and increased backlash, is mounted. Furthermore, the motor is not used for providing excitations, also to eliminate the effects of the dynamics coming from the electrical components of the drive which have not been included into this model. The figures below show a comparison between the FE simulations and measurements on the test-bed.

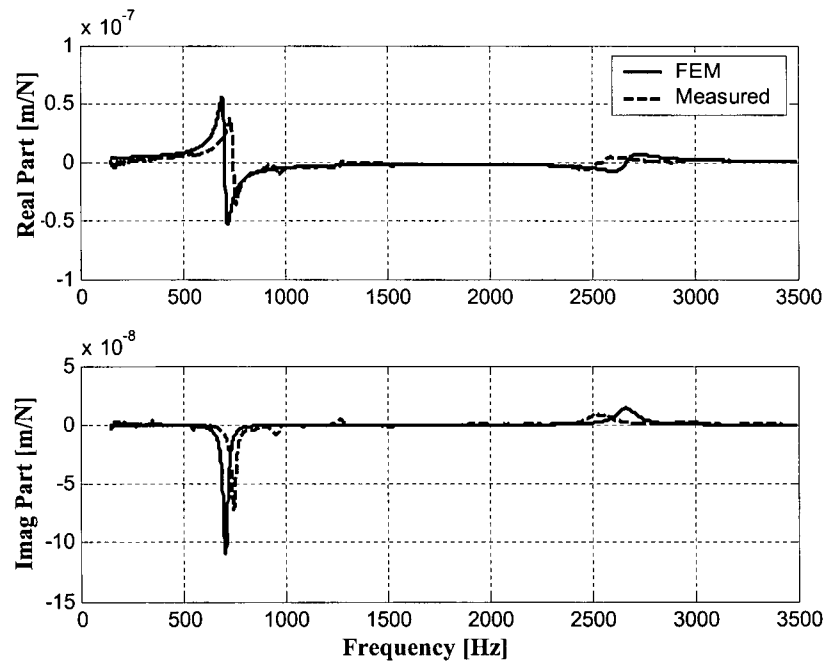


Figure 3.29: Axial FRF of Full System Except Table, Coupling and Rotor

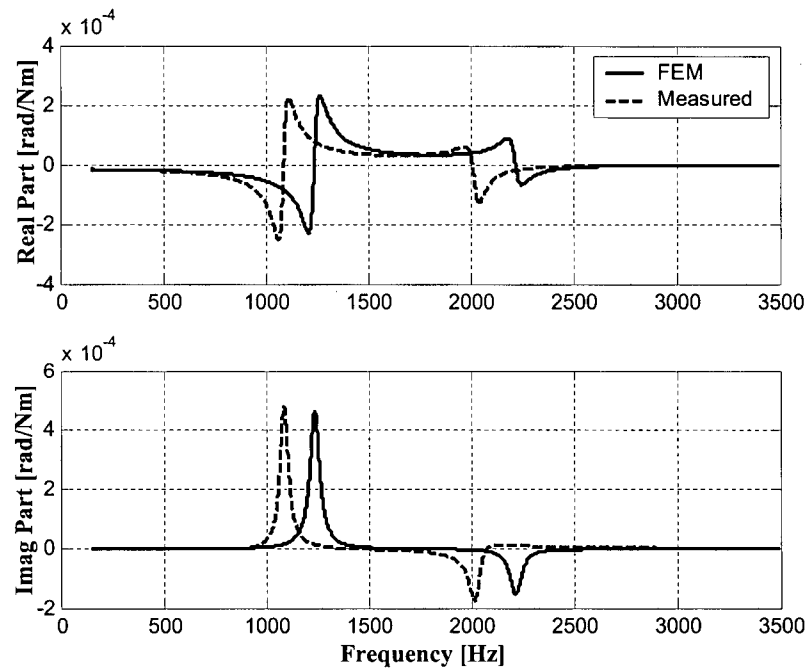


Figure 3.30: Torsional FRF of Full System Except Table, Coupling and Rotor

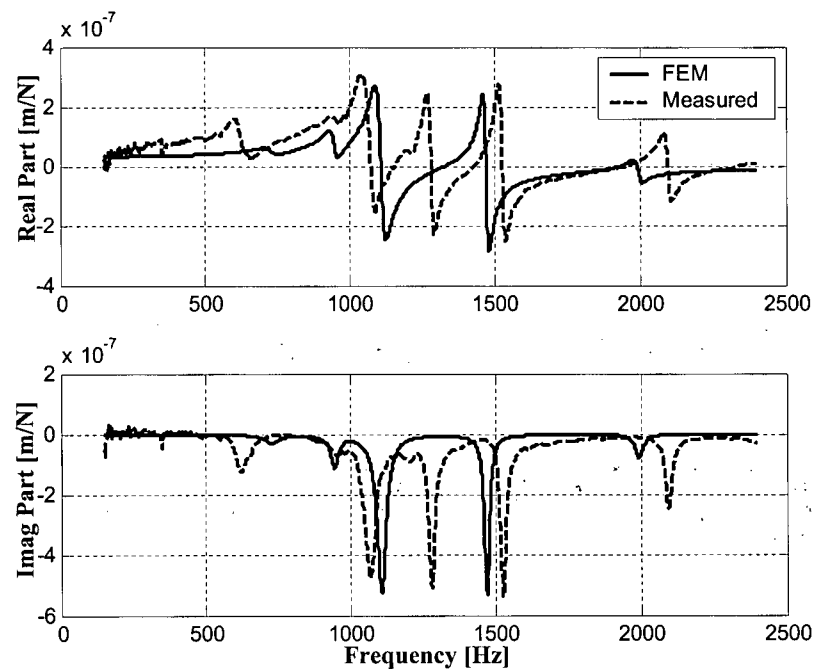


Figure 3.31: Radial FRF of Full System Except Table, Coupling and Rotor

As seen from the figures, even though the model is still able to capture the dynamics in the three directions, the match between measurement and simulations has declined

significantly. The axial modes show a slight shift in frequency, and also a bit of mismatch in amplitude. This is probably due to the approximations made regarding the axial stiffness of the angular-contact ball bearing (see Appendix B).

The torsional modes match quite well in amplitude, but show a constant shift in frequencies. A possible reason for this is the effect of the inertia of the bearing rings and balls which are not included in the bearing model.

As for the radial modes (Figure 3.31), the model seems to be good in predicting the second, third and fifth modes of the system. However, the first and last modes show a poor match, while the fourth mode is totally missed out. Definitely, the approximations made in the radial stiffness of both bearings plays a role in affecting the accuracy of the model. Furthermore, the angular-contact bearing has a housing consisting of a huge block within which the bearing sits. This block is connected to the machine's frame using fasteners. With more information about the housing, particularly about the spring stiffness of the fasteners, this housing should have been more realistically modeled as a lumped mass attached to the frame by springs. However, here, this compliance has been neglected, and the housing assumed to be rigidly connected to the frame. This is probably the reason for the mode missing from the model.

3.5.2.4 Full System

Finally, in order to test the full model, the motor is connected to the rest of the system through the coupling, and the table is attached to the nut. As mentioned earlier, due to the lack of information about the guideways, they are assumed to be perfectly rigid.

All of the FRF measurements above have been made using an impulse hammer-accelerometer set. However, for the full model, this technique cannot provide sufficient excitation for the system, therefore a stepped sine wave approach is used. Sine waves are applied to the motor as control signals through the electrical components of the drive, while angular position measurements are taken from an angular encoder mounted on the end of the ballscrew distal from the motor. In addition, linear position measurements are taken from a linear encoder mounted on the table. The dynamics of the electrical components between control signal and the motor torque (see Figure 3.1) are modeled as a constant gain, due to

the fact that the amplifiers are set to the current-controlled mode. For more information about these measurements, see [13].

The figures below show the comparison between the full FE model simulations and experimental measurements.

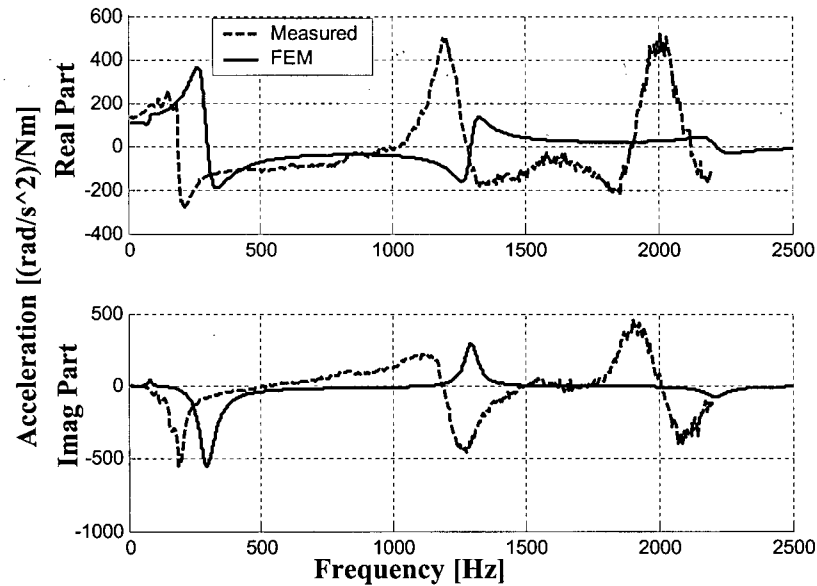


Figure 3.32: FRF from Excitation at Motor to Angular Acceleration at Ballscrew End

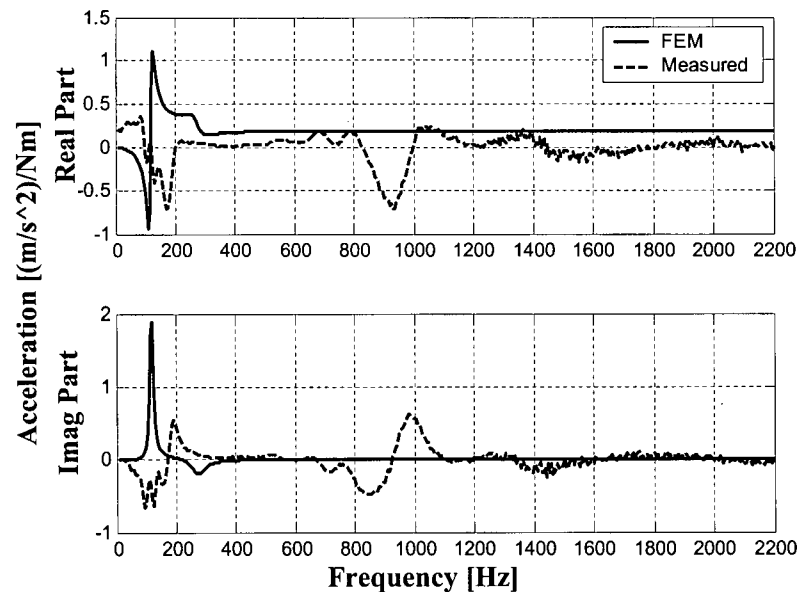


Figure 3.33: FRF from Excitation at Motor to Linear Acceleration at Table

As observed from the figures, there are significant deviations between the prediction of the FE model and the measured responses. The torsional modes show a reasonable comparison, particularly for the first mode which comes from the coupling. Even though the other modes show a reasonable match in frequency, the measured results show huge reversals and amplitude deviations. These are partly as a result of the non-linear friction and backlash which have been greatly amplified by the addition of the table. Furthermore, the dynamics of the electronic components definitely add a time delay to the response due to the influence of the D/A converters.

In the second FRF from motor torque to linear accelerations at the table, the model again gives a somewhat reasonable prediction at the low frequency modes. However, the mode at about 900 [Hz] is not captured by the model. This is probably arising from the influence of the guideway compliance which has not been modeled. The FE model indicates radial modes of the ballscrew at about the same frequency. However, these cannot be transmitted to the table when the guideway is assumed to be perfectly rigid. Another significant factor influencing the results is the compliance between the table and nut via fasteners, which has not been considered due to insufficient information.

3.6 Summary

In this chapter, a hybrid finite element modeling technique combining FE structures with lumped-parameter has been presented for ballscrew drives. In particular, the screw-nut interface, which plays a key role in the dynamics of ballscrew drives, has been looked into more closely. As an improvement to the models already in existence for this interface, two methods – the rigid-ballscrew method and the shape function method – have been developed.

Judging from the foregoing, it can be said that the modeling technique presented here is potentially good enough for capturing linear dynamics within the frequency range for control engineering purposes, given that sufficient information is provided about the system parameters. The discrepancies that show up in the full model are to be expected because the experimental test-bed used here does not reflect the class of machine tool feed drives to which the modeling technique presented here is applicable. High speed machine tool ballscrew drives which require this type of modeling are often built such that non-linear effects such as friction and backlash are highly minimized. Consequently, for such ballscrew

drives, a linear model is sufficient to capture the necessary dynamics needed for controller design, which is the topic of Chapter Four. Furthermore, the remaining non-linearities in the system, which cannot be captured by the linear model, can be included in a time-domain simulation model in order to be able to investigate their effects on the feed drive and controller performance. This is the topic of Chapter Five.

Chapter 4

Model Analysis and Controller Design

4.1 Overview

In this chapter, the model for the experimental test-bed presented in the previous chapter is analyzed to obtain the information needed for controller design. Using this information, two types of high-bandwidth controllers are designed for the feed drive system. The first controller is designed following the traditional technique which is based on only the rigid-body dynamics of the drive. However, it is shown that modifications have to be made in order to successfully implement such a controller on a feed drive system which has significant flexibilities. Furthermore, a second controller is presented, in which the high-order dynamics of the feed drive are considered in the controller design process. The performance characteristics of these two designs are analyzed using frequency and time-domain methods, mainly with an aim of underlining the necessity of the modeling technique presented in Chapter Three.

A pre-controller-design analysis of the open-loop dynamics of the feed drive system is presented in Section 4.2. This is followed by the design of the first controller based on rigid-body dynamics in Section 4.3. Section 4.4 shows the short-comings of this design when implemented on a feed drive with significant flexibilities, and proffers two commonly used solutions to the problem. In Section 4.5, the second controller is presented, and then some concluding remarks are given in the last section.

4.2 Extraction of Open Loop Transfer Function of Feed Drive Model

There are many ways of representing the modeled dynamics of a system for which a controller is to be designed. Two of the most common ones are the transfer function (TF) and state-space (SS) methods. In some cases, choice between the two depends on the kind of controller design and analysis that is intended, while in other cases, either representation works as well as the other.

In this chapter, the transfer function method is preferred for controller design and analysis because it gives a compact and rather intuitive representation of the feed drive dynamics. In addition, it provides simpler and more effective formulations for the controllers considered here.

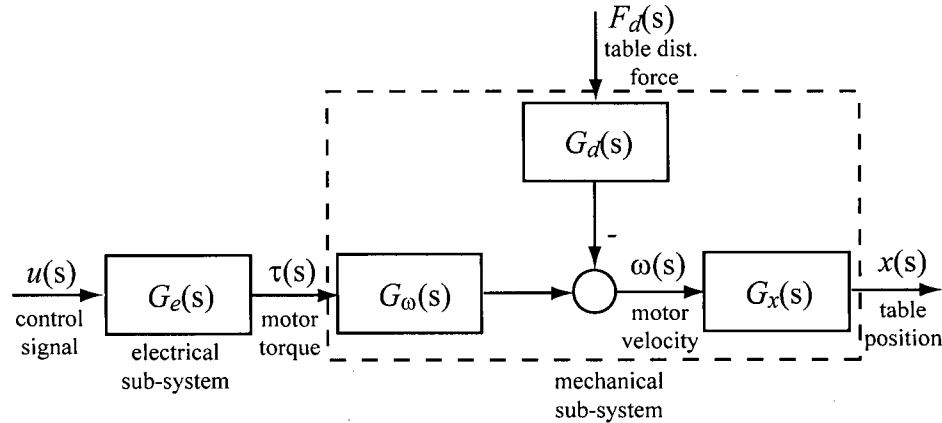


Figure 4.1: Open-Loop Dynamics of Feed Drive Axis

Figure 4.1 shows a block diagram of the open-loop (OL) dynamics for the feed drive axis of the experimental set-up in the previous chapter (hereinafter described as the *set-up*). $G_e(s)$ is the transfer function of the electrical system (with the exception of the D/A converter). It represents the dynamics between the analog control signal, $u(s)$ and the actuation torque applied to the motor, $\tau(s)$. For this set-up, this dynamics is assumed to be much faster than that of the mechanical sub-system. Therefore it is approximated as,

$$G_e(s) = K_a K_t \quad (4.1)$$

where $K_a = 6.4898$ [A/V] is the current amplifier gain, and $K_t = 0.4769$ [Nm/A] is the motor's torque constant.

The mechanical system can be considered to consist of three transfer functions. The first, $G_\omega(s)$, represents the dynamics between the motor torque and the motor's angular velocity, $\omega(s)$, while $G_x(s)$, the second transfer function, describes the dynamics between $\omega(s)$ and $x(s)$, the position of the table. The third transfer function, $G_d(s)$, on the other hand, represents the effect any kind of disturbance force applied to the table (cutting forces, friction forces, etc), $F_d(s)$ has on $\omega(s)$. These three transfer functions can either be used to express the rigid-body

dynamics of the drive, or they can be used to describe a combination of both the rigid-body and structural dynamics of the drive. These two options are explained in the sections below.

4.2.1 Rigid-Body Dynamics

The transfer functions for the rigid-body dynamics of the feed drive are given by,

$$G_{\omega}^r(s) = \frac{1}{Js + B}; \quad G_x^r(s) = \frac{r_g}{s}; \quad G_d^r(s) = \frac{r_g}{Js + B} \quad (4.2)$$

Here, $J=8.55 \times 10^{-3}$ [kgm²] is the total inertia of the feed drive reflected at the motor shaft. It can easily be obtained from the modal mass m_q of the rigid body mode of the drive (see Appendix A). $B=0.0321$ [kgm²/s] is the equivalent viscous damping of the drive system, also reflected at the motor shaft. Its value is obtained experimentally. $r_g=1.59 \times 10^{-3}$ [m/rad] is the gear reduction ratio of the drive's ballscrew, which represents the amount of linear motion obtained at the table per unit rotation of the motor shaft. The superscript, r on each of the transfer functions in Eq.(4.2) indicates that they represent only rigid-body dynamics.

4.2.2 Inclusion of Structural Dynamics

Theoretically, the feed drive system, just like any structural system, has infinite degrees-of-freedom (DOF), meaning that it has an infinite number of normal (vibration) modes besides its rigid-body modes. When the finite element method is used to model the system, the number of normal modes is reduced to a finite value given by the number of DOF considered in the model. However, in controller design, it is often unnecessary to consider vibration modes at frequencies that are far higher than the desired bandwidth of the drive. Furthermore, some vibration modes, even though within the frequency region of interest, do not affect the dynamics between the controlled input and the measured output because of their mode shapes, therefore they do not need to be considered for controller design.

In order to find out which of the normal modes should be considered, it is helpful to inspect the frequency response functions (FRF) of the model between the controlled input(s) and measured output(s), within the frequency range of interest.

For the particular feed drive considered here, it is desired to achieve a closed-loop (CL) bandwidth of 50 to 100 [Hz], therefore a frequency range of up to 300 [Hz] is examined.

Figure 4.2 shows the magnitudes of the FRFs between the two inputs $\tau(s)$ and $F_d(s)$, and two outputs $\omega(s)$ and $x(s)$ of the set-up within this frequency range (0 – 300 [Hz]).

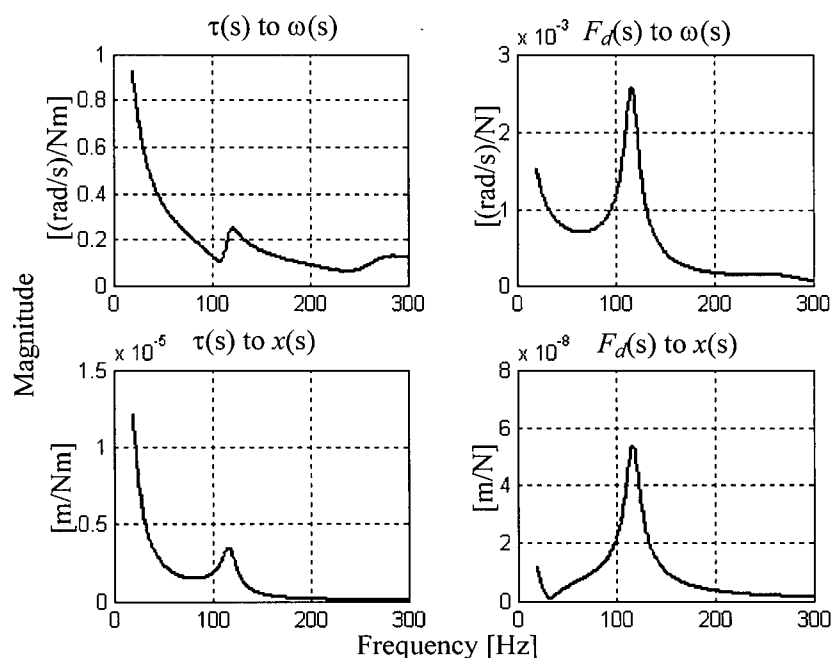


Figure 4.2: Magnitudes of the FRFs between Feed Drive Inputs and Outputs

As seen from the figure, there are two normal modes of interest within the considered frequency range. There is the mode at about 120 [Hz], which is dominant, and then another mode at about 270 [Hz] which is relatively weaker. As will be explained later, the 120-Hz mode corresponds to the axial deformation of the ballscrew between the fixed thrust bearing and the nut, while the 270-Hz mode is mainly due to the torsional deformation of the coupling between the motor shaft and ballscrew.

It must be mentioned here that the plots shown in Figure 4.2 reflect the FRFs generated with the table positioned at the centre of its travel range. However, because of the position-dependent structural dynamics variations explained in Section 3.5.2.2, it is also necessary to examine the same FRFs generated with the table positioned at the extremities of its travel range to check if any additional modes show up. For the feed drive considered here, this analysis has been conducted, and it reveals that the same two modes are present, with only slight changes in their natural frequencies. The effects of this natural frequency variation will be looked into later.

Generally, the transfer function $G_p(s)$ between an input force and output position for a linear system, including its structural dynamics (normal modes) can be expressed as,

$$G_p(s) = G_p^r(s) + \sum_{k=1}^{N_{mode}} \frac{(R_p)_k}{s^2 + 2\zeta_k(\omega_n)_k s + (\omega_n)_k^2} \quad (4.3)$$

where ζ_k is and $(\omega_n)_k$ are respectively the damping ratio and natural frequency of the k^{th} normal mode and N_{mode} is the number of normal modes considered, while $G_p^r(s)$ is the rigid-body transfer function for the system, similar to those defined in Eq.(4.2). $(R_p)_k$ is the transfer function's residue for the k^{th} mode given by,

$$(R_p)_k = \frac{\mathbf{P}_{k,i} \mathbf{P}_{k,j}}{(m_q)_k} \quad (4.4)$$

$\mathbf{P}_{k,m}$ and $\mathbf{P}_{k,n}$ are respectively the i^{th} and j^{th} elements of the k^{th} normal mode shape vector. i represents the input node, while j represents the output node. $(m_q)_k$ is the modal mass for the k^{th} mode.

Based on this information, the transfer function $G_\omega(s)$, considering the rigid-body dynamics and the two normal modes mentioned above, is expressed as,

$$G_\omega(s) = G_\omega^r(s) + \frac{R_{\omega 1} s}{s^2 + 2\zeta_1 \omega_{n1} s + \omega_{n1}^2} + \frac{R_{\omega 2} s}{s^2 + 2\zeta_2 \omega_{n2} s + \omega_{n2}^2} \quad (4.5)$$

where the subscripts 1 and 2 represent the first and second normal modes. The extra s term appearing in the numerator is as a result of the derivative operation needed to convert a transfer function between an input force and output position to one between an input force and an output velocity.

Similarly, $G_d(s)$ is given by,

$$G_d(s) = G_d^r(s) + \frac{R_{d1} s}{s^2 + 2\zeta_1 \omega_{n1} s + \omega_{n1}^2} + \frac{R_{d2} s}{s^2 + 2\zeta_2 \omega_{n2} s + \omega_{n2}^2} \quad (4.6)$$

In order to calculate $G_x(s)$, an intermediary transfer function $G_m(s)$ must be defined between the motor torque, $\tau(s)$ and the table position, $x(s)$. This transfer function has the form,

$$G_m(s) = G_m^r(s) + \frac{R_{m1}}{s^2 + 2\zeta_1\omega_{n1}s + \omega_{n1}^2} + \frac{R_{m2}}{s^2 + 2\zeta_2\omega_{n2}s + \omega_{n2}^2} \quad (4.7)$$

$G_m^r(s)$ is the rigid-body mode for the transfer function given by,

$$G_m^r(s) = G_\omega^r(s) \cdot G_x^r(s) = \frac{r_g}{Js^2 + Bs} \quad (4.8)$$

Then the transfer function $G_x(s)$ can be obtained as,

$$G_x(s) = \frac{G_m(s)}{G_\omega(s)} \quad (4.9)$$

The numerical values for the modal parameters and residues appearing in Eq.(4.5) to Eq.(4.7) for three positions of the table are summarized in Table 4.1. The positions examined are the extreme left position (L-Position), centre position (C-Position) and extreme right position (R-Position) of the table within its travel range.

PARAMETER	VALUE		
	L-Position	C-Position	R-Position
f_{n1} [Hz]	109.51	117.69	133.82
ζ_1 [%]	6	6	6
$R_{\omega 1}$ [rad ² /(Nms ²)]	13.75	14.52	16.25
R_{m1} [rad ² /(Ns ²)]	-2.22x10 ⁻¹	-2.27x10 ⁻¹	-2.38x10 ⁻¹
R_{d1} [rad ² /(Ns ²)]	-2.22x10 ⁻¹	-2.27x10 ⁻¹	-2.38x10 ⁻¹
f_{n2} [Hz]	269.62	270.92	273.62
ζ_2 [%]	10	10	10
$R_{\omega 2}$ [rad ² /(Nms ²)]	28.06	27.29	25.56
R_{m2} [rad ² /(Ns ²)]	3.53x10 ⁻²	4.06x10 ⁻²	5.19x10 ⁻²
R_{d2} [rad ² /(Ns ²)]	3.53x10 ⁻²	4.06x10 ⁻²	5.19x10 ⁻²

Table 4.1: Parameters for Mechanical Sub-System Transfer Functions

The natural frequencies ω_n in [rad/s] used in Eq.(4.5) to Eq.(4.7) can be obtained from the f_n [Hz] values provided in Table 4.1 by simply multiplying them by a factor of 2π .

4.3 High-Bandwidth Controller Design Based on Rigid-Body Dynamics

Following the customary practice in feed drive controller design, controllers are often designed based on the rigid-body dynamics of the drive. One of the most common types of designs used in machine tool feed drives is the P-PI control scheme. As shown in Figure 4.3, this type of design consists of two cascaded control loops – a velocity loop with an analog Proportional-Integral (PI) controller, around which is wrapped a position loop consisting of a digital Proportional (P) controller. A Zero-Order Hold (ZOH) is placed between the digital P-Controller and the analog PI-Controller as a D/A converter.

The rationale for this cascaded control scheme is that the PI-Controller is used to provide more damping for the close-loop system, together with an integral action which helps to eliminate steady-state errors that could arise from constant disturbance forces. The digital P-controller is then used as a tuning knob to adjust the overall gain of the closed-loop system.

In this set-up, the analog angular velocity signals are measured using a tachometer with a conversion gain $H_g=0.0668$ [V/(rad/s)], attached to the motor shaft, while the table position is measured as digital signals using a linear encoder mounted on the table.

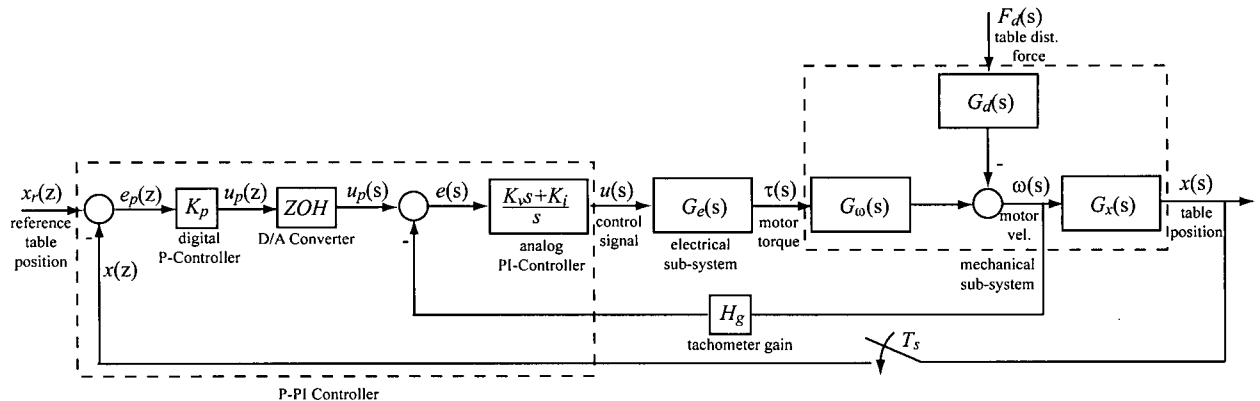


Figure 4.3: P-PI Control Scheme

In this design task, the objective is to appropriately select the controller gains, K_i , K_v and K_p , in order to achieve a high control bandwidth, while maintaining good reference tracking with adequate disturbance and noise rejection.

Since only the rigid-body dynamics is considered in this design, the transfer functions $G_\omega(s)$, $G_x(s)$ and $G_d(s)$ in Figure 4.3 are replaced with $G_\omega^r(s)$, $G_x^r(s)$ and $G_d^r(s)$, respectively.

The design is carried out in two stages. First the analog PI controller for the velocity loop is designed, and then the digital P-Controller is designed for the position loop. These two steps are explained in more detail below.

4.3.1 Design of the Analog PI-Controller

The closed-loop transfer function of the velocity loop is expressed as,

$$G_v(s) = \frac{\frac{K_a K_t K_i H_g}{J} \left(\frac{1}{H_g} + \frac{K_v}{K_i H_g} s \right)}{s^2 + \left(\frac{B + K_a K_t K_v H_g}{J} \right) s + \left(\frac{K_a K_t K_i H_g}{J} \right)} \quad (4.10)$$

Since the denominator is second-order, it can be expressed in terms of ω_n and ζ , the closed loop natural frequency and damping ratio, as,

$$\text{den}(G_v(s)) = s^2 + \left(\frac{B + K_a K_t K_v H_g}{J} \right) s + \left(\frac{K_a K_t K_i H_g}{J} \right) \equiv s^2 + 2\zeta\omega_n s + \omega_n^2 \quad (4.11)$$

By comparing terms, K_i and K_v can be written in terms of ω_n and ζ as,

$$K_i = \frac{J\omega_n^2}{K_a K_t H_g}; \quad K_v = \frac{(2\zeta\omega_n J - B)}{K_a K_t H_g} \quad (4.12)$$

For this set-up, it is desired to have a critically damped denominator dynamics with a natural frequency (f_n) of 50 [Hz]. Based on these specifications, ω_n and ζ are obtained as,

$$\zeta = 0.7071; \quad \omega_n = 2\pi f_n = 314.16 \text{ [rad/s]} \quad (4.13)$$

From these values, the gains of the PI-Controller are obtained from Eq.(4.12) as,

$$K_v = 18.217 \text{ [V/V]}; \quad K_i = 4081.2 \text{ [rad/s]} \quad (4.14)$$

Figure 4.4 shows the unit step response for the closed-loop system. As seen, the system has a fast rise time of about 3 [ms] and a settling time of 16 [ms]. Even though the denominator dynamics is critically damped, the system still has an overshoot of about 16 [%], arising because of the extra dynamics added by the zero in the numerator. However, a

small overshoot in the velocity loop is usually permissible since this does not necessarily affect the feed drive's positioning accuracy.

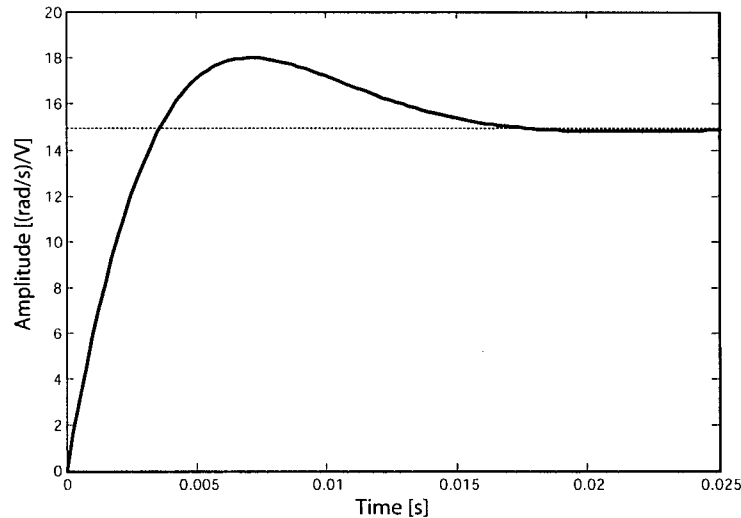


Figure 4.4: Unit Step Response of Rigid-Body-Based PI-Controlled Velocity Loop

If the open-loop (OL) transfer function is denoted as $L(s)$, the sensitivity function $S(s)$ and complementary sensitivity function $T(s)$ can be expressed as [25],

$$S(s) = \frac{1}{1+L(s)}; \quad T(s) = \frac{L(s)}{1+L(s)} \quad (4.15)$$

These two functions play a very important role in control engineering. The sensitivity function gives an indication of the susceptibility of the closed-loop system to the effect of an external disturbance. At the same time, it also provides a measure of the relative change in closed-loop dynamics with respect to any relative change in the open-loop dynamics. The complementary sensitivity function, on the other hand, influences how much measurement noise is injected back into the closed-loop response. In practice, it is desirable to keep $S(s)$ minimal in the low frequency range, so that external disturbances within the control bandwidth are effectively rejected, while $T(s)$ should be kept low at frequencies beyond the control bandwidth in order to minimize the influence of high-frequency measurement noise. However, from Eq.(4.15), it can be seen that $S(s) + T(s) = 1$. This implies a trade off between achieving effective disturbance rejection and measurement noise sensitivity – which is one of the key challenges in any controller design problem [13].

Figure 4.5 shows the magnitude Bode plots for the closed-loop, sensitivity function and complementary sensitivity function of the velocity loop.

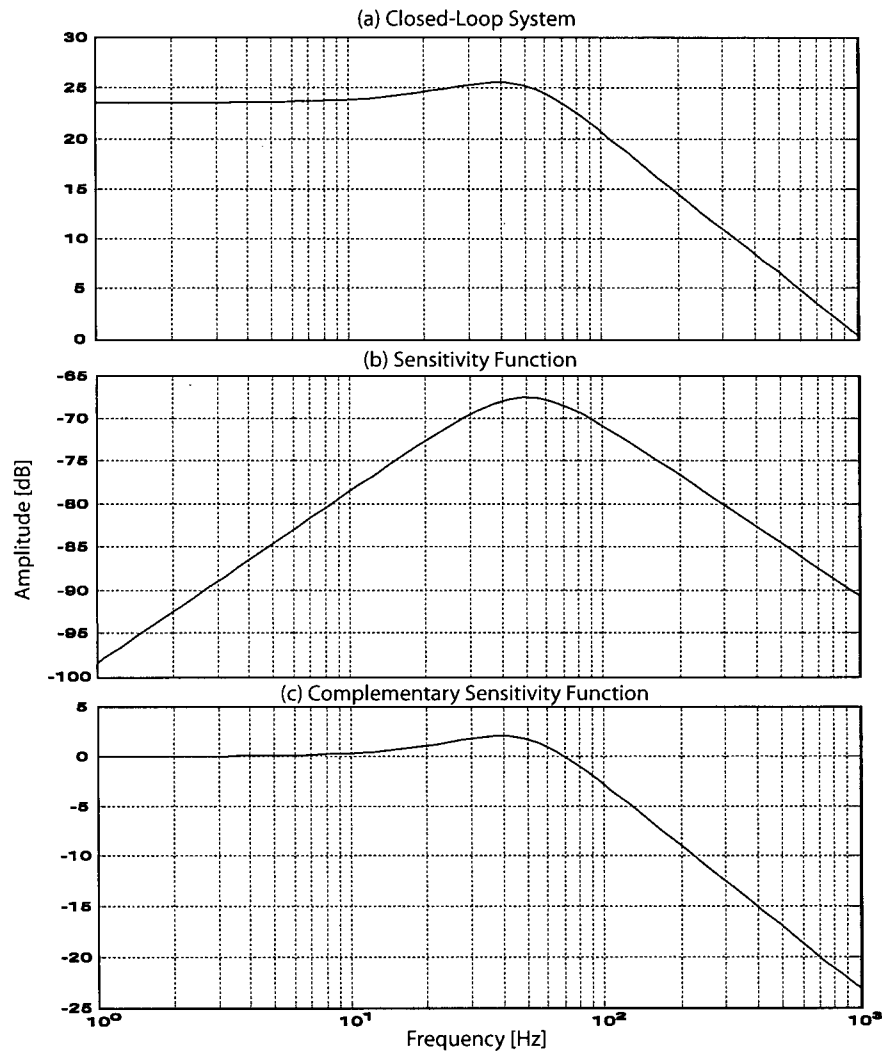


Figure 4.5: Response Functions for Rigid-Body-Based PI-Controlled Velocity Loop

From plot (a), the closed-loop bandwidth is obtained as 102 [Hz]. The sensitivity function in plot (b) shows a good rejection of low frequency disturbance, with a maximum amplitude of -67.6 [dB] occurring at 48.4 [Hz]. The high-frequency noise attenuation is also good, as shown by the complementary sensitivity function in plot (c). The maximum value of $T(s)$ is 2.02 [dB] and it occurs at 42.2 [Hz], after which it gently rolls off.

4.3.2 Design of the Digital P-Controller

Following the design of the analog PI-controller presented above, it now remains to close the position loop using a P-controller. Since the P-controller is implemented digitally, the position loop dynamics has to be transformed from continuous-time to discrete time using the z-transform. Noting that the dynamics of the ZOH is given by,

$$ZOH = \frac{1 - e^{-sT_s}}{s} \quad (4.16)$$

the discrete-time open-loop TF, $L(z)$ for the position loop can be calculated as,

$$L(z) = Z \left\{ \frac{1 - e^{-sT_s}}{s} K_p G_v(s) G_x(s) \right\} \quad (4.17)$$

where $T_s = 200$ [μ s] is the sampling period, and Z represents the z-transform operator.

K_p , being the only design parameter, is adjusted in order to maintain a stable loop, while satisfying the design requirements. Practically, the value of K_p is also limited by the saturation limits of the amplifier and actuator. As mentioned in Chapter Three, since the set-up was not designed for High-Speed Machining (HSM) purposes, its saturation limits reduce the achievable bandwidth to values much below the desired values for the purposes of HSM. However, since the controller design here is performed mainly for demonstrative purposes, and will not be implemented on the actual machine, these limits are ignored and the value of K_p is adjusted to 7000 [V/m] to achieve a closed-loop bandwidth of 58 [Hz].

Figure 4.6 shows a Bode plot of $L(z)$ with the K_p set at 7000 [V/m].

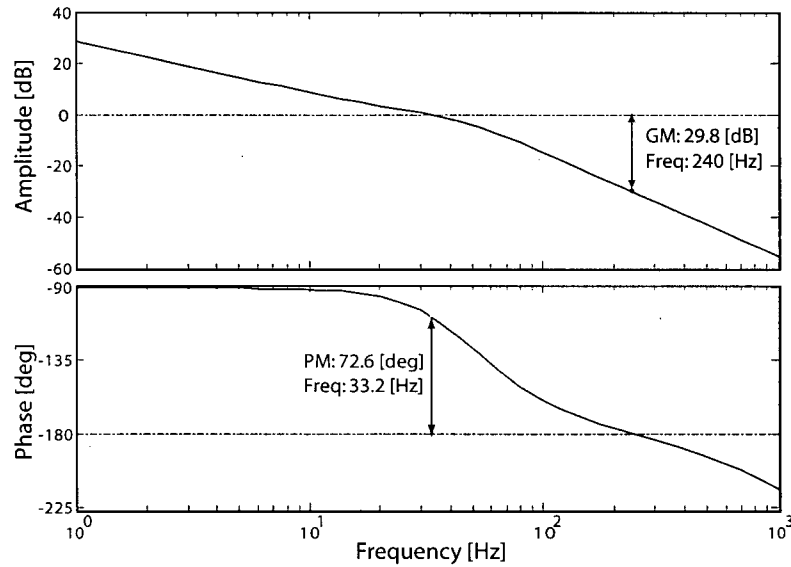


Figure 4.6: Open-Loop Bode Diagram for Position Loop of Rigid-Body-Based P-PI Controller Combined with Rigid-Body-Based Feed Drive Model

The loop is stable, with a good gain margin (GM) of 29.8 [dB] and phase margin (PM) of 72.6 [deg]. The unit step response from the reference table position $x_r(z)$ to the actual table position $x(s)$ in Figure 4.7 shows a fast rise time of 7 [ms] and a settling time of 26 [ms]. Even though the response is a bit oscillatory, there is no overshoot. This ensures that contouring accuracy is maintained for rapid motion commands.

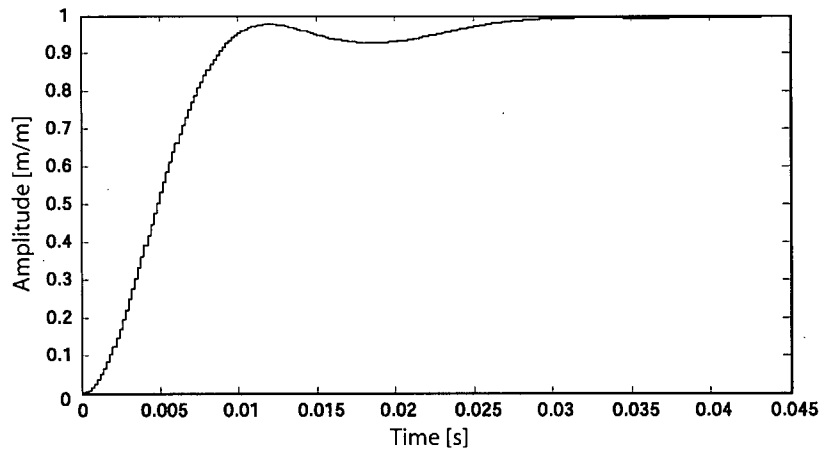


Figure 4.7: Unit Step Response of Position Closed-Loop of Rigid-Body based P-PI Controller Combined with Rigid-Body-Based Feed Drive Model

The Bode plots of the Sensitivity $S(z)$ and complementary sensitivity $T(z)$ functions depicted in Figure 4.8 also show the desired trends. $S(z)$ has a maximum value of -172 [dB] at 50 [Hz]. Generally, the sensitivity function has very low values at all frequencies due to the effect of the ballscrew gear reduction. This is one reason why ballscrew drives are preferred over direct drives. On the other hand, $T(z)$ which for this case also represents the closed-loop (CL) transfer function of the system, remains constant and then decreases monotonically after the cut-off (bandwidth) frequency.

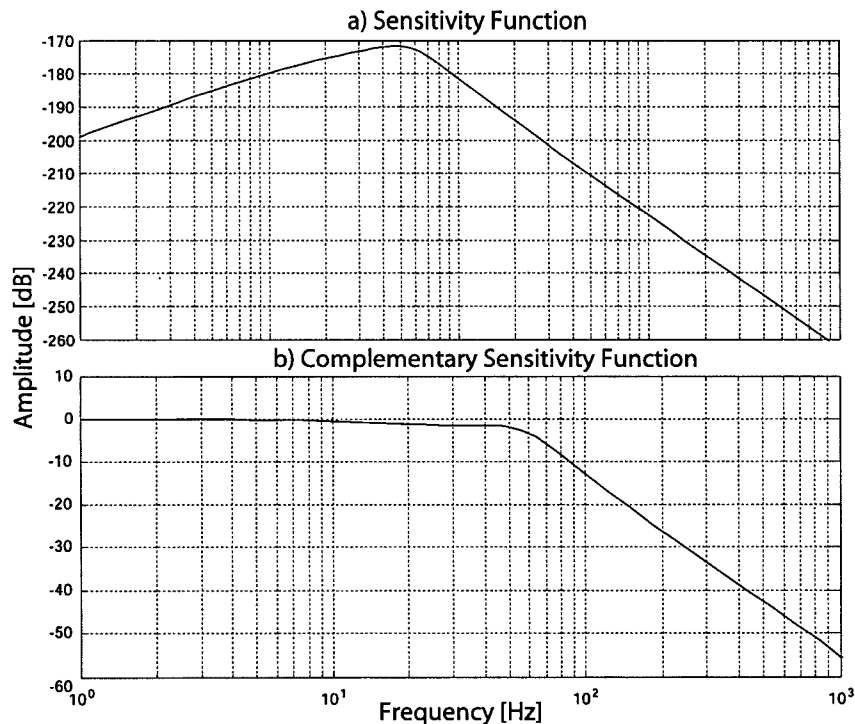


Figure 4.8: Sensitivity and Complementary Sensitivity Functions of Position Loop for Rigid-Body based P-PI Controller Combined with Rigid-Body-Based Feed Drive Model

4.4 Mitigation of Effects of Structural Dynamics on Controller Performance

In the previous section, the high-bandwidth P-PI controller was designed based on only the rigid-body dynamics of the drive. However, since the drive exhibits structural resonances at frequencies close to the control bandwidth, it is of interest to investigate how these structural dynamics influence the controller performance. In order to do this, the rigid-body transfer functions $G'_\omega(s)$, $G'_x(s)$ and $G'_d(s)$, used above for controller design, are respectively replaced by $G_\omega(s)$, $G_x(s)$ and $G_d(s)$, which provide a more realistic description of the feed

drive dynamics; because, in addition to the rigid-body dynamics, they also include the effects of the structural dynamics of the feed drive within the frequency range of interest. Figures 4.9 to 4.11 show OL Bode, CL Step, sensitivity and complementary sensitivity functions of the position loop at the C-Position. The plots for the other two positions closely resemble those of the C-Position; therefore they are not shown here to avoid repetition.

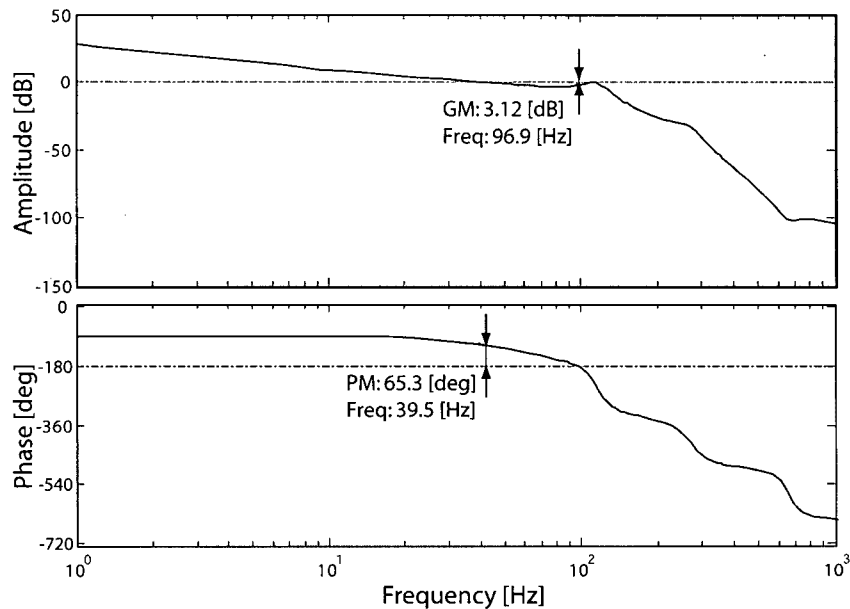


Figure 4.9: Open-Loop Bode Diagram for Position Loop of Rigid-Body-Based P-PI Controller Combined with Flexible Feed Drive Model

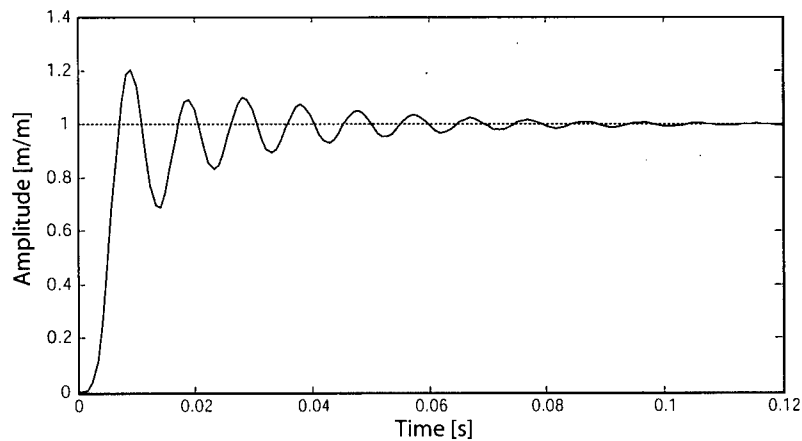


Figure 4.10: Unit Step Response for Position Loop of Rigid-Body based P-PI Controller Combined with Flexible Feed Drive Model

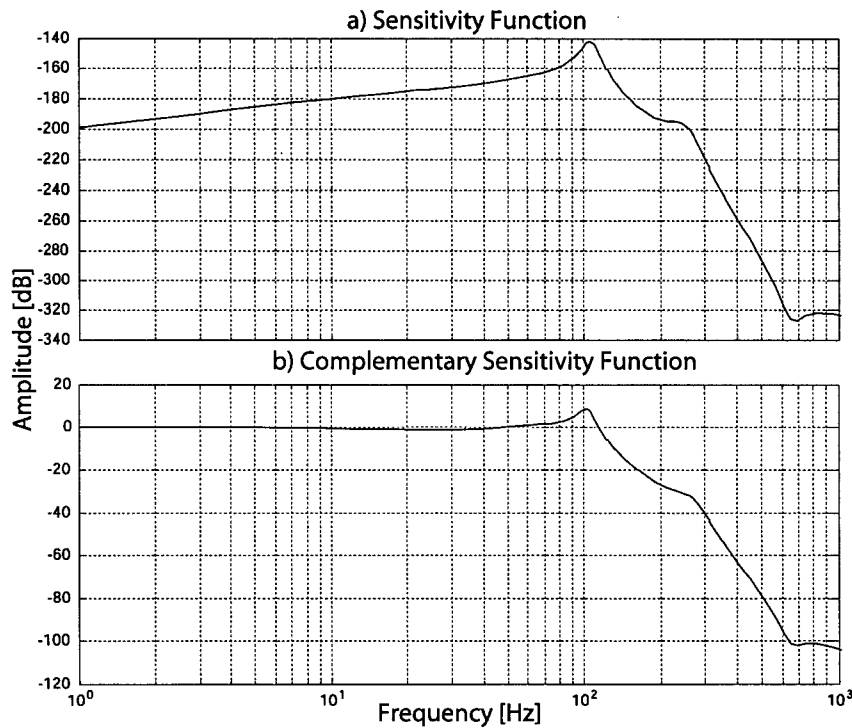


Figure 4.11: Sensitivity and Complementary Sensitivity Functions for Position Loop of Rigid-Body based P-PI Controller Combined with Flexible Feed Drive Model

Figure 4.9 shows that due to the structural dynamics at 118 and 271 [Hz], instead of obtaining a GM of 29.8 [dB] and a PM of 72.6 [deg] as indicated in Figure 4.6, a GM of 3.12 [dB] and PM of 65.3 [deg] are observed. This deterioration in the relative stability of the closed-loop system is reflected in the Unit Step Response shown in Figure 4.10, which exhibits a 20 [%] maximum overshoot and excessive oscillations at 100 [Hz] mainly caused by the axial mode of the ballscrew. As a result, a settling time of 72 [ms] as opposed to the anticipated 26 [ms] is observed. Also the sensitivity and complementary sensitivity functions in Figure 4.11 are affected by these dynamics. The peak of $S(z)$ increases, from -172 to -142 [dB], while $T(z)$ acquires a peak value of 8.82 [dB] at 103 [Hz], indicating an increase in the amount of measurement noise injected into the closed-loop system.

Considering the performance of the controller in the presence of the structural dynamics, it is clear that this design is unacceptable. Steps have to be taken to improve the design. Two

of the common methods of doing this are the modification of the mechanical design, and notch filtering of the structural modes of interest. Each of these techniques is applied to this set-up as presented in the following sections.

4.4.1 Modification of the Mechanical Design

In some cases, it is helpful to investigate the option of modifying the mechanical design as a simple and straightforward method of improving the performance of the controller. In order to do this, it is useful to examine the mode shapes of the problematic modes to find out the points of significant structural deformations. If possible, the mechanical design can be changed at such points in order to improve it.

For this set-up, an examination of the mode shapes show that in the first normal mode, as shown in Figure 4.12, a great part of the deformations are as a result of an axial stretching of the ballscrew between the nut and thrust bearing. In other words, this mode is directly linked to the axial stiffness of the ballscrew. In order to increase this stiffness, the diameter of the ballscrew must be increased, or its length reduced. Another alternative would be to use a stiffer material. Even though these changes are theoretically possible, practically they often would involve major changes in the design since ballscrews are usually manufactured as standard parts that have been selected to fit other dimensions of the machine. This is especially so in the case of this set-up. Therefore no modifications to the mechanical design are performed for this case.

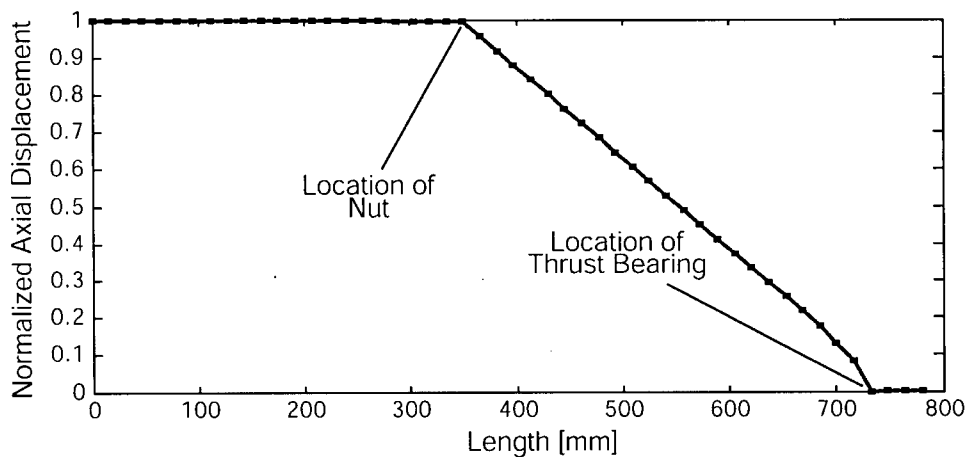


Figure 4.12: Axial Mode Shape of Ballscrew for First Normal Mode (C-Position)

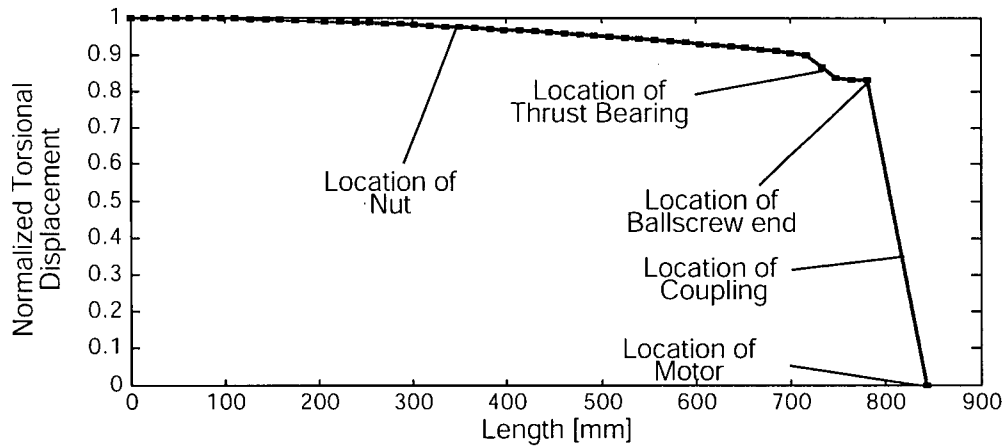


Figure 4.13: Torsional Mode Shape of Ballscrew for Second Normal Mode (C-Position)

The torsional mode shape for the second normal mode (Figure 4.13) reveals that the coupling joint is the greatest contributor to the deformations that occur in the mode. Therefore, in order to reduce the effects of this mode, a coupling of higher torsional stiffness (k_T) can be employed. From manufacturer's catalogs, it is found that using a bellow-type coupling instead of the jaw-type coupling originally used on the set-up can increase the torsional stiffness from its current value of $k_T=3,940$ [Nm/rad] to a catalog value of $k_T=45,940$ [Nm/rad], an increase of about twelve folds. By employing this new coupling, the natural frequency of the second mode is increased from values around 270 [Hz] to about 560 [Hz], such that it goes out of the frequency range of interest. The first mode, on the other hand is affected minimally. Hence, this modification has helped eliminate one of the problematic modes of the mechanical structure, leaving only one to be contended with. Consequently, the expressions for $G_\omega(s)$, $G_d(s)$ and $G_m(s)$ given in Eq.(4.5) to Eq.(4.7) can be simplified by totally eliminating the term corresponding to the second normal mode. Table 4.2 gives a summary of the new modal parameters after the modification

PARAMETER	VALUE		
	L-Position	C-Position	R-Position
f_{n1} [Hz]	112.46	121.50	139.88
ζ_1 [%]	6	6	6
$R_{\omega 1}$ [rad ² /(Nms ²)]	10.18	10.22	10.19
R_{m1} [rad ² /(Ns ²)]	-1.91×10^{-1}	-1.91×10^{-1}	-1.91×10^{-1}
R_{d1} [rad ² /(Ns ²)]	-1.91×10^{-1}	-1.91×10^{-1}	-1.91×10^{-1}
f_{n2} [Hz]	561.77	561.58	560.77
ζ_2 [%]	10	10	10
$R_{\omega 2}$ [rad ² /(Nms ²)]	27.19	27.17	27.22
R_{m2} [rad ² /(Ns ²)]	5.05×10^{-3}	5.30×10^{-3}	5.45×10^{-3}
R_{d2} [rad ² /(Ns ²)]	5.05×10^{-3}	5.30×10^{-3}	5.45×10^{-3}

Table 4.2: Parameters for Mechanical Sub-System Transfer Functions (After Modification)

4.4.2 Application of Notch Filter

Notch filtering is a classical method of providing a compensating network that avoids the unnecessary excitation of the resonant modes of a structure through pole-zero cancellation. The functioning of the notch filter can be better understood by taking a look at its Bode diagram (Figure 4.15). The filter introduces a notch at the frequency of the undesired mode, together with a phase that is negative below and positive above the resonant frequency. Placing this filter in the control loop ensures that the resonant modes will not be excited by the command signals or the control action. However, it does not introduce any damping to these modes. In other words, if these modes are excited, the system will respond in the same way as the open-loop system.

Since this set-up has two cascaded loops, and the inner loop is analog, it is desired to design a digital notch filter which can be implemented on a digital computer to cancel out the first resonant mode of the mechanical structure in the velocity closed loop. In other words, the notch filter will be placed in the position loop as shown in Figure 4.14.

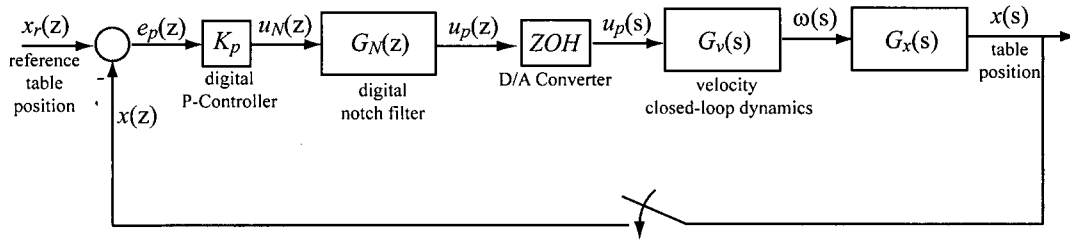


Figure 4.14: Digital Notch Filter in Position Loop

The structure of a the digital notch filter $G_N(z)$ is,

$$G_N(z) = K_N \frac{z^2 + n_1 z + n_2}{z^2 + d_1 z + d_2} \quad (4.18)$$

where n_1 and n_2 are the coefficients of the numerator polynomial of $G_N(z)$ corresponding to the coefficients of the complex conjugate poles to be cancelled, and d_1 and d_2 are those of the denominator polynomial corresponding to the coefficients of the new poles that replace the cancelled ones. K_N is an adjustment factor to ensure a steady-state gain of unity. It is calculated as,

$$G_N(z)|_{z=1} = K_N \frac{z^2 + n_1 z + n_2}{z^2 + d_1 z + d_2} \Big|_{z=1} = 1 \Rightarrow K_N = \frac{1 + d_1 + d_2}{1 + n_1 + n_2} \quad (4.19)$$

According to [25], even though the performance of notch filters can be affected adversely when there is a huge parameter mismatch that renders the pole-zero cancellation ineffective, this effect is greatly reduced when the parameter mismatch is small. This is particularly true when the poles to be canceled are sufficiently stable.

For this set-up, the first-mode for which the notch filter is designed exhibits parameter mismatch from one position to another due to the changing natural frequencies (Table 4.2). However, the effects of these changes have been examined and found to be quite small if the notch filter is designed based on the parameters of the C-Position, since its parameters lie in between those of the other two positions. However, it must be stressed that this situation is very specific. In some cases, it might be necessary to consider designing a notch filter whose parameters are scheduled based on the parameter variation from position to position.

For the C-Position, the damping ratio and natural frequency of the resonant mode are $\zeta_N=0.0855$ and $\omega_N=753.98$ [rad/s] ($f_N=120$ [Hz]), respectively. As explained above, in order to ensure pole-zero cancellation, these have to be the damping ratio and natural frequency of the numerator polynomial of $G_N(z)$. The coefficients n_1 and n_2 can be calculated based on these parameters and T_s , the sampling time of the system, as [3],

$$n_1 = -2e^{-\zeta_N\omega_N T_s} \cdot \cos(\omega_N T_s \sqrt{1-\zeta_N^2}); \quad n_2 = e^{-2\zeta_N\omega_N T_s} \quad (4.20)$$

In the denominator polynomial of $G_N(z)$, it is desired to have the same natural frequency of the numerator (i.e. $\omega_D=\omega_N=753.98$ [rad/s]). However, in order to attenuate the resonance magnitude of the mode, its damping ratio is increased to $\zeta_D=0.5$. Consequently, its coefficients d_1 and d_2 are calculated as,

$$d_1 = -2e^{-\zeta_D\omega_D T_s} \cdot \cos(\omega_D T_s \sqrt{1-\zeta_D^2}); \quad d_2 = e^{-2\zeta_D\omega_D T_s} \quad (4.21)$$

Table 4.3 gives a summary of the coefficients for the notch filter, and Figure 4.15 shows a Bode plot for the notch filter.

Parameter	n_1	n_2	d_1	d_2	K_N
Value	-1.9521	0.9745	-1.8390	0.8600	0.9402

Table 4.3: Coefficients of Notch Filter $G_N(z)$

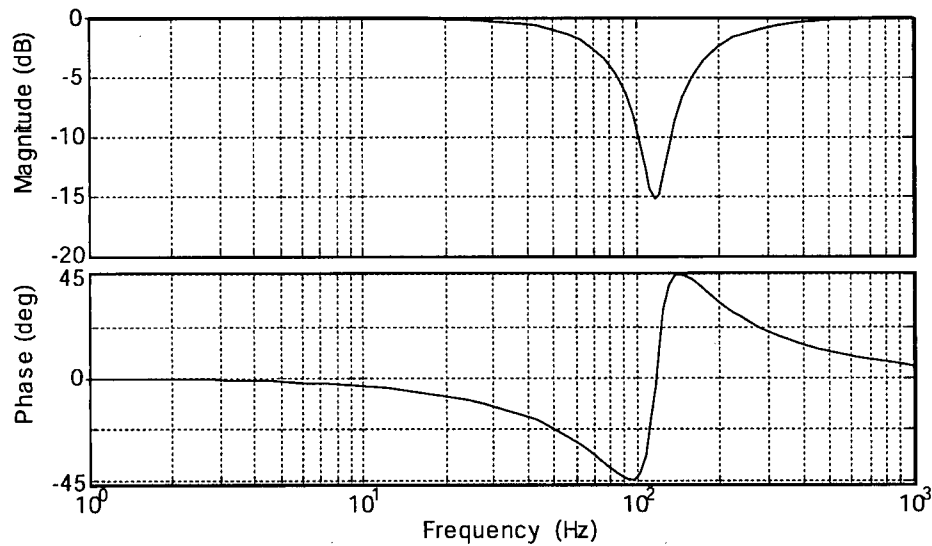


Figure 4.15: Bode Diagram of Notch Filter

Following the application of the notch filter, K_p is re-selected in order to achieve the desired response. A value $K_p=5000$ [V/m] is found to yield a closed-loop bandwidth of above 50 [Hz]. Figure 4.16 shows the Bode plot for the open-loop system of the re-designed P-PI controller and flexible feed drive with and without the notch filter (NF) at the L-Position, which represents the worst-case scenario in parameter mismatch due to position-dependent dynamics.

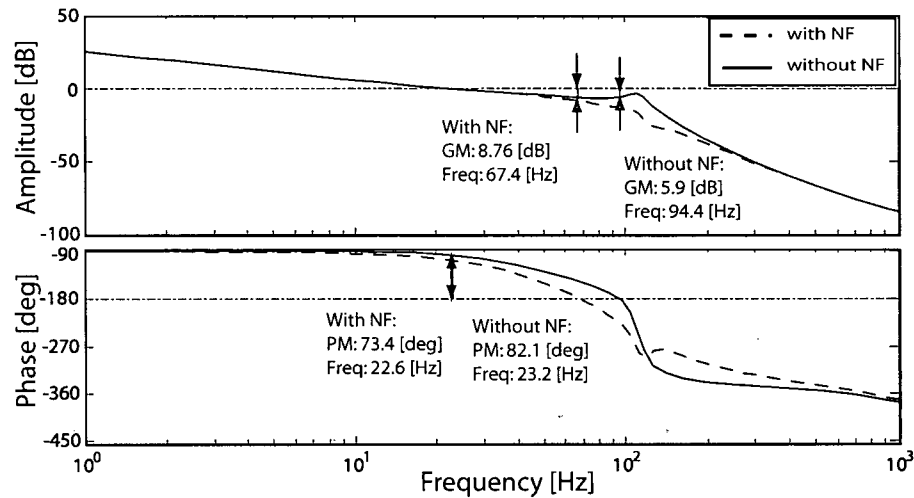


Figure 4.16: Open-Loop Bode of Position Loop for Re-designed P-PI Controller and Flexible Feed Drive with and without the Notch Filter

As seen from the figure, the addition of the notch filter introduces some attenuation to the resonance peak thereby increasing the gain margin from 5.9 to 8.76 [dB]. However on the other hand, there is some loss in phase margin from 82.1 to 73.4 [deg]. This trade of phase margin for gain margin is however a good one in this case because the gain margin is more critical in this situation. This can be seen more clearly from Figure 4.17 which shows the unit step response of the closed-loop system for both cases, also at the L-Position.

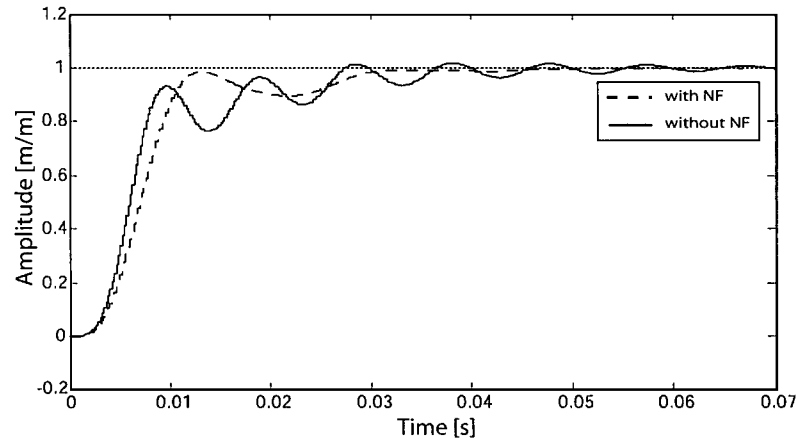


Figure 4.17: Unit Step Response of Position Loop for Re-designed P-PI Controller and Flexible Feed Drive with and without the Notch Filter

Without the notch filter, the response is very oscillatory with a settling time of 53 [ms] and a slight overshoot of 2 [%]. The frequency of the oscillations is now 106 [Hz] and still mainly due to the axial mode of the ballscrew. When the notch filter, is placed in the loop, the settling time reduces to 30 [ms]. Furthermore, the response is much more stable with less oscillations and no overshoot. This comes all as a result of the improved gain margin made possible by the notch filter.

Figure 4.18 shows the sensitivity and complementary sensitivity functions for the position loop of the re-designed P-PI controller and flexible feed drive with and without the notch filter. From plot (b), it is evident that the addition of the notch filter reduces the amount of measurement noise injected into the closed-loop system. Without the notch filter, $T(z)$ has a peak magnitude of 2.2 [dB] at 103 [Hz], while it crosses -3 [dB] at 111 [Hz]. However, with the notch filter, the magnitude peak is totally eliminated and the -3 [dB] crossing frequency is reduced to 63 [Hz] indicating a better attenuation of high-frequency noise.

Plot (a), on the other hand, shows that the notch filter does not improve the response to disturbances significantly. This is because, as mentioned previously, even though the notch filter is able to prevent the excitation of the resonant modes by the command signal and control action, when excited by the disturbance force which does not pass through the notch filter, the resonant mode responds in the same way as it would in the open-loop system. This is because the filter is unable to add damping to the resonant modes directly. In order to

improve the response to disturbances, a control structure which aims at compensating the resonant modes by adding more damping to them should be considered, as explained in the next section.

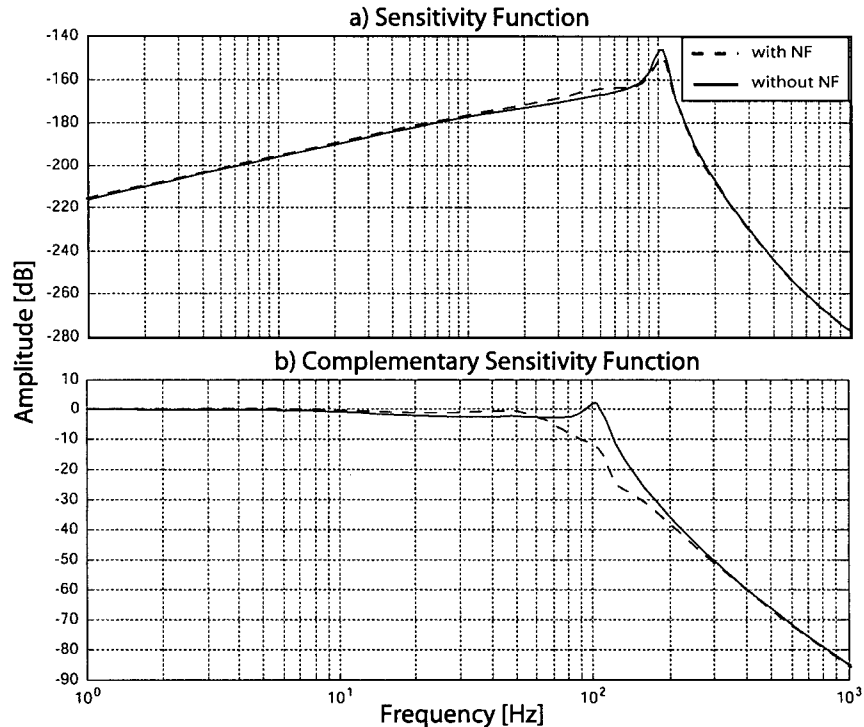


Figure 4.18: Sensitivity and Complementary Sensitivity Functions of Position Loop for Re-designed P-PI Controller and Flexible Feed Drive with and without the Notch Filter

4.5 Mode-Compensating Pole-Placement Controller

One control structure that makes it possible to compensate the oscillatory modes coming from the structural dynamics of the feed drive is the Pole-Placement Control (PPC) structure. This type of control, also known as RST control, makes use of the three polynomials, $R(z)$, $S(z)$ and $T(z)$ in the form of a feed-forward filter ($T(z)/R(z)$) and feed-back filter ($S(z)/R(z)$), shown in Figure 4.19, to indirectly place the poles of the closed-loop characteristic polynomial, $A_{cl}(z)$ such that a desired closed-loop response is obtained.

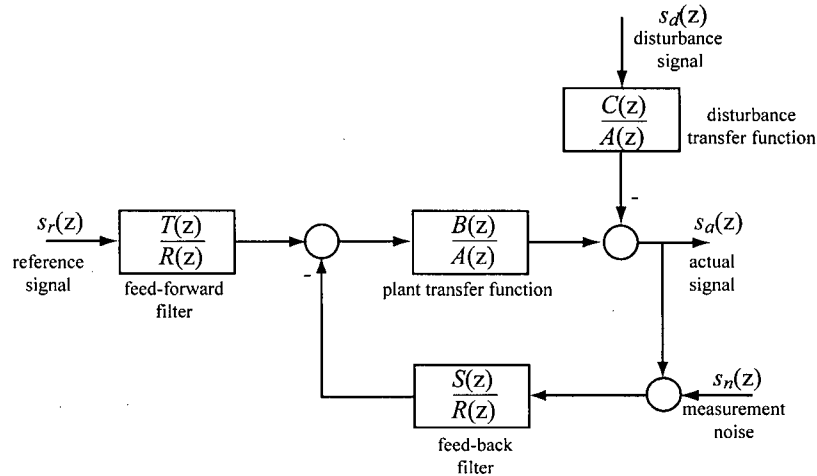


Figure 4.19: Topology of Pole-Placement Controller

From Figure 4.19, the relationship between $s_a(z)$, the actual signal, and the system inputs, namely the reference signal, $s_r(z)$, the disturbance signal, $s_d(z)$ and the measurement noise, $s_n(z)$ is,

$$s_a = \frac{BT}{AR + BS} s_r - \frac{CR}{AR + BS} s_d - \frac{BS}{AR + BS} s_n \quad (4.22)$$

In this equation, the dependent variable, z has been dropped in order to simplify the notation. This notation will be used frequently in this section.

As seen from the expression in Eq.(4.22), the characteristic equation is governed by $AR+BS$. Since the A and B polynomials both belong to the plant and so cannot be changed, the S and R polynomials can be used to adjust the roots of the characteristic equation.

In PPC design, the characteristic polynomial A_{cl} , is often factored into a product of two polynomials: a controller polynomial A_c , and an observer polynomial A_o , such that,

$$A_{cl} = A_c A_o \quad (4.23)$$

If the system is reachable, arbitrary eigenvalues (poles) can be assigned to A_c , while if the system is observable, arbitrary eigenvalues (poles) can be assigned to A_o . The eigenvalues to be assigned to these polynomials are chosen based on the desired closed-loop response of the system.

Also from Eq.(4.22), it is evident that the polynomial R influences the numerator dynamics of the disturbance response, while S affects the numerator dynamics of the noise response. Therefore, by forcing R to have a desired factor R_d , and S to have a desired factor S_d , a lot of control can be gained over these responses.

Furthermore, control designers sometimes prefer to cancel zeros and poles that are well-damped from the plant transfer function. In order to do this, it is helpful to factor the plant transfer function polynomials, A and B as,

$$A = A^+ A^-; \quad B = B^+ B^- \quad (4.24)$$

where A^+ and B^+ are the factors containing the well-damped poles and zeros, respectively, that can be cancelled. A^- and B^- , on the other hand, contain the poorly damped or unstable poles and zeros that cannot be cancelled. Considering that a process (plant transfer function) pole is cancelled by a controller zero and vice versa, the polynomials R and S can be written in term of their factors as,

$$R = B^+ R_d R^*; \quad S = A^+ S_d S^*; \quad (4.25)$$

R^* and S^* represent the remainder of the R and S polynomials, respectively after a division by their pre-specified factors.

In order to solve for the polynomials R and S , the expression for the characteristic polynomial, $AR+BS$ is equated to the desired characteristic polynomial A_{cl} to give,

$$A_{cl} = A_c A_o = AR + BS \quad (4.26)$$

Eq.(4.26) is known as the Diophantine Equation. This equation is tractable as long as A and B have no common factors (i.e. the plant is observable and reachable). However, in order to obtain a minimum-degree solution, the degree of A_{cl} ($\deg A_{cl}$) must satisfy the condition [3],

$$\deg A_{cl} = 2 \deg A + \deg R_d + \deg S_d - 1 \quad (4.27)$$

This condition is based on the assumption that $\deg S = \deg R$ (i.e. control signal computation time is negligible). Based on the same minimum-degree requirement, the degree of S is given by,

$$\deg S = \deg A + \deg R_d + \deg S_d - 1 \tag{4.28}$$

The T polynomial is usually chosen such that it consists of the observer polynomial, A_o multiplied by a scaling factor t_o . Since T strongly influences the tracking performance of the controller (Eq.(4.22)), t_o is used to insure that the system maintains a steady-state gain of unity. Hence,

$$\left. \frac{s_a}{s_r} \right|_{z=1} = \left. \frac{BT}{AR + BS} \right|_{z=1} = \left. \frac{Bt_o A_o}{A_c A_o} \right|_{z=1} = 1 \Rightarrow t_o = \frac{A_c(1)}{B(1)} \tag{4.29}$$

In order to implement this controller scheme on the set-up, the a few modifications have to be made to the open-loop system of Figure 4.1 in order to conform it to fit the system in Figure 4.19. These modifications are shown in Figure 4.20.

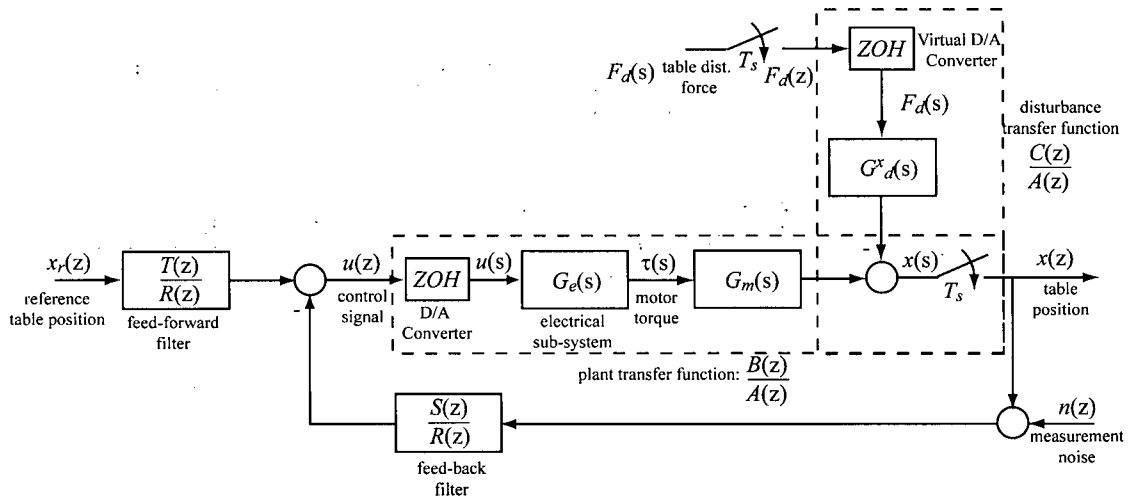


Figure 4.20: Pole-Placement Control Scheme

First, the transfer function product $G_\omega(s).G_x(s)$, is replaced by $G_m(s)$, while another transfer function $G_d^x(s)$ is defined to describe the dynamics between the table disturbance force, $F_d(s)$ and the table position $x(s)$. It is obtained from the transfer function $G_d(s)$ as,

$$G_d^x(s) = G_d(s) \cdot G_x(s) \tag{4.30}$$

Following these, the plant transfer function $B(z)/A(z)$ is easily obtained by finding the ZOH-equivalent pulse (discrete-time) transfer function of $G_e(s).G_m(s)$. In order to obtain the disturbance pulse transfer function $C(z)/A(z)$, it is assumed that the disturbance force $F_d(s)$ is

sampled and then converted back to continuous-time using a ZOH. For this assumption to be valid, $F_d(s)$ must be much slower than the sampling frequency.

Having converted the set-up's configuration to match that of Figure 4.19, the design follows quite simply. The design is conducted for the table at the C-Position.

The polynomials A and B are expressed in terms of their coefficients as,

$$\begin{aligned} A &= z^4 + a_1 z^3 + a_2 z^2 + a_3 z + a_4 \\ B &= b_0 z^3 + b_1 z^2 + b_2 z + b_3 \end{aligned} \quad (4.31)$$

The coefficients of the two polynomials are given in Table 4.4.

Coefficients of A			
a_1	a_2	a_3	a_4
-3.9580	5.8972	-3.9203	0.9811
Coefficients of B			
b_0	b_1	b_2	b_3
-2.7242×10^{-10}	8.0698×10^{-10}	3.9993×10^{-10}	-4.0367×10^{-10}

Table 4.4: Coefficients of Polynomials A and B

Based on these polynomials, the pole-zero map of B/A is shown in Figure 4.21.

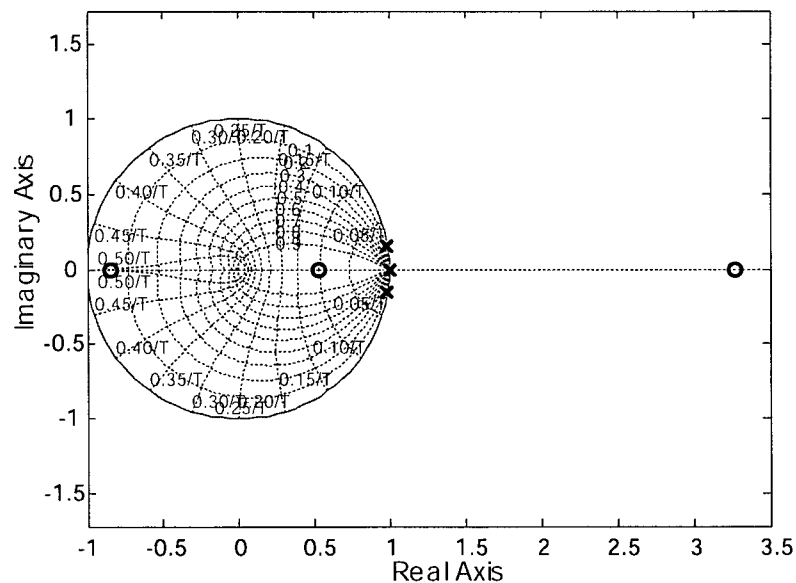


Figure 4.21: Pole-Zero Map of $B(z)/A(z)$

From the pole-zero map, it can be observed that only one zero ($z=0.535$) is sufficiently damped and so can be cancelled. There are also two well-damped poles, one at $z=1$ and the other at $z=0.999$, but these will not be cancelled since they are at a point of critical stability. Therefore,

$$A^+ = 1; \quad A^- = A; \quad B^+ = z - 0.535; \quad B^- = \frac{B}{B^+} \quad (4.32)$$

It is desired to have an integrator in R so that the steady-state error in $x(z)$ due to the disturbance $F_d(z)$ can be eliminated. Furthermore, it is desired that the measurement noise $n(z)$ should not give any error in $x(z)$ at the Nyquist Frequency ($z=-1$). Consequently, the polynomials R_d and S_d are given as,

$$R_d = z - 1; \quad S_d = z + 1 \quad (4.33)$$

Since $\deg A = 4$, $\deg R_d = 1$ and $\deg S_d = 1$, from Eq.(4.28), $\deg S = \deg R = 5$. Consequently, based on Eq.(4.25), they can be expressed as,

$$\begin{aligned} R &= B^+ R_d R^* = (z - 0.535)(z - 1)(z^3 + r_1 z^2 + r_2 z + r_3) \\ S &= A^+ S_d S^* = (z + 1)(s_0 z^4 + s_1 z^3 + s_2 z^2 + s_3 z + s_4) \end{aligned} \quad (4.34)$$

In order to determine the desired characteristic polynomial A_{cl} , $\deg A_{cl}$ is obtained from Eq.(4.27) as $\deg A_{cl} = 9$. Based on this information, $\deg A_c$ is set equal to four, while $\deg A_o$ is set to five.

The structure of A_c is chosen to be a product of B^+ , a real pole, and a pair of complex-conjugate poles of the form,

$$A_c = (z - 0.535)Z \left\{ (s + \alpha\omega_c)(s^2 + 2\zeta_c\omega_c s + \omega_c^2) \right\} \equiv (z - 0.535)(z + a_c)(z^2 + a_{c1}z + a_{c2}) \quad (4.35)$$

where $\zeta_c=1.0$ and $\omega_c=565.49$ [rad/s] (90 [Hz]) are the damping ratio and natural frequency of the complex-conjugate poles, while $\alpha=1$ is a scaling factor which determines how fast the real pole is with respect to the complex-conjugate poles. Z here represents an operator which maps the poles from the s to the z -domain. Based on this mapping, the coefficients a_c , a_{c1} and a_{c2} are calculated as,

$$a_c = -e^{-\alpha\omega_c T_s}; \quad a_{c1} = -2e^{-\zeta_c\omega_c T_s} \cdot \cos(\omega_c T_s \sqrt{1-\zeta_c^2}); \quad a_{c2} = e^{-2\zeta_c\omega_c T_s} \quad (4.36)$$

As for the observer polynomial A_o , it is assumed to consist of a product of a pair of complex-conjugate poles and three poles at the origin of the z -plane. It is expressed as,

$$A_o = z^3 Z \left\{ (s^2 + 2\zeta_o\omega_o s + \omega_o) \right\} \equiv z^3 (z^2 + a_{o1}z + a_{o2}) \quad (4.37)$$

The natural frequency of the complex-conjugate poles of A_o , $\omega_o=763.43$ [rad/s] (121.5 [Hz]), is chosen to coincide with the natural frequency of the resonant mode in the feed drive structure. However, its damping is changed from 0.06 to $\zeta_o = 0.7071$. The values of a_{o1} and a_{o2} are thus obtained as,

$$a_{o1} = -2e^{-\zeta_o\omega_o T_s} \cdot \cos(\omega_o T_s \sqrt{1-\zeta_o^2}); \quad a_{o2} = e^{-2\zeta_o\omega_o T_s} \quad (4.38)$$

The numerical values for the coefficients of A_{cl} are summarized in Table 4.5

Coefficient	a_c	a_{c1}	a_{c2}	a_{o1}	a_{o2}
Value	-0.8930	-1.7861	0.7975	-1.7849	0.8057

Table 4.5: Coefficients of Desired Characteristic Equation, A_{cl}

With the desired characteristic polynomial A_{cl} completely defined, the Diophantine Equation (Eq.(4.26)) is solved and the coefficients of R and S are obtained. Furthermore, the value of t_o is obtained using Eq.(4.29). Their numerical values are given in Table 4.6.

Coefficient	r_1	r_2	r_3	t_0	
Value	0.5759	0.5490	0.2000	1.0702×10^6	
Coefficient	s_0	s_1	s_2	s_3	s_4
Value	3.0078×10^8	-1.1554×10^9	1.6693×10^9	-1.07516×10^9	2.6038×10^8

Table 4.6: Coefficients of the R, S and T Polynomials

Figure 4.22 shows the open-loop Bode plot for the position loop. The gain margin obtained with this controller is 2.55 [dB], which is significantly less than that obtained using the notch filter. The same problem is also observed in the phase margin, which in this case is 31.7 [deg]. This deterioration of gain and phase margins comes as a result of the extra free-integrator forced into the controller through the R polynomial, for the purpose of attenuating constant disturbance forces. In order to improve these margins, for better robustness, the loop

can be closed on the table velocity or the constraint imposed on R can be relaxed, hence eliminating one of the free integrators.

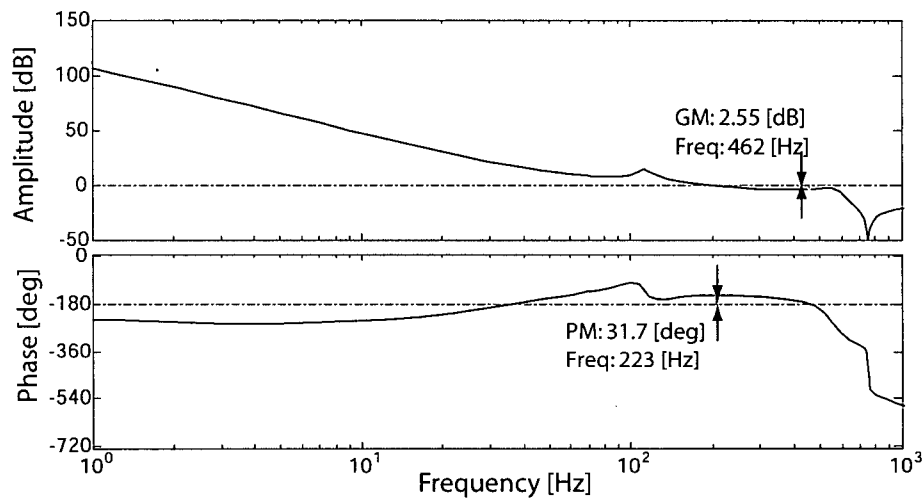


Figure 4.22: Open-Loop Bode of Position Loop Controlled with the PPC

The unit step response of the system (Figure 4.23) shows that the poor gain and phase margin do not deteriorate the tracking performance of the controller. The settling time for the PPC controller is about 15 [ms], without any oscillations or overshoots, while even with the notch filter, the re-designed P-PI controller had a settling time of 30 [ms] with slight oscillations.

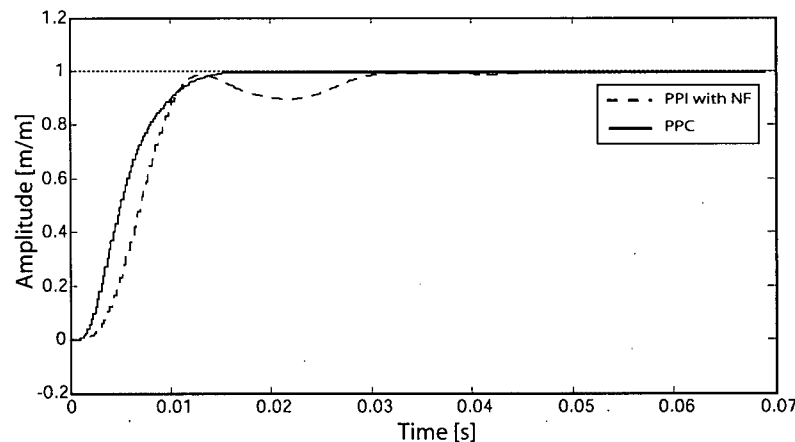


Figure 4.23: Unit Step Response for Position Closed-Loop of PPC and Re-designed P-PI Controller with Notch Filter

The plots for the sensitivity and complementary sensitivity functions in Figure 4.24 show, that the PPC controller improves the disturbance response at low frequencies, particularly in the region around the closed-loop bandwidth of 50 [Hz]. This improvement comes as a result of the damping added to the oscillatory modes of the feed drive structure, which could not be damped using the notch filter. The effect of the additional damping can be better observed from the response of both systems to a unit step disturbance, as shown in Figure 4.25. As seen, the response of the re-designed P-PI with Notch Filter takes 150 [ms] to settle, while the PPC settles in 20 [ms].

Unfortunately, the PPC controller, when compared to the P-PI with notch filter, introduces more measurement noise into the closed-loop system at high frequencies. The constraint on the complementary sensitivity function enforced by the S polynomial ensures that it has a zero value at the Nyquist Frequency, but cannot guarantee low values of complementary sensitivity at other frequencies. Therefore, it may be necessary to place more constraints at the other frequencies, if the system is exposed to a significant amount of measurement noise.

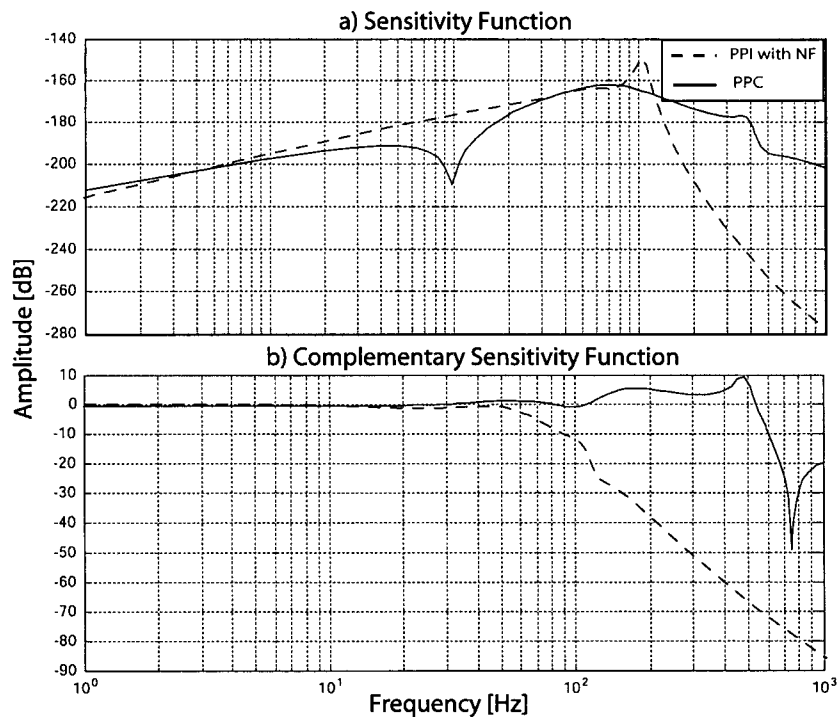


Figure 4.24: Sensitivity and Complementary Sensitivity Functions for Position Loop of PPC and Re-designed P-PI Controller with Notch Filter

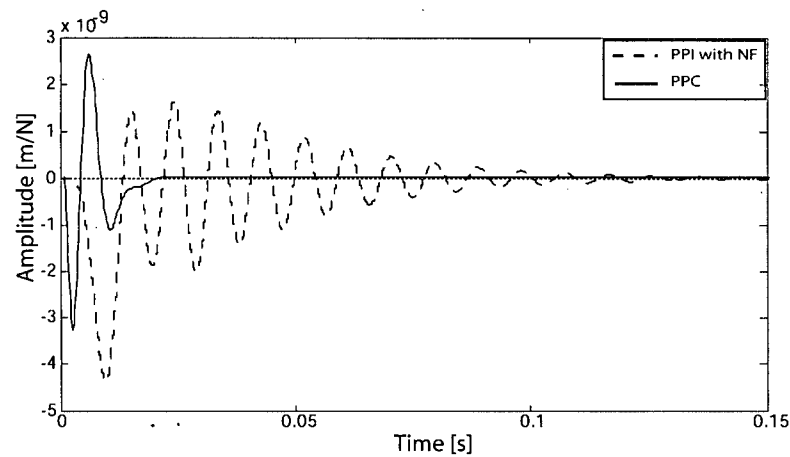


Figure 4.25: Unit Step Disturbance Response for Position Closed-Loop of PPC and Re-designed P-PI Controller with Notch Filter

4.6 Summary

In this chapter, the importance of considering the structural dynamics of a feed drive during controller design has been shown through two controller design examples. First, a P-PI controller is designed based on rigid-body dynamics and then implemented on a feed drive model which includes structural dynamics. By means of the frequency and time-domain characteristics of the system, it is observed that a significant deterioration of performance results due to the effects of the resonances of the mechanical structure. In order to improve the performance of the controller, the structural dynamics is taken into account, and modifications are first made on the mechanical design, then a notch filter is implemented, and finally, a mode-compensating PPC controller is designed. All these together show that the consideration of the structural dynamics of the drive is a better alternative to a design performed based on only rigid-body dynamics considerations. They therefore highlight the importance of the modeling scheme presented in the previous chapter. Furthermore, they will be used in the simulation scheme described in the following chapter, in order to investigate the interaction between controller and feed drive dynamics.

Chapter 5

Interactive Simulation of Feed Drive-Controller Performance

5.1 Overview

The purpose of this chapter is to extend and reconfigure the linear FE model for ballscrew drives presented in Chapter Three to make it suitable for time-domain performance simulations. In order to do this, first of all a realistic simulation model for the mechanical system of the feed drive has to be generated from the FE Model. This challenge is treated in Section 5.2, where one of the major issues considered is the incorporation of some of the typical non-linearities of ballscrew drives into the simulation model. Another issue considered in Section 5.2 is the shortening of the duration of simulations through model reduction. This is because time-domain simulations for complex systems are often computationally intensive and time-consuming, neither of which is desirable for practical purposes. In Section 5.3, the resulting simulation model for the feed drive's mechanical system is implemented on a commercial simulator for the experimental set-up described in Chapter Three. Moreover, controller dynamics from the previous chapter, and some process dynamics are also added, and interactive simulations are performed in order to examine various properties of the feed drive axis. Finally, the highlights of the chapter are summarized in Section 5.4.

5.2 Generation of Simulation Model of Feed Drive

5.2.1 State-Space Representation of the Linear Dynamics

The FE Model of the ballscrew drive, as mentioned in Chapter Three, results in a set of linear differential equations which can be expressed in matrix form as,

$$\mathbf{M}_{model}\ddot{\mathbf{d}} + \mathbf{C}_{model}\dot{\mathbf{d}} + \mathbf{K}_{model}\mathbf{d} = \mathbf{F} \quad (5.1)$$

where \mathbf{M}_{model} , \mathbf{C}_{model} and \mathbf{K}_{model} are respectively the mass, viscous damping and stiffness matrices of the model, while \mathbf{d} represents the vector of generalized displacements and \mathbf{F} is the vector of generalized forces.

As in the case of the controller design, this dynamics of the model can be represented in various forms for simulation purposes. However, the state-space (SS) approach is often preferred above other representations because it lends itself better to numeric mathematical manipulations. Furthermore, in the state-space representation, the effects of initial conditions can also be captured.

Generally, the state-space representation of a linear system can be expressed as,

$$\begin{aligned}\dot{\mathbf{x}} &= \mathbf{A}\mathbf{x} + \mathbf{B}\mathbf{u} \\ \mathbf{y} &= \mathbf{C}\mathbf{x} + \mathbf{D}\mathbf{u}\end{aligned}\quad (5.2)$$

Where \mathbf{x} , \mathbf{u} and \mathbf{y} are the state, input and output vectors of the system, respectively. If the state-vector in Eq.(5.2) is chosen such that it consists of the model's vector of generalized displacements, \mathbf{d} and its derivative, $\dot{\mathbf{d}}$ then the matrices \mathbf{A} and \mathbf{B} are written as,

$$\mathbf{A} = \begin{bmatrix} \mathbf{0} & \mathbf{I} \\ -\mathbf{M}_{model}^{-1}\mathbf{K}_{model} & -\mathbf{M}_{model}^{-1}\mathbf{C}_{model} \end{bmatrix}; \quad \mathbf{B} = \begin{bmatrix} \mathbf{0} \\ \mathbf{M}_{model}^{-1} \end{bmatrix} [\mathbf{T}_{F-u}]; \quad \text{where } \mathbf{x} = \begin{Bmatrix} \mathbf{d} \\ \dot{\mathbf{d}} \end{Bmatrix} \quad (5.3)$$

\mathbf{T}_{F-u} in Eq.(5.3) is a matrix which transforms the input vector, \mathbf{u} into the vector of generalized forces, \mathbf{F} . If \mathbf{T}_{F-u} is omitted from the expression for \mathbf{B} , then the inputs are assumed to be expressed as forces (i.e. $\mathbf{u}=\mathbf{F}$).

The output vector, \mathbf{y} is related to \mathbf{x} and \mathbf{u} through the matrices \mathbf{C} and \mathbf{D} , respectively. In most cases, $\mathbf{D}=\mathbf{0}$, while \mathbf{C} can simply be set to an identity matrix so that the output vector is identical to the state-vector (i.e. $\mathbf{y}=\mathbf{x}$).

Diagrammatically, the model expressed by Eq.(5.2) and Eq.(5.3) can be viewed as a dynamic state-space block, SS_{model} , having input ports into which forces are fed, and output ports from which the states (displacements and velocities) of the system can be tapped as shown in Figure 5.1.

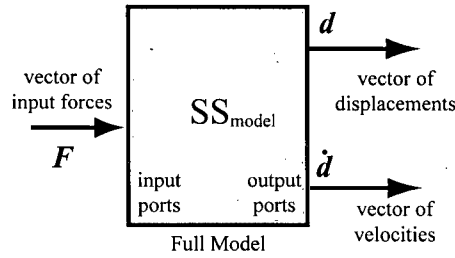


Figure 5.1: Diagrammatic Representation of State-Space Model

The model represented by Eq.(3.44) consists of several components (rigid-bodies and finite element structures) connected by joint interfaces. For simulation purposes, it is often desired to split the model into two or more sub-models, so that the non-linear dynamics at the joint interfaces between them can be realistically included into the simulation. A typical example of such a case is the joint at the screw-nut interface, where important non-linearities like nut backlash and position-dependent dynamics take place.

Considering the simplest case where the full model is to be split into only two sub-models with one joint connection between them, the differential equations describing the dynamics of the model (Eq.(3.44)) can be re-arranged as,

$$\underbrace{\begin{bmatrix} M_{sm1} & 0 \\ 0 & M_{sm2} \end{bmatrix}}_{M_{model}} \underbrace{\begin{Bmatrix} \ddot{d}_{sm1} \\ \ddot{d}_{sm2} \end{Bmatrix}}_{\ddot{d}} + \underbrace{\begin{bmatrix} C_{sm1} & 0 \\ 0 & C_{sm2} \end{bmatrix}}_{C_{model}} \underbrace{\begin{Bmatrix} \dot{d}_{sm1} \\ \dot{d}_{sm2} \end{Bmatrix}}_{\dot{d}} + \underbrace{\begin{bmatrix} K_{sm1} & 0 \\ 0 & K_{sm2} \end{bmatrix}}_{K_{model}} \underbrace{\begin{Bmatrix} d_{sm1} \\ d_{sm2} \end{Bmatrix}}_d = \underbrace{\begin{Bmatrix} F_{sm1} \\ F_{sm2} \end{Bmatrix}}_F \quad (5.4)$$

The subscripts $sm1$ and $sm2$ respectively indicate a matrix or vector belonging to the first and second sub-model, while C_{joint} and K_{joint} are the damping and stiffness matrices of the joint connecting the two sub-models.

From Eq.(5.4), it is clear that, excluding the joint interface matrices, the dynamic equations for each of the sub-models can be written independently as,

$$\begin{aligned}
 M_{sm1} \ddot{d}_{sm1} + C_{sm1} \dot{d}_{sm1} + K_{sm1} d_{sm1} &= F_{sm1} \\
 M_{sm2} \ddot{d}_{sm2} + C_{sm2} \dot{d}_{sm2} + K_{sm2} d_{sm2} &= F_{sm2}
 \end{aligned} \quad (5.5)$$

Hence, following the same procedure as for the full model, each sub-model can be converted into a state-space description, SS_{sm1} and SS_{sm2} . On the other hand, the stiffness and viscous damping matrices of the joint interface can be implemented in time-domain as direct and cross-coupling springs and viscous dampers having the stiffness and damping constants derived from the elements of K_{joint} and C_{joint} , respectively. Figure 5.2 shows the schematic of an example of this implementation for a simple case where the K_{joint} and C_{joint} represent a single spring stiffness, k and damping constant, c between an attachment point on Sub-model 1 and another on Sub-model 2.

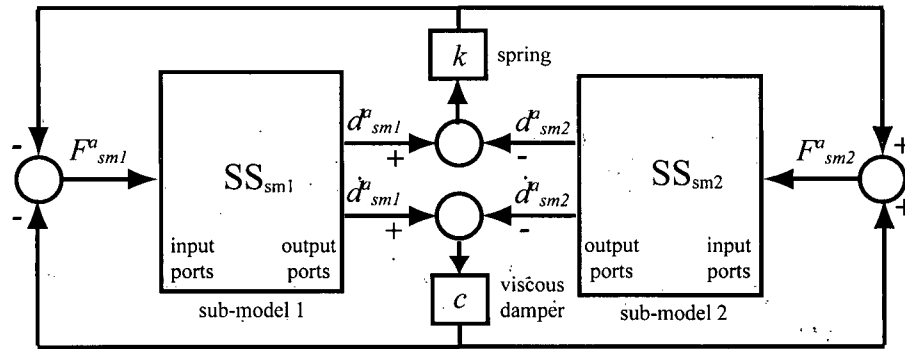


Figure 5.2: Sample Implementation of Joint Stiffness and Damping Matrices

d_{sm1}^a and d_{sm2}^a in the figure respectively represent the displacements of the attachment point on Sub-model 1 and Sub-model 2, while \dot{d}_{sm1}^a and \dot{d}_{sm2}^a represent their velocities. F_{sm1}^a and F_{sm2}^a on the other hand, are the reaction forces on each of the sub-models due to the stretching of the spring, k and motion of the viscous damper, c . Even though this model-splitting procedure has been described for a simple case, it can be implemented quite easily for multiple joints having complex stiffness and viscous damping matrices.

5.2.2 Incorporation of the Non-Linear Dynamics

In ballscrew drive systems, various forms of non-linearities are present. As in the case of the linear model presented in Chapter Three, these non-linear dynamics can be grouped into those arising from elements in the electrical sub-system and those stemming from the mechanical components. In the electrical sub-system, typical non-linearities include saturation limits in the amplifier, delays from the D/A converters and quantization errors

from the measurement devices. On the mechanical side, the most common non-linearities are coulomb and static friction (e.g. at the guideways), backlash at the joint interfaces (e.g. at the screw-nut interface), and the position-dependent structural dynamics variations described in Chapter Three.

Since the modeling in this thesis is focused on the mechanical sub-system, the non-linearities in the electrical sub-system, even though significant, will not be dealt with here; only those arising from the mechanical components will be tackled.

5.2.2.1 Coulomb and Static Friction

Coulomb and static friction exist at every sliding interface in the drive system. However, their effects are most felt at the guideway interface because of the huge mass of the table resting on the guides which gives rise to large normal forces. Therefore while they can be neglected at the other sliding surfaces, they cannot be disregarded at the guideways.

The friction characteristics for lubricated metallic surfaces in contact can best be described by the Stribeck friction curve shown in Figure 5.3 [2]. This curve consists of four different regions – the static friction, boundary lubrication, partial-fluid lubrication and full-fluid lubrication, regions.

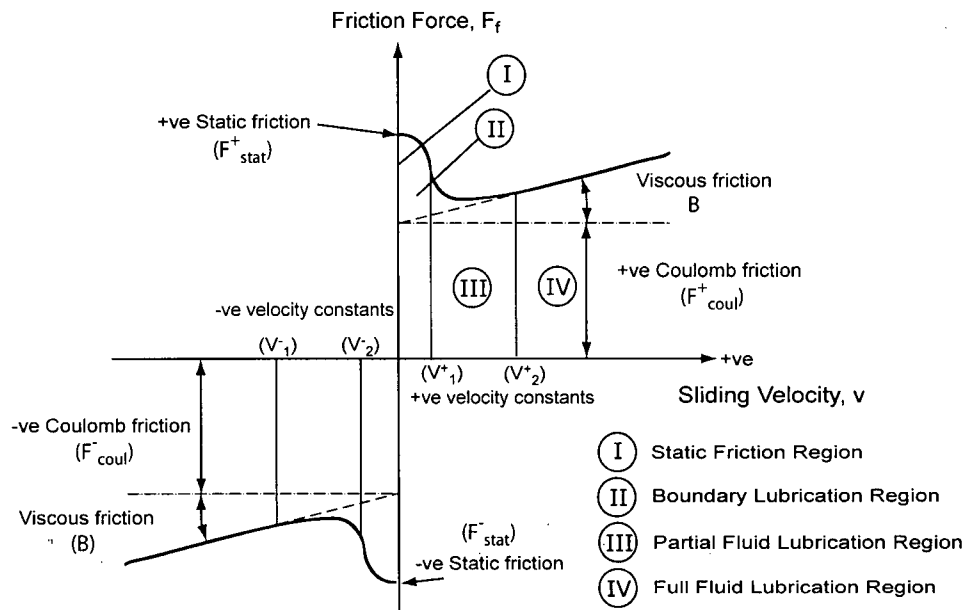


Figure 5.3: The Stribeck Friction Curve

When a force is applied to one of the bodies in contact, so as to make it slide relative to the other, the interlocking asperities between the two surfaces are elastically deformed. During this period, there is no relative motion between the bodies; hence it is called the static friction region. When a certain threshold, $F_{stat}^{+/-}$ is reached, the interlocking asperities disengage and motion begins, with a sliding (relative) velocity of v between the two bodies. Initially, the sliding velocity is low, so a consistent film of lubricant cannot be formed between the contact surfaces. Therefore, during this period, sliding occurs between the thin layers of lubricant trapped on the contact surfaces. This phenomenon is known as boundary lubrication. In the partial-fluid lubrication region, the sliding velocity is enough to cause a lubricant film to form between the surfaces. However, this film is not thick enough to completely separate the two contact surfaces; therefore there is still some metal-to-metal contact between them. After the sliding velocity reaches a sufficiently high level, a thick and continuous film of lubricant is formed between the surfaces, completely separating them. Here, the viscosity of the lubricant dominates the friction force, giving rise to what is known as the viscous friction or full-fluid region.

Considering the characteristics of the Stribeck friction curve described above, an analytical formulation for the non-linear variation of the Friction Force, F_f with the sliding velocity, v between the two bodies can be given as [14],

$$F_f^{+/-}(v) = F_{stat}^{+/-} \cdot e^{-v/V_1^{+/-}} + F_{coul}^{+/-} \cdot (1 - e^{-v/V_2^{+/-}}) + B \cdot v \quad (5.6)$$

$F_{stat}^{+/-}$ and $F_{coul}^{+/-}$ are respectively the static and Coulomb friction forces, while $V_1^{+/-}$ and $V_2^{+/-}$ are velocity thresholds which are used to demarcate the different friction regions described above. $V_1^{+/-}$ determines the spacing between the boundary and partial-fluid, lubrication regions, while $V_2^{+/-}$ regulates the spacing between the partial-fluid and full-fluid, lubrication regions. The superscript $+/-$ appearing in the equation indicates a choice between the positive and negative constants depending on the sign of the velocity. In Eq.(5.6), a viscous damping term, $B \cdot v$, representing the viscous damping force on the rigid-body motion has also been included. This is based on an assumption that the model's viscous damping matrix, C_{model} was derived from modal damping ratios (see Appendix A), and so does not include the damping on the rigid-body mode. However, if this effect has already been included in C_{model} , it should be excluded from the friction force expression.

Even though the expression for F_f given in Eq.(5.6) is complicated, it can be simplified, if need be, by taking its limit as $V^{+/-}_1$ and $V^{+/-}_2$ approach zero, so that the expression reduces to,

$$F_f^{+/-}(v) = F_{coul}^{+/-} + B \cdot v \quad (5.7)$$

Irrespective of the expression used, the effect of F_f can be incorporated into the simulation model by simply calculating the sliding velocity, v from the velocity states, \dot{d}^1 and \dot{d}^2 of the components concerned, and feeding it into a friction dynamics block which represents Eq.(5.6) or Eq.(5.7). The resulting friction force, F_f is then applied to the force inputs of the components, F^1 and F^2 as a disturbance force as shown in Figure 5.4.

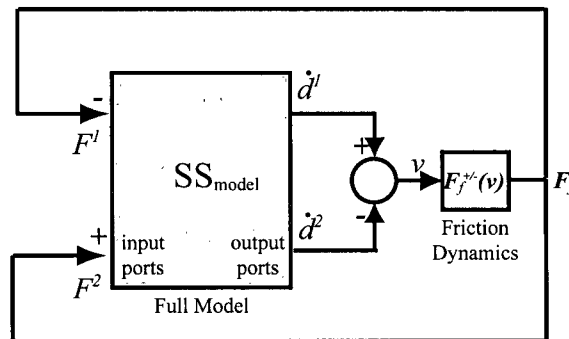


Figure 5.4: Incorporation of Friction into Simulation Model

5.2.2.2 Backlash

Backlash is a non-linear position-dependent dynamics which mostly results from the presence of a clearance between two mechanical elements. One of the interfaces where a significant amount of backlash-like dynamic behaviour is observed in a ballscrew drive is the screw-nut interface [10]. Some other joint interfaces may also exhibit a similar behaviour depending on how they are designed. It is necessary to consider backlash in the simulation model because it gives rise to a hysteretic behaviour which may degrade the performance of the ballscrew drive.

Generally, the mechanism of backlash can be described using the classical dead-zone model depicted in Figure 5.5. According to this model, the input and output mechanical

elements can either be in a disengaged state (Case 1), engaged in a positive direction (Case 2) or engaged in a negative direction (Case 3).

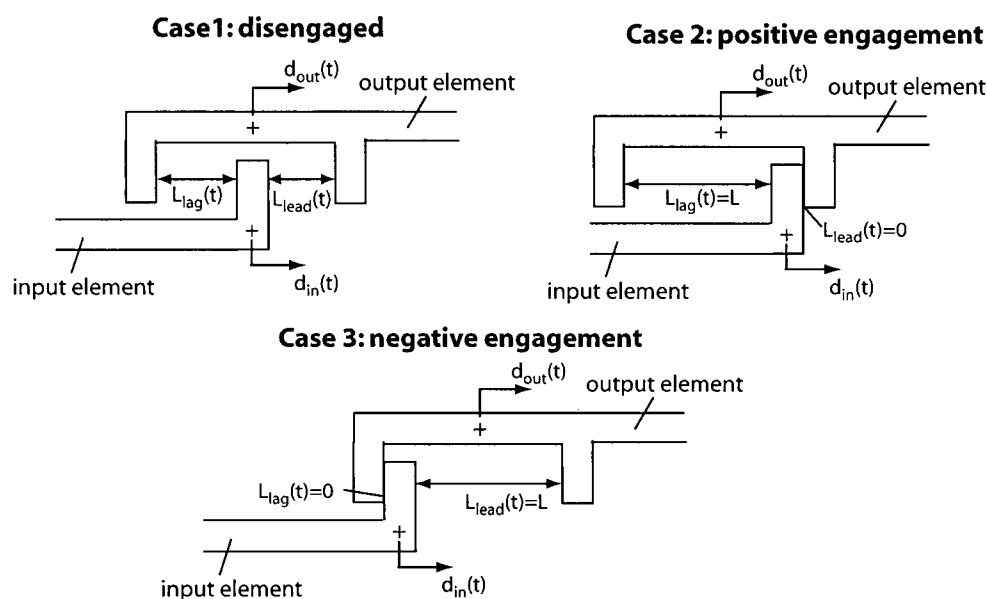


Figure 5.5: Classical Dead-Zone Backlash Model

Mathematically, the relationship between $d_{in}(t)$, the displacement of the input element at any given instant, and $d_{out}(t)$, the displacement of the output element at the same instant can be described as,

$$d_{out}(t) = \begin{cases} 0; & -L_{lag}(t) < d_{in}(t) < L_{lead}(t) \\ d_{in}(t); & \text{otherwise} \end{cases} \quad (5.8)$$

In the equation, $L_{lag}(t)$ and $L_{lead}(t)$ are respectively the instantaneous distance between the input element, and the left and right limits of the dead-zone having an effective clearance of length L (see Figure 5.5). Initially, they are both set to a value of half the length of the dead-zone (i.e. $L_{lag}(0) = L_{lead}(0) = L/2$), and as time goes on, they are updated based on the rule,

$$L_{lag}(t) = \begin{cases} L_{lag}(t-1) + d_{in}(t); & 0 < L_{lag}(t) < L \Rightarrow (\text{Case 1}) \\ L; & L_{lag}(t) > L \Rightarrow (\text{Case 2}) \\ 0; & L_{lag}(t) < 0 \Rightarrow (\text{Case 3}) \end{cases} \quad (5.9)$$

$$L_{lead}(t) = \begin{cases} L_{lead}(t-1) - d_{in}(t); & 0 < L_{lead}(t) < L \Rightarrow (\text{Case 1}) \\ 0; & L_{lead}(t) < 0 \Rightarrow (\text{Case 2}) \\ L; & L_{lead}(t) > L \Rightarrow (\text{Case 3}) \end{cases}$$

Unlike the friction dynamics described in the previous section, in order to implement backlash dynamics in the simulation model, the entire model has to be split up into sub-models at the joint location concerned. This is because the backlash represents a kind of switch which connects and disconnects two sub-models at the joint in between them. For instance, assuming some backlash dynamics is present at the joint interface between SS_{sm1} and SS_{sm2} , shown in Figure 5.2; it can be incorporated into the joint interface as shown in Figure 5.6.

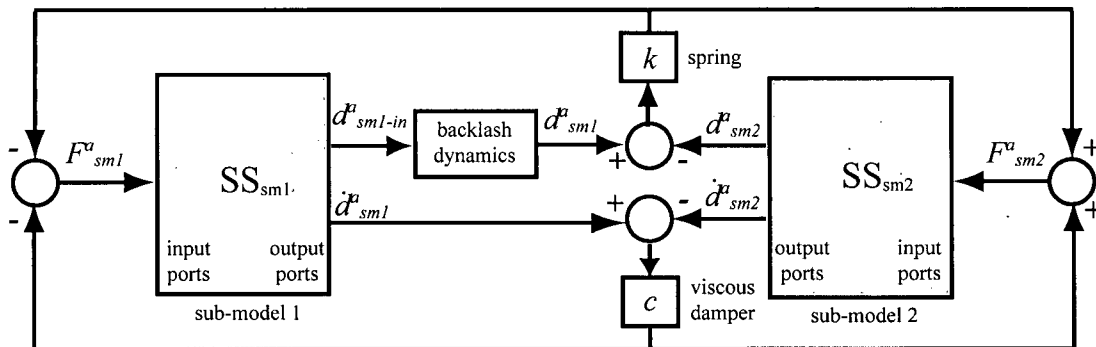


Figure 5.6: Incorporation of Backlash into Simulation Model

The “backlash dynamics” block in the figure essentially executes the backlash model given by Eq.(5.8) and (5.9). d_{sm1-in}^a is the displacement of the attachment point excluding the effects of backlash. It represents $d_{in}(t)$ in the backlash model of Figure 5.5. d_{sm1}^a , on the other hand, is the actual displacement of the attachment point, considering backlash. It is similar to $d_{out}(t)$ in Figure 5.5.

5.2.2.3 Position-Dependent Structural Dynamics Variations

In Chapter Three, the variation of the ballscrew drive dynamics as the nut moves along the ballscrew was discussed in detail. The natural frequencies and amplitudes of the system's open-loop response were seen to change from position to position. Furthermore, in Chapter Four, this changing open-loop dynamics was also shown to affect closed-loop dynamics of the controlled system.

Therefore, considering that while executing motion commands, the table and nut have to continuously move from one position to the other, these position-dependent changes in dynamics have to be incorporated in the simulation model in order to observe their effects.

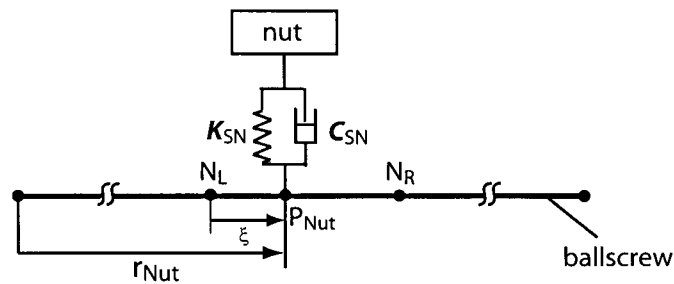


Figure 5.7: Movement of Screw-Nut Interface Joint along Ballscrew

Figure 5.7 shows the mechanism for this variation. As the nut moves along the threaded section of the ballscrew, the screw-nut interface joint moves from one attachment point, P_{Nut} to the other. The interface joint is represented by the screw-nut interface stiffness matrix, K_{SN} and damping matrix, C_{SN} (if available). r_{Nut} is the instantaneous position vector of the nut measured from the beginning of the threaded portion of the ballscrew. Since the ballscrew model consists of an FE beam with discrete nodes, the information at any nut attachment point, P_{Nut} , is provided by the information at the nodes, N_L and N_R , to the immediate left and right of it. ξ is the distance from N_L to P_{Nut} at any time.

In the simulation model, the effect of this position-dependent dynamic variation can be captured by grouping the ballscrew and other components attached to it as one sub-model (sub-model 1), and grouping the nut and the other components attached to it as another sub-model (sub-model 2), as shown in Figure 5.8. Then the screw-nut interface stiffness and damping matrices K_{SN} and C_{SN} are substituted as the joint interface matrices. Since the nut attachment point, P_{Nut} is continuously changing, a selection block is also introduced in order

to select the state vectors, $(\dot{d}_{sm1}^{aL}, \dot{d}_{sm1}^{aL})$ and $(\dot{d}_{sm1}^{aR}, \dot{d}_{sm1}^{aR})$ respectively belonging to N_L and N_R , from the vector of all the states for the sub-model $(\dot{d}_{sm1}, \dot{d}_{sm1})$. These selections are based on the value of the nut's position vector r_{Nut} at each instant.

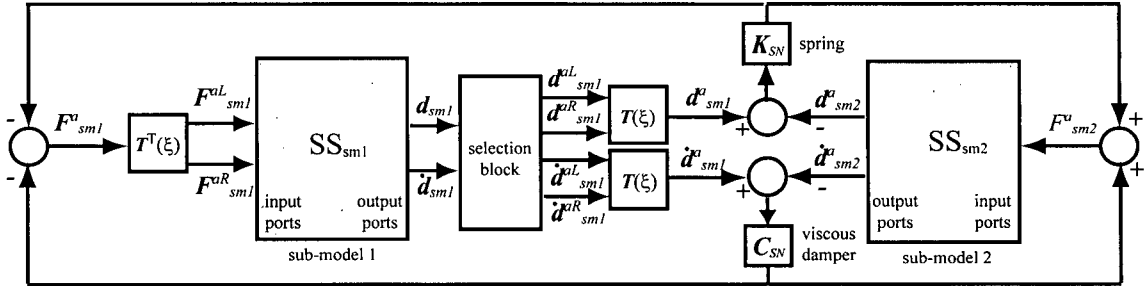


Figure 5.8: Incorporation of Position-Dependent Structural Dynamics Variations into Simulation Model

Given the information at the left and right nodes, the shape function matrix $T(\xi)$ introduced in Chapter Three as $T_{BS\xi-BSi}$, is used to transform the states belonging to the left and right nodes, to equivalent states, $(\dot{d}_{sm1}^a, \dot{d}_{sm1}^a)$ at the attachment point P_{Nut} . Similarly, the transpose of this matrix $T^T(\xi)$ is used to transform the reaction force vector, F_{sm1}^a from the joint, to the reaction force vectors, F_{sm1}^{aL} and F_{sm1}^{aR} at N_L and N_R , respectively.

Consequently, as the nut moves along the ballscrew, the position-dependent dynamic variations are captured in a smooth and efficient manner. Even though, by using a single screw-nut interface stiffness matrix K_{SN} , the Rigid-Ballscrew method is assumed to have been employed here, the same procedure can be applied, with minor modifications, when the shape-function-method-based interface stiffness matrices K_{SNi} , presented in Chapter Three, are used.

5.2.3 Model Reduction

5.2.3.1 Component Mode Synthesis

Finite element models usually consist of a large number of degrees-of-freedom (DOF). Generally, the number of DOF in the model determines the amount of dynamic information

that can be obtained from it. However, oftentimes, only a small amount of this dynamic information is useful for controller design and simulation purposes, while most of it is redundant. Model reduction therefore aims at eliminating as much of the unnecessary information as possible without unduly distorting the beneficial portion of the information.

One class of reduction methods that has proved efficient for multi-component structures like ballscrew drives is the Component Mode Synthesis (CMS) reduction techniques [46]. In the CMS methods, the DOF of the structure to be reduced are grouped into two categories – the interface/exterior DOF and the interior DOF. The exterior DOF are those DOF of the model which cannot be eliminated during the reduction process. They usually comprise the DOF at the interface of two connected structures, which bear reaction forces, and also the DOF to which actuation forces are applied. The interior DOF on the other hand, are typically those DOF to which no load is applied, hence making it possible to express them in terms of the exterior DOF using the Guyan Reduction Method [16].

When reducing ballscrew drive models, one of the greatest challenges faced is capturing the position-dependent dynamic variations. This is because the relative motion of one structure with respect to the other demands that the exterior DOF defined for the interface between these structures change from position to position. Consequently, standard flexible multi-body dynamic simulation software packages like ADAMS [32] are unable to handle systems like ballscrew drives because their methods are limited to structures with fixed interface points. For this reason, other researchers [46] have devised a means of handling this problem by retaining all the DOF of the so-called residual structures which are involved in relative motion (like the ballscrew) while reducing the other structures. However, this method has a significant drawback because retaining all the DOF of the residual structures greatly limits the amount of reduction that can be achieved. For instance, for the model presented in Chapter Three, more than 90 [%] of its DOF belong to the ballscrew. Therefore, retaining all the DOF of the ballscrew implies almost no reduction.

Consequently, in this section, CMS methods are applied in a novel way for ballscrew drives in order to enable the residual structures to also be reduced, while still allowing the position-dependent dynamic variations to be incorporated effectively into the reduced model using the method presented in the previous section.

5.2.3.2 Reduction Using Constraint Modes

Consider a structure which has E exterior DOF and I interior DOF. The structure is loaded at its exterior DOF by forces F_e , and also loaded at its interior DOF by forces F_i . Assuming, as is usually the case, that the system's damping matrix is obtained via the modal damping technique (see Appendix A), then the system can be analyzed as un-damped. The model's equation of motion in the partitioned form is thus given by,

$$\underbrace{\begin{bmatrix} M_{ee} & M_{ei} \\ M_{ie} & M_{ii} \end{bmatrix}}_{M_{model}} \underbrace{\begin{Bmatrix} \ddot{d}_e \\ \ddot{d}_i \end{Bmatrix}}_{\ddot{d}} + \underbrace{\begin{bmatrix} K_{ee} & K_{ei} \\ K_{ie} & K_{ii} \end{bmatrix}}_{K_{model}} \underbrace{\begin{Bmatrix} d_e \\ d_i \end{Bmatrix}}_d = \underbrace{\begin{Bmatrix} F_e \\ F_i \end{Bmatrix}}_F \quad (5.10)$$

where the subscripts e and i refer to exterior and interior DOF.

In order to reduce the system, a component mode set has to be chosen. One of the most commonly used sets consists of the complete set of exterior DOF d_e , augmented by a set of P fixed or free-interface normal (vibration) modal DOF of the structure, q_p [17]. For ballscrew drives, the set of free interface normal modes is usually preferred over the fixed ones [46]. Based on this component mode set selection, the coordinate transformation required for reduction is given by,

$$\begin{Bmatrix} d_e \\ d_i \end{Bmatrix} = \Psi \begin{Bmatrix} d_e \\ q_p \end{Bmatrix} \quad (5.11)$$

where the transformation matrix, Ψ is expressed as,

$$\Psi = \begin{bmatrix} I_{ee} & \mathbf{0}_{ep} \\ \varphi_{ie} & \chi_{ip} \end{bmatrix} \quad (5.12)$$

φ_{ie} are the constraint or static modes due to unit displacements at the exterior DOF. They are calculated [16] by assuming $F_i=0$ for the static equilibrium equations derived from Eq.(5.10). Hence, φ_{ie} is given by,

$$\varphi_{ie} = -K_{ii}^{-1} K_{ie} \quad (5.13)$$

χ_{ip} on the other hand, is a subset of the modeshape vector, χ , obtained from solving for the eigenvectors of Eq.(5.10), and selecting the first P non-rigid-body modes.

The reduced mass and stiffness matrices of the model are therefore obtained by pre-multiplying and post-multiplying the original ones by Ψ^T and Ψ , respectively, while the force vector, F is pre-multiplied by Ψ^T to get its reduced form. This results in an equation of motion for the reduced system given by,

$$\mathbf{M}_{model}^{red} \begin{Bmatrix} \ddot{\mathbf{d}}_e \\ \ddot{\mathbf{q}}_p \end{Bmatrix} + \mathbf{K}_{model}^{red} \begin{Bmatrix} \mathbf{d}_e \\ \mathbf{q}_p \end{Bmatrix} = \mathbf{F}^{red} \quad (5.14)$$

where the superscript 'red' indicates the reduced system which has $(I-P)$ DOF less than the original system $(I \gg P)$. The response of the full system can be recovered from the reduced system by using Eq.(5.11). This kind of recovery is called Modal Displacement (MD) recovery.

MD recovery gives a good approximation of the full system's response provided the condition that $F_i=0$ is satisfied. This is because the contribution of the truncated $(I-P)$ higher frequency modes is partly accounted for by the constraint modes which ensure that the static part of the solution is exact, with minimal errors in the dynamic part of the solution.

However, when some interior DOF are loaded, the MD recovery method gives rise to errors in both the static and dynamic part of the solution, particularly at the response of the interior DOF. This is the case for ballscrew drives because, as explained previously, the exterior DOF keep changing as the nut moves along the ballscrew. If only a few of these are selected as exterior DOF for the model, then when the nut moves, some interior DOF become loaded resulting in errors. One way of averting this problem is to change the exterior DOF as the nut moves, but this gives rise state-space sub-models which are position/time-dependent, and must be re-computed at every time step. Another way out is to retain all the DOF of structures like the ballscrew, which are involved in relative motion; but this gives rise to a poor reduction, as explained previously.

5.2.3.3 Response Recovery Using Modal Acceleration

Considering the shortcomings of the MD method when recovering the responses of structures with loads applied to their interior DOF, in this thesis the Modal Acceleration (MA) recovery method [15] is proposed as an effective way of obtaining the response of the

full system. This is because it introduces a static correction to the MD method which improves the accuracy of the recovered response.

In order to recover the responses from the reduced model, the equation of motion expressed in Eq.(5.10) can be split into two row partitions. The first is given by,

$$\begin{bmatrix} \mathbf{M}_{ee} & \mathbf{M}_{ei} \end{bmatrix} \begin{Bmatrix} \ddot{\mathbf{d}}_e \\ \ddot{\mathbf{d}}_i \end{Bmatrix} + \begin{bmatrix} \mathbf{K}_{ee} & \mathbf{K}_{ei} \end{bmatrix} \begin{Bmatrix} \mathbf{d}_e \\ \mathbf{d}_i \end{Bmatrix} = \mathbf{F}_e \quad (5.15)$$

Then from the second row partition, the displacements of the interior DOF, \mathbf{d}_i can be obtained as,

$$\mathbf{d}_i = \begin{bmatrix} -\mathbf{K}_{ii}^{-1} \mathbf{M}_{ie} & -\mathbf{K}_{ii}^{-1} \mathbf{M}_{ii} \end{bmatrix} \begin{Bmatrix} \ddot{\mathbf{d}}_e \\ \ddot{\mathbf{d}}_i \end{Bmatrix} - \mathbf{K}_{ii}^{-1} \mathbf{K}_{ie} \mathbf{d}_e + \mathbf{K}_{ii}^{-1} \mathbf{F}_i \quad (5.16)$$

This expression can be rewritten as,

$$\begin{Bmatrix} \mathbf{d}_e \\ \mathbf{d}_i \end{Bmatrix} = \begin{bmatrix} \mathbf{0}_{ee} & \mathbf{0}_{ei} \\ -\mathbf{K}_{ii}^{-1} \mathbf{M}_{ie} & -\mathbf{K}_{ii}^{-1} \mathbf{M}_{ii} \end{bmatrix} \begin{Bmatrix} \ddot{\mathbf{d}}_e \\ \ddot{\mathbf{d}}_i \end{Bmatrix} + \begin{bmatrix} \mathbf{I}_{ee} \\ -\mathbf{K}_{ii}^{-1} \mathbf{K}_{ie} \end{bmatrix} \mathbf{d}_e + \begin{bmatrix} \mathbf{0}_{ei} \\ \mathbf{K}_{ii}^{-1} \end{bmatrix} \mathbf{F}_i \quad (5.17)$$

By substituting Eq.(5.11) into Eq.(5.17), the MA recovery turns out to be,

$$\begin{Bmatrix} \mathbf{d}_e \\ \mathbf{d}_i \end{Bmatrix} = \underbrace{\begin{bmatrix} \mathbf{0}_{ee} & \mathbf{0}_{ep} \\ -\mathbf{K}_{ii}^{-1} (\mathbf{M}_{ie} + \mathbf{M}_{ii} \boldsymbol{\varphi}_{ie}) & -\mathbf{K}_{ii}^{-1} \mathbf{M}_{ii} \boldsymbol{\chi}_{ip} \end{bmatrix}}_{\mathbf{T}_1} \begin{Bmatrix} \ddot{\mathbf{d}}_e \\ \ddot{\mathbf{q}}_p \end{Bmatrix} + \underbrace{\begin{bmatrix} \mathbf{I}_{ee} \\ \boldsymbol{\varphi}_{ie} \end{bmatrix}}_{\mathbf{T}_2} \mathbf{d}_e + \underbrace{\begin{bmatrix} \mathbf{0}_{ei} \\ \mathbf{K}_{ii}^{-1} \end{bmatrix}}_{\mathbf{T}_3} \mathbf{F}_i \quad (5.18)$$

This method therefore explicitly includes a recovery matrix (\mathbf{T}_3) which corrects for the static effects of the forces applied to the interior DOF. Furthermore, using \mathbf{T}_2 it corrects for the static effects of inertia loads due to accelerations of the exterior DOF [15]. Consequently, for ballscrew drives, components like the ballscrew can be reduced with fixed exterior DOF, and then the static effects of the reaction forces and inertial loads can be added on by using the MA recovery.

Figure 5.9 shows how this is implemented for the full model shown in Figure 5.1. The reduced state-space model $\text{SS}_{\text{model}}^{\text{red}}$ is obtained by substituting the reduced mass matrix $\mathbf{M}_{\text{model}}^{\text{red}}$, reduced stiffness matrix $\mathbf{K}_{\text{model}}^{\text{red}}$ and reduced damping matrix ($\mathbf{C}_{\text{model}}^{\text{red}} = \boldsymbol{\Psi}^T \mathbf{C}_{\text{model}} \boldsymbol{\Psi}$) into Eq.(5.3).

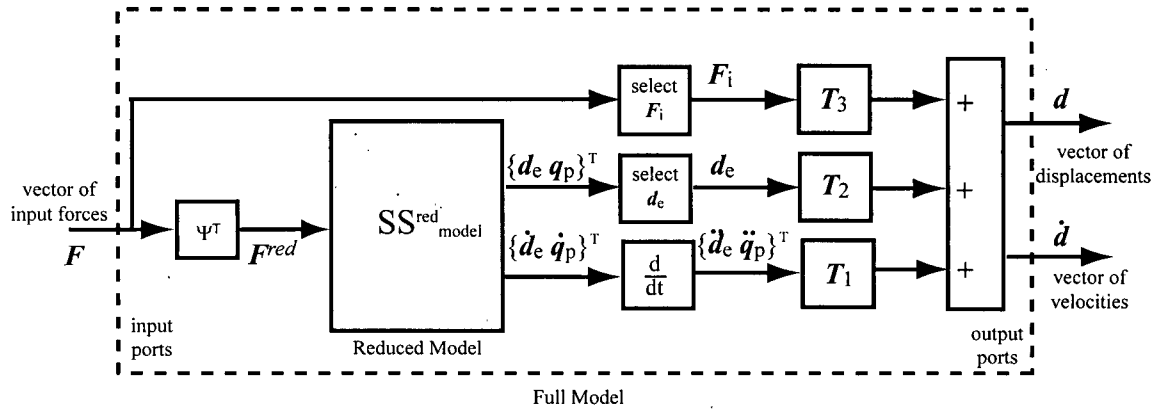


Figure 5.9: Implementation of CMS Reduction and MA Recovery Scheme

5.3 Sample Implementation of Simulation Model

In this section, a Simulink[®] model of the experimental test-bed described in Chapter Three is built based on the methodology presented in this chapter. First, the state-space model of the set-up is derived, and then non-linear dynamics are incorporated into it. In order to better understand the advantage of this model, the closeness of its acceleration response to that of the actual set-up is compared with the acceleration response of a similar model developed only considering rigid-body dynamics. Next, the model is reduced, and the effectiveness of the reduction scheme is weighed against the full model. Finally some controller and process dynamics are added on, and the whole system simulated for a given reference trajectory.

5.3.1 Interaction between Non-Linear and Higher Order Dynamics

The non-linearities considered for the set-up model are the guideway friction, screw-nut interface backlash and position-dependent dynamic variations. In order to incorporate them into the model, it is divided into two sub-models at the screw-nut interface. Furthermore, because the guideway is assumed to be rigid, the bending deflections of the system do not have any effects on the table dynamics. Consequently, all the DOF related to bending are considered redundant for this model and so have been deleted, leaving only the torsional and axial DOF. Table 5.1 gives a summary of the components and number of DOF in each of the sub-models.

Sub-Model	Constituent Components	Number of DOF
Sub-Model 1	ballscrew, thrust bearing, radial ball bearing, coupling, rotor	101
Sub-Model 2	table and nut	1

Table 5.1: Description of Sub-Models of Set-up

The joint connection between the two models is a reduced form of the screw-nut interface stiffness and damping matrices, having only the torsional and axial DOF. The state-space equation for each sub-model is generated using the method explained in Section 5.2.1. Subsequently, the guideway friction is applied to the table and nut (lumped together) in Sub-Model 2, based on the procedure outlined in Section 5.2.2.1, while the screw-nut interface backlash is applied to the torsional DOF of the joint between the two sub-models following the description in Section 5.2.2.2. Lastly, the variation of dynamics as the nut and table move along the ballscrew is introduced into the model as explained in Section 5.2.2.3. Table 5.2 gives a summary of the friction and backlash parameters for Eq.(5.7) and Eq.(5.9), measured experimentally from the set-up.

Parameter	Value
$F^{+/-}_{coul}$ [N]	± 2066
B [kg/s]	12673
L [rad]	0.001885

Table 5.2: Friction and Backlash Parameters for Set-up

Figure 5.10 shows the square-wave excitation signal applied to the motor in order to observe the motions of the table under the influence of the system non-linearities and higher-order dynamics. It has a frequency of 5 [Hz] and peak-to-peak amplitude of 4.25 [V].

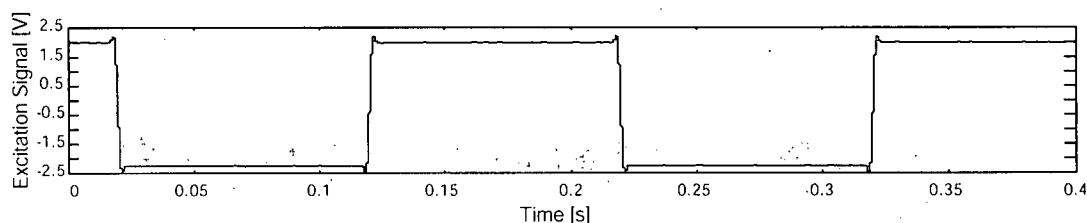


Figure 5.10: Excitation Signal Applied to Motor

A comparison of the responses of the table with and without backlash and guideway friction is shown in Figure 5.11. As seen, when the non-linearities are not considered, the excitation signal causes vibrations at 115 [Hz] which are noticeable at the table responses, particularly in the acceleration response. These vibrations are excited once at the beginning of each step, and then die down uniformly. They are mainly as a result of the axial mode of the ballscrew described in Section 4.4.1. However, with the addition of non-linearities, there is an extra excitation of the same mode in the middle of each step, resulting from the discontinuities of the backlash and friction forces. Furthermore, the backlash adds a varying time delay which can be observed in the acceleration signals. This is the time-delay that gives rise to the reversals and extra phase lag in the responses of the actual machine presented in Sections 3.5.2.2 and 3.5.2.4. Also, notice the enormous errors in the displacement response, resulting from the presence of coulomb friction.

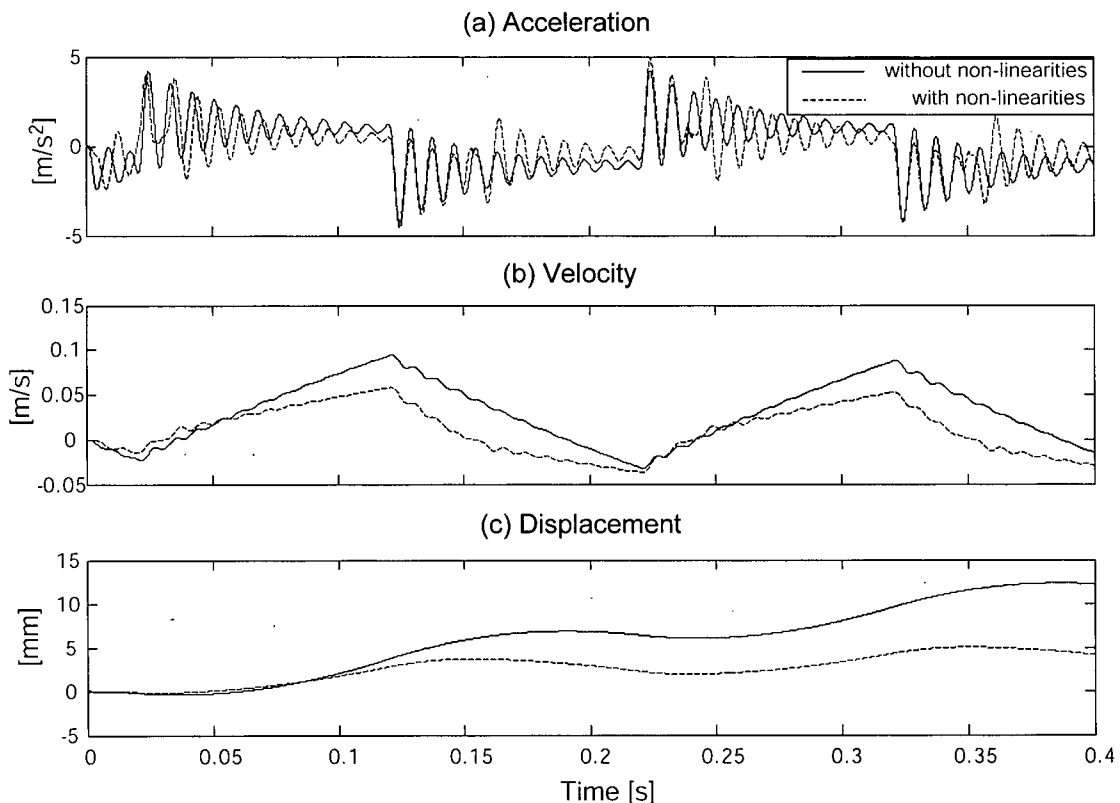


Figure 5.11: Simulated Responses of the Table with and without Non-linearities

The responses shown in Figure 5.11 are for the C-Position (i.e. when the table is at the centre of its travel length). Figure 5.12 shows a comparison of the responses measured at the R-Position (i.e. when the table is at the extreme right of its travel length), with those at the C-Position. Notice the increase in the frequency of the vibrations from 115 [Hz] at the C-Position, to 133 [Hz] at the R-Position. This is due to the position-dependent variation in the machine dynamics as the nut travels along the ballscrew.

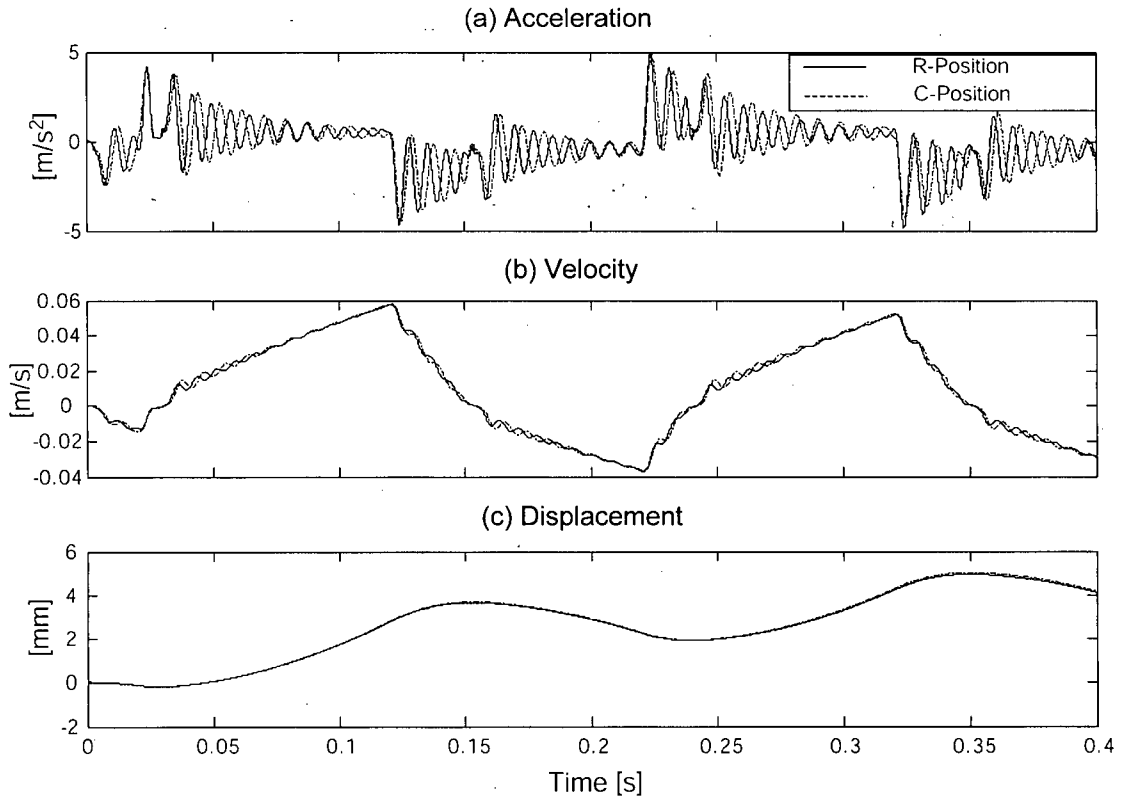


Figure 5.12: Simulated Responses of the Table Measured at the C and R-Positions

For the sake of comparison, the same excitation signals in Figure 5.10 are applied to a model generated only based on rigid-body dynamics. Furthermore, they are applied to the experimental test-bed and the acceleration of the table is measured using an accelerometer mounted on the table. Figure 5.13 shows these two responses, together with that obtained from the FE model at the C-Position. As seen, the rigid-body dynamics model cannot capture any of the vibrations, therefore highly underestimates the accelerations. The FE Model is able to capture some of the vibrations, and so is at least better able to predict the peak value.

The discrepancy between the frequency of the vibrations measured from the actual set-up and those from the model are as a result of the influence of other vibration modes which are not captured by the model. Modal tests on the set-up indicate the presence of two other modes at about 60 [Hz] and 160 [Hz], in addition to the one captured by the FE Model at about 120 [Hz]. The 60-Hz mode is believed to exist as a result of the interactions between the x-axis drive of the machine (which is used as the experimental set-up) and the y-axis drive upon which it is mounted. In order to capture this mode, the y-axis drive must also be modeled. On the other hand, the mode at 160 [Hz] is probably due to the influence of the fastened joint between the nut and table. Usually, this joint plays an important role in the dynamics measured at the table. However, it was excluded from the FE-Model for this set-up due to insufficient information about the stiffness of its fastened joint.

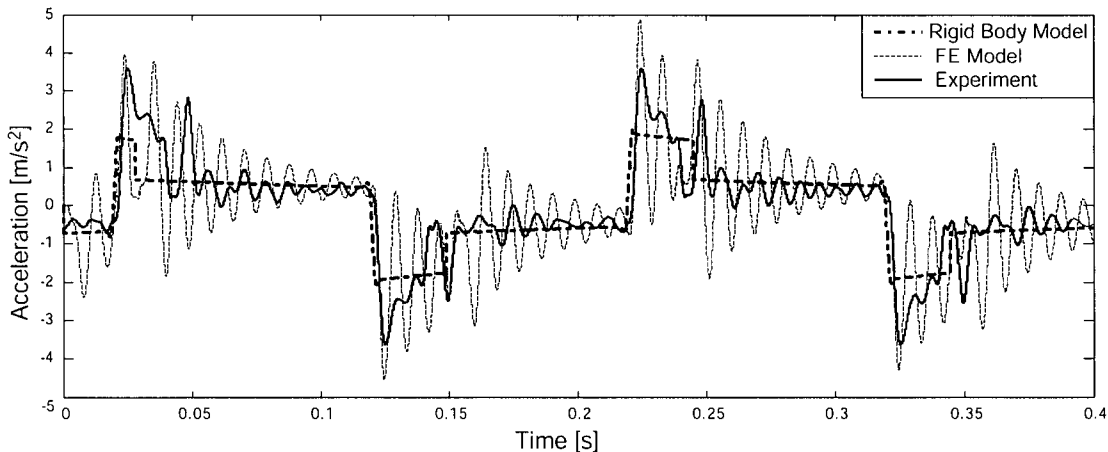


Figure 5.13: Comparison of the Rigid-Body and FE Models with Experiments

5.3.2 The Impact of Model Reduction

The model reduction scheme discussed in Section 5.2.3 is implemented on the simulation model for the set-up presented above, in order to get rid of the redundant information in the model, hence reduce the simulation time. Since the model is divided into two sub-models, the reduction has to be applied individually to the sub-models. Sub-model 2 has only 1 DOF hence it is totally meaningless to reduce it. On the other hand, Sub-model 1 has 101 DOF, most of which are coming from the ballscrew. Most of the redundant information resides in this sub-model, therefore it will be beneficial to reduce it.

For the reduction, two exterior DOF are considered ($E=2$). The first exterior DOF is the motor's DOF, which is chosen because the actuation torque is applied to it. As a second exterior DOF, a node at the centre of the ballscrew is chosen, to serve as an anchor point for the whole ballscrew which can receive forces on any of its nodes depending on the position of the nut. Furthermore, the first three free-interface normal modes of the sub-model are selected ($P=3$). Hence the number of DOF of the sub-model is reduces from 101 to 6 (i.e $E+P+1$ Rigid-Body Mode).

Table 5.3 gives a summary of the first four natural frequencies calculated based on the full sub-model, and those obtained from the reduced sub-model. The percentage errors in the natural frequencies of the reduced sub-model with respect to those of the full sub-model are also given. The results show that the maximum discrepancy in the frequencies is 0.8 [%], which is negligible. Therefore, the reduction does not significantly distort the natural frequencies. This is so because the number of ballscrew DOF chosen as exterior DOF is few.

Mode Number	Full Sub-Model's Natural Freq. [Hz]	Reduced Sub-Model's Natural Freq. [Hz]	Percentage Error
1	260.86	262.94	0.800
2	793.46	793.46	0.000
3	1276.40	1276.50	0.007

Table 5.3: Comparison of Natural Frequencies of the Full and Reduced Sub-Models

When this reduced model is used without the MA recovery, the slightest movement of the nut away from the anchor node chosen on the ballscrew leads to numerical instabilities due to the forces applied on the interior nodes. However, with the MA recovery, the correction factor takes care of the errors and the simulation remains stable irrespective of the position of the nut on the ballscrew.

In order to ascertain the impact of the reduction on the simulation time, and accuracy of the responses, the excitation signal shown in Figure 5.10 is applied to the reduced model and the responses of the table are obtained. The simulation on the full-model takes 635 [s] on a Pentium IV CPU (2.40 GHz) running Simulink[®], while on the reduced model, it takes 135

[s], representing a five fold reduction in simulation time. Figure 5.14 shows a comparison between the responses obtained from the two models, while Figure 5.15 shows a zoomed view of the boxed region of the response plots. It is obvious from the figures that the responses are approximately the same. The slight discrepancy which can be observed from the acceleration plot indicates the errors arising from the dynamic portion of the truncated modes which has not been compensated. However, the errors resulting from this are negligible for all practical purposes.

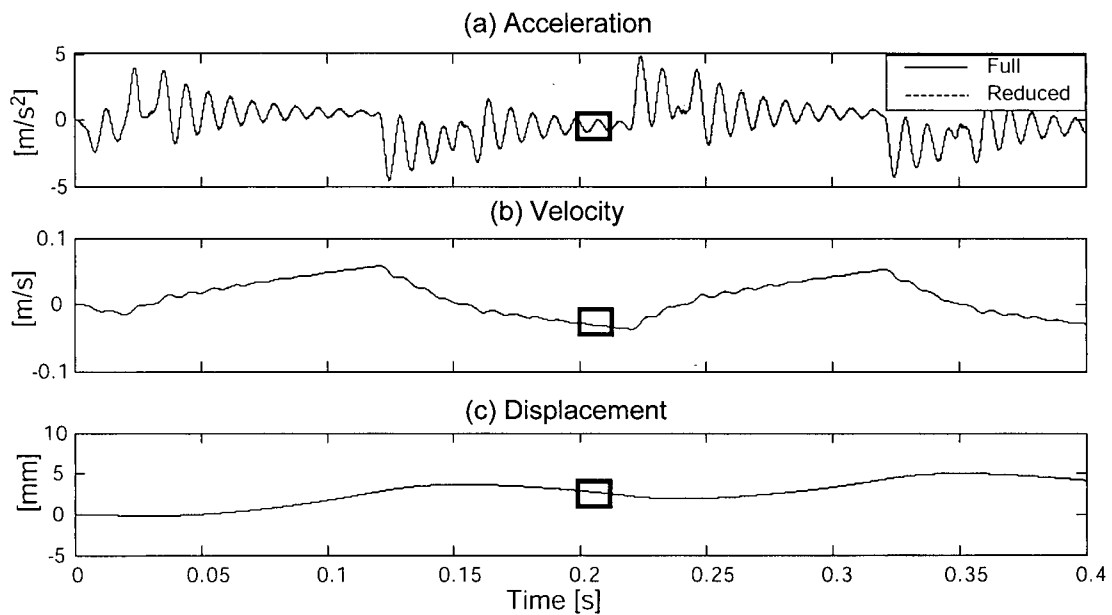


Figure 5.14: Comparison of the Simulated Responses from the Full and Reduced Models

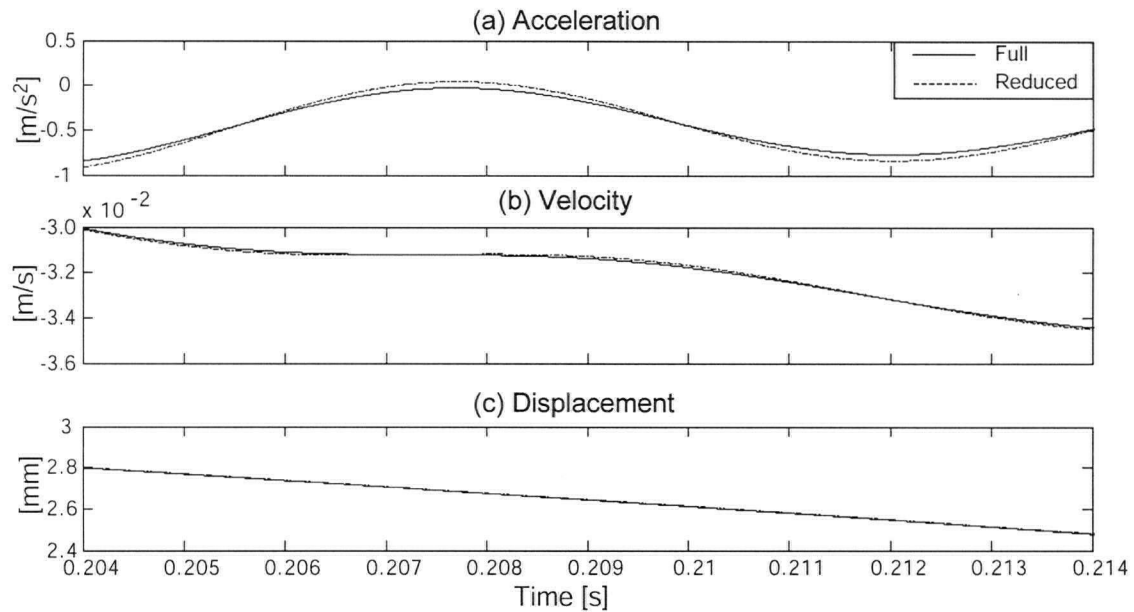


Figure 5.15: Zoomed View of the Simulated Responses from the Full and Reduced Models

5.3.3 Coupled Simulation of Controller, Process and Feed Drive Systems

In order to show how the simulation model presented here fits into the grand scheme of virtual simulation of machine tool feed drive systems (which could be extended to include the entire machine tool), the three controllers designed in Chapter Four are each used to perform a simple single-axis slotting operation. As shown in Figure 5.16, first the workpiece is fed rapidly at 40 [m/min] over a distance of 100 [mm] starting from the L-Position of the table. Then the slotting operation is performed at a feed rate of 25 [m/min]. Finally, the table is rapidly moved to the other end (R-Position) of its travel range, again using a 40-m/min feed rate.

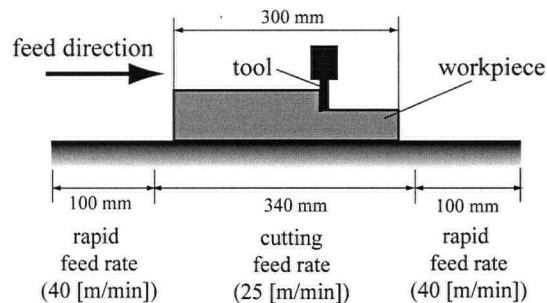


Figure 5.16: Slotting Operation

The reference trajectory for the toolpath, and the cutting force in the feed direction per spindle revolution ($T_{spindle}=0.0024$ [s]) are shown in Figure 5.17 and Figure 5.18, respectively. They are obtained using in-house developed software [8] based on the parameters given in Table 5.4 and Table 5.5, respectively.

Trajectory Type	Trapezoidal Velocity
Velocity Limit of Machine	60 [m/min]
Acceleration Limit of Machine	1.5 [G]
Deceleration Limit of Machine	1.5 [G]

Table 5.4: Parameters for Reference Trajectory Generation

Workpiece Material	Al 7075
Tool Type/Material	4-Fluted Helical Endmill/Carbide
Tool Diameter	20 [mm]
Tool Helix Angle	30 [deg]
Spindle Speed	25000 [rpm]
Depth of Cut	5 [mm]

Table 5.5: Parameters for Cutting Process Simulation

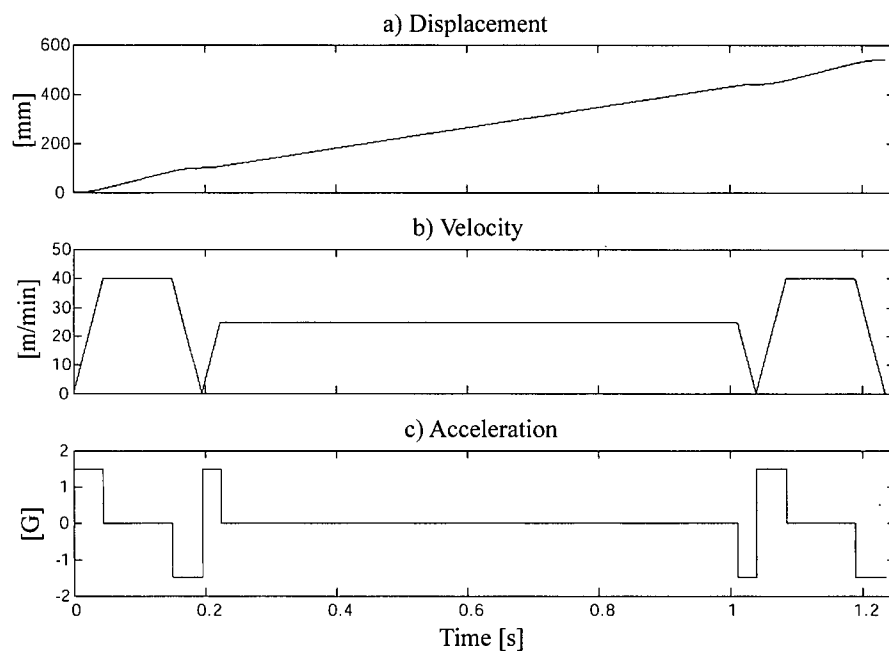


Figure 5.17: Reference Trajectories for Slotting Operation

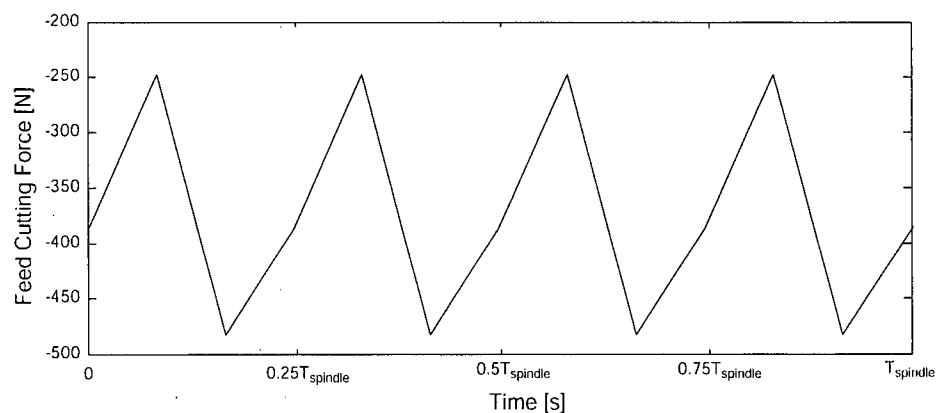


Figure 5.18: Feed Cutting Forces over One Spindle Revolution

The responses of the feed drive system controlled by the P-PI Controller designed based on rigid-body dynamics, re-designed P-PI Controller with a Notch Filter, and PPC, designed in Chapter Four, are shown in Figures 5.19, 5.20 and 5.21, respectively.

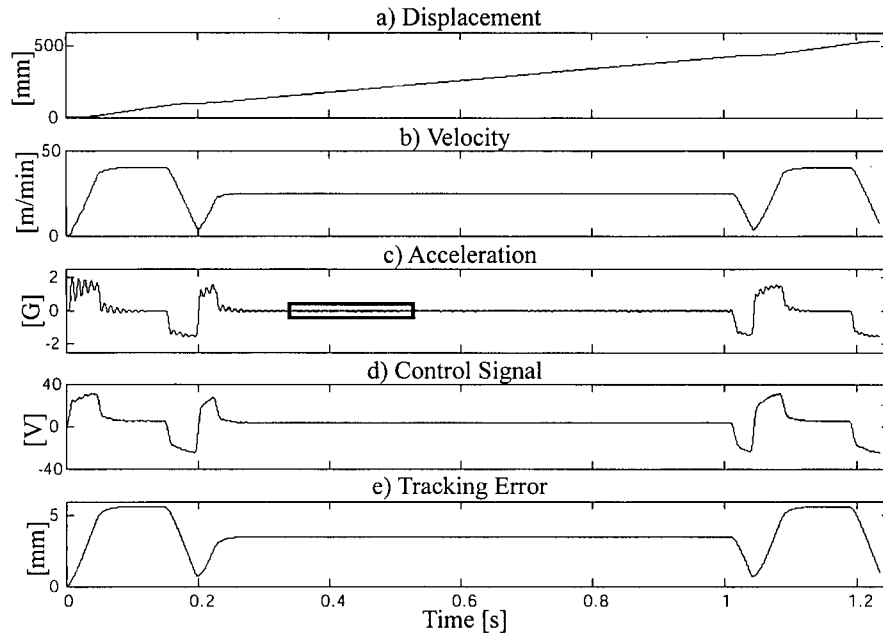


Figure 5.19: Simulated Responses of Feed Drive Controlled with Rigid-Body Based P-PI Controller

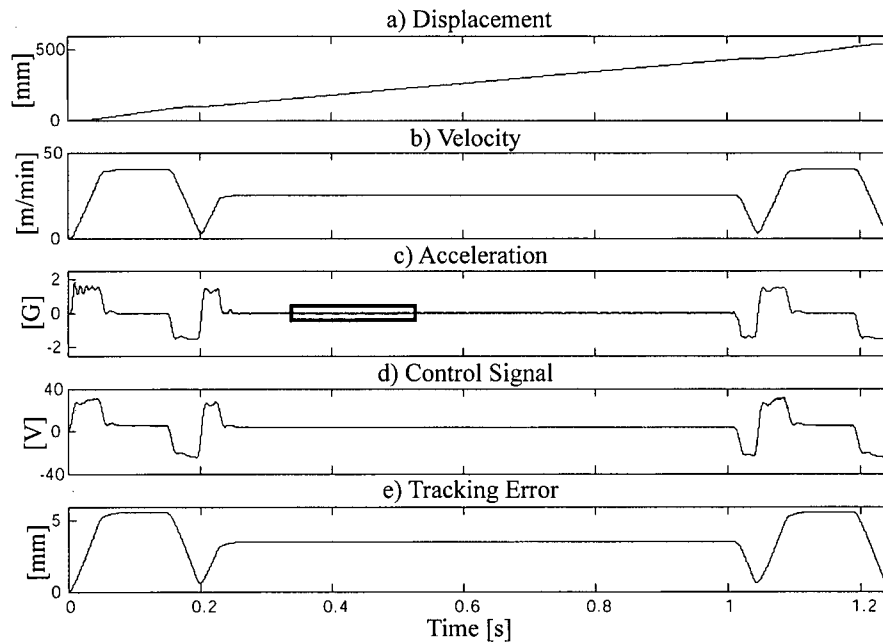


Figure 5.20: Simulated Responses of Feed Drive Controlled with P-PI+Notch Filter

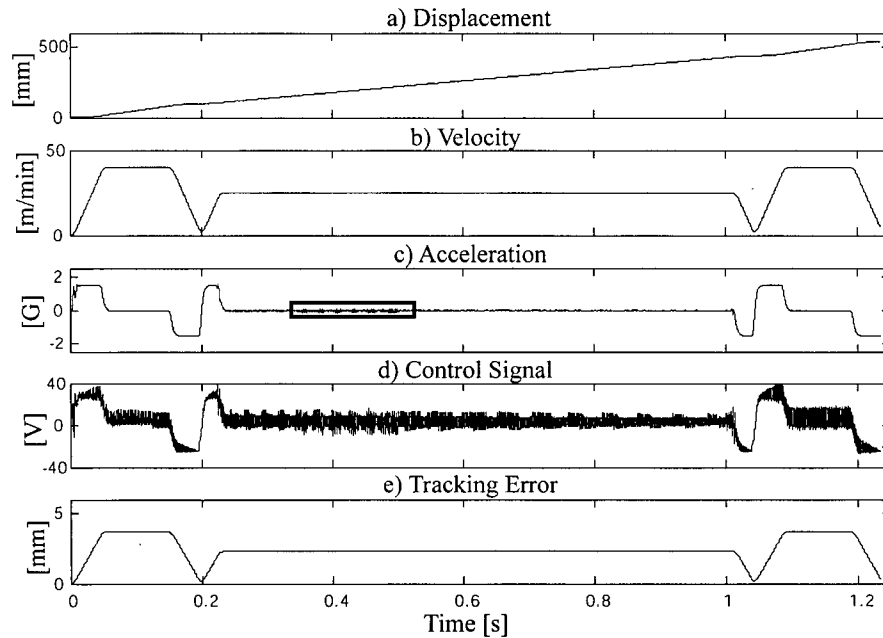


Figure 5.21: Simulated Responses of Feed Drive Controlled with PPC

From the figures, the performance characteristics of each of the controllers on the feed drive model can readily be observed. From the acceleration response of the rigid-body dynamics based P-PI controller (Figure 5.19(c)), the effect of the uncompensated mode of 112-140 [Hz] (depending on the position) can be seen as transient vibrations due to inertia forces. The amplitude of the vibrations is higher, around the L-Position, while it reduces significantly at the R-Position. This phenomenon is closely linked to the mode shape at that frequency range, which as explained in Section 4.4.1, is predominantly an axial mode of the ballscrew being stretched and compressed as the table moves. Since the axial stiffness of the ballscrew is inversely proportional to its length, at the L-Position, the effective distance between the nut and the thrust bearing attached to the ballscrew is maximum, therefore the stiffness is least, while at the R-Position, the distance is minimum, hence the stiffness maximum. This position-dependent change in stiffness is also the reason why the natural frequency, which is proportional to stiffness, is lowest at the L-Position and highest at the R-Position.

The addition of the notch filter, as observed from Figure 5.20(c), results in a significant attenuation of the vibrations. However, since the notch filter was designed for the C-Position, its effectiveness deteriorates a little at the L and R-Positions. In the case of this set-up, the

deterioration is not severe; however, in cases where the variation of dynamics from one position to the other is very large, the deterioration may lead to stability issues.

Comparing the tracking errors of the two controllers discussed above (Figures 5.19(e) and 5.20(e)), it can be concluded that the addition of the notch filter does not improve the tracking performance of the feed drive system. A maximum tracking error of 5.6 [mm] is recorded for both cases, during the rapid feed motion periods at the beginning and end of the operation.

The mode-compensating PPC outperforms the P-PI controllers both in terms of vibration suppression and tracking performance. It is able to successfully damp out the vibrations coming from the ballscrew's axial mode at all positions, while keeping the maximum tracking error below 4 [mm]. However, even with this improvement, the tracking error is still large, and so for high-precision machining, a controller which can further reduce the tracking errors must be resorted to. An Adaptive Sliding Mode Controller has been implemented in [13] to achieve both mode-compensation and high-precision tracking performance.

All three controllers show a similar trend in control signals. The maximum peak value of control signals (40 [V]) occurs when the PPC is used, while a maximum continuous value of 25 [V] is recorded for all three controllers. These values correspond to a peak torque and continuous torque requirement of 124 [Nm] and 78 [Nm], respectively from the drives. The set-up used here has not been designed for HSM purposes, hence its peak and continuous torque values are respectively 43 [Nm] and 8.5 [Nm]. However in high-speed machine tools, lighter mechanical components are employed together with powerful drives. Therefore, the torque requirements are significantly reduced, while the capabilities of the drives are increased to meet the demands of the high-performance controllers.

The control signals of the PPC are more oscillatory than those of the P-PI Controllers due to the fact that it acts aggressively to compensate for the vibrations coming from the ballscrew's axial mode. However, just as in the case of the P-PI+Notch Filter, the performance of this fixed-parameter PPC can not be guaranteed in the presence of huge changes in dynamics from position to position.

The effects of the disturbance forces applied to the feed drive's table during the slotting operation are highly attenuated due to the ballscrew's drive ratio. Furthermore, the presence

of integral action in all three controllers ensures that any static error that the 350 [N] negative offset in the cutting forces may introduce is eliminated. However, the alternating portion of the cutting force introduces a forced vibration at 1667 [Hz] (tooth-passing frequency) on the table, which can be seen by zooming into the boxed region of the acceleration responses of the three controllers as shown in Figure 5.22 (a), (b) and (c).

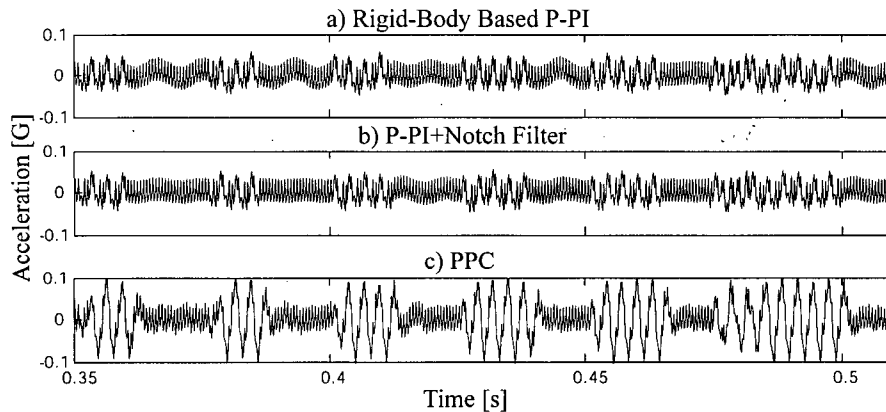


Figure 5.22: Comparison of Simulated Acceleration Responses of Feed Drive controlled by Various Controllers under Effects Cutting Force Disturbances

From Figure 5.22, it can be seen that apart from the forced vibrations at tooth-passing frequency, the cutting forces also excite a vibration at about 120 [Hz] (mainly due to the frequency of the axial mode of the ballscrew) in the acceleration response of the two P-PI controllers. However, in the response of PPC controller, the oscillation at 120 [Hz] is not noticeable. This is due to the ability of the PPC to introduce damping directly to the compensated mode, unlike the P-PI+Notch Filter. Furthermore, the figure shows that the cutting forces also intermittently excite some vibrations at about 333 [Hz]. These vibrations result from a combined effect of the ballscrew's axial mode at about 120 [Hz], and other modes of the ballscrew, for instance the coupling's torsional mode at about 560 [Hz]. The amplitude of these intermittent vibrations is smaller (0.05 [G]) for the P-PI controllers, but increases by about two folds for the PPC. This is because of the higher sensitivity of the PPC at high frequencies, when compared to the P-PI controllers (see Figure 4.24 (a)). Therefore, it is important that while trying to mitigate the effects of low-frequency modes, the high-

frequency ones are not unduly amplified, as in the case of the PPC, especially where the effects of disturbance forces at those high frequencies could be significant.

5.4 Summary

In this chapter, a simulation model for ballscrew drives based on equations of motions obtained from a linear FE model has been developed. The model is designed to incorporate some of the common non-linearities of a feed drive's mechanical system – backlash, coulomb and static friction, and position-dependent variation in structural dynamics. Furthermore, an existing response recovery method has been applied to ballscrew drives in a novel way in order to achieve a considerable reduction in simulation time, while still making it possible to capture the position dependent dynamics of the drive. Using a commercial simulator, the model has been used to simulate the interaction between feed drive structural dynamics, non-linearities, process dynamics and controller dynamics.

Chapter 6

Conclusions

6.1 Conclusions

A modeling scheme for Cartesian-configured high-speed machine tool ballscrew drives is presented in this thesis. This scheme enables the components of a ballscrew drive to be modeled using finite element techniques as lumped rigid-bodies or distributed parameter components. As a result, a hybrid finite element model of the feed drive is generated, which can be used for high-performance controller design and interactive simulation of the feed drive's performance during the design stage of the machine tool.

In modeling ballscrew drives, the mechanical components which are relatively more rigid are modeled as lumped rigid-bodies, while the ballscrew, which is relatively more flexible, is modeled using Timoshenko beam elements. The joint interfaces, including bearings, couplings and guideways, are modeled as linear and rotary springs in various directions. This results in a model which is able to capture the desired structural dynamics while maintaining a reasonably low order.

A significant contribution of this thesis is in the modeling of the screw-nut interface, where two methodologies for deriving the interface stiffness matrix are presented – the rigid-ballscrew and shape function methods. The rigid-ballscrew method gives rise to a single interface stiffness matrix which is experimentally proven to adequately predict the position-dependent structural dynamics variations that occur as the nut moves along the ballscrew. Furthermore, the matrix is seen to contain some additional cross-coupling terms which have not been derived by other researchers, and may play an important role in the dynamics of ballscrew drives, as shown by a preliminary simulation study. The shape function method has been derived in anticipation of situations where the rigid-ballscrew method may not work properly. However, it is yet to be validated experimentally.

The ballscrew drive model developed in this thesis is able to provide relevant dynamic information needed for controller design. Controllers designed based on the model are shown to outperform those designed based on the traditional techniques which do not consider the

structural dynamics of the drive. Furthermore, the model provides information which enables weak spots of the feed drive's mechanical design to be identified, and modifications made where possible in order to enhance its performance characteristics.

As part of the modeling scheme presented in this thesis, a simulation strategy is derived which permits some non-linear dynamics of the drive mechanism to be incorporated into time-domain simulations. The most peculiar non-linearity considered is the position-dependent structural dynamics variations which occur as the nut moves along the ballscrew. The simulation strategy allows for a smooth and efficient adjustment of the dynamics of the feed drive as the table position changes. This thesis makes a significant contribution in this respect by devising a means of efficiently achieving model reduction, while retaining the ability of the simulation scheme to capture these position-dependent dynamics. As a result, a significant amount of reduction in simulation time is achieved without unduly sacrificing the capabilities of the model. The simulation strategy also allows the controller dynamics and some other relevant dynamics of the feed drive system to be included in the time-domain simulations in order to realize a virtual prototype of the feed drive.

In summary, the modeling scheme presented in this thesis shows promising potentials towards providing a good description of the dynamics of Cartesian-configured ballscrew drives needed for controller design and performance simulation in the virtual environment. However, the full potential of the scheme could only be partially validated experimentally, due to a few limitations of the test-bed employed.

6.2 Future Research Directions

The modeling scheme presented in this thesis is applicable only to Cartesian-configured ballscrew drive systems where all the rigid-body motions are linear, since they consist of displacements along the Cartesian coordinates of the machine. However, it will be beneficial to extend the scheme to include non-Cartesian machine tools, like five-axis or parallel kinematic machine tools which are increasingly being used in the high-speed machining of dies and molds, aerospace parts, and other parts requiring complex three-dimensional motions. Since these machines exhibit large rotations, their kinematics is non-linear and coupled, thus giving rise to a more complex and time-dependent model.

Linear drives are increasingly being employed by machine tool builders, particularly for very high-speed machines with low thrust requirements. Therefore, the extension of this work to linear drives will pay great dividends.

A preliminary study has been conducted on the cross-coupling terms present in the screw-nut interface stiffness matrix derived in this thesis. This study shows interesting effects that the cross-coupling terms produce on the deformations of the table and ballscrew. It will be useful to conduct an experimental study in order to check if such effects are observable on an actual system, and if so, their relative significance.

Controller design, including the drive flexibilities and position-dependent dynamics, is another interesting dimension that can be added to this work. This will require developing control laws that will compensate for the changing structural dynamics of the feed drive as it moves from position to position. This research in controller design takes a more intriguing twist when applied to linear drives. Since the influence of the process dynamics on the controller performance is more profound when they are used. Therefore, the controller design will have to aim at actively preventing process induced instabilities like chatter vibrations, while trying to achieve high-positioning accuracy.

Bibliography

- [1] Allotta, B., Angioli, F., Rinchi, M., 2001, "Constraints Identification for Vibration Control of Time-Varying Boundary Conditions Systems", *Proceedings of the 2001 IEEE/ASME International Conference on Advanced Intelligent Mechatronics*, pp.606-611.
- [2] Armstrong, H.B., Dupont, P., and Canudas De Wit, C., 1994, "A Survey of Models, Analysis Tools and Compensation Methods for the Control of Machines with Friction," *Automatica*, Vol.30, No.7, pp.1083-1138.
- [3] Astrom, K.J., Wittenmark, B., 1997, *Computer-Controlled System*, Prentice Hall.
- [4] Berkermer, J., 2003, *Ph.D. Thesis: Gekoppelte Simulation von Maschinen-dynamik und Antriebsregelung unter Verwendung linearer Finite Elemente Modelle*, Universität Stuttgart, Institut für Statik und Dynamik der Luft-Und Raumfahrtkonstruktionen, Stuttgart.
- [5] Cannon, H.R., Schmitz E., 1984, "Initial Experiments on the End-Point Control of a Flexible One-Link Robot", *Int. J. Robot. Res.*, Vol.3, No.3, pp.62-75.
- [6] Cao Y., and Altintas, Y., 2004, "A General Method for the Modeling of Spindle-Bearing Systems," *ASME Journal of Mechanical Design*, Vol.126, pp.1089-1104.
- [7] Chen, Y., Tlustý, J., 1995, "Effect of Low-Friction Guideways and Lead-Screw Flexibility on Dynamics of High-Speed Machines", *Annals of CIRP*, Vol. 44, No. 1, pp. 353-356.
- [8] *Cut Pro® - Milling and Virtual CNC Modules*. Manufacturing Automation Laboratory, University of British Columbia.
- [9] Cuttino, J.F., Dow, T.A., 1997, "Contact Between Elastic Bodies with an Elliptic Contact Interface in Torsion", *ASME Journal of Applied Mechanics*, Vol.64, pp.144-148.
- [10] Cuttino, J.F., Dow, T.A., and Knight, B.F., 1997, "Analytical and Experimental Identification of Nonlinearities in a Single-Nut, Preloaded Ballscrew," *ASME Journal of Mechanical Design*, Vol.119, pp.15-19.
- [11] De Luca, A., Siciliano, B., 1993, "Regulation of Flexible Arms under Gravity", *IEEE Transactions on Robotics and Automation*, Vol.9, No.4, pp.463-476.
- [12] DeMul, J.M., Vree, J.M., and Mass, D.A., 1989, "Equilibrium and Association Load Distribution in Ball and Roller Bearings Loaded in Five Degrees of Freedom while Neglecting Friction, Part I: General Theory and Application to Ball Bearings", *ASME Journal of Tribology*, Vol.111, pp.142-148.
- [13] Erkorkmaz, K., 2003, *Ph.D. Thesis: Optimal Trajectory Generation and Precision Tracking Control for Multi-Axis Machines*, University of British Columbia, Department of Mechanical Engineering, Vancouver.

- [14] Erkorkmaz, K., and Altintas, Y., 2001, "High Speed CNC System Design: Part II – Modeling and Identification of Feed Drives," *International Journal of Machine Tools and Manufacture*, Vol.41, No.10, pp.1487-1509.
- [15] Fransen, S.H., 2004, "Data Recovery Methodologies for Reduced Dynamic Substructure Models with Internal Loads," *AIAA Journal*, Vol.42, No.10, pp.2130-2142.
- [16] Guyan, R.J., 1965, "Reduction of Stiffness and Mass Matrices," *AIAA Journal*, Vol.3, No.2, p.380.
- [17] Hintz, R.M., 1975, "Analytical Methods in Component Modal Synthesis," *AIAA Journal*, Vol.13, No.8, pp.1007-1016.
- [18] Holroyd, G., Pislaru, C., Ford, D.G., 2003, "Modelling the Dynamic Behaviour of a Ball-Screw System Taking into Account the Changing Position of the Ball-Screw Nut", *Proceedings of the 6th International Conf. LAMDAMAP 2003, Huddersfield, UK*, pp.337-348.
- [19] Hong, S.W., Shamine, D.M., and Shin, Y.C., 1999, "An In-Situ Identification Method for Joint Parameters in Mechanical Structures", *Journal of Vibration and Acoustics*, Vol.121, pp.363-372.
- [20] Hyde, J.M., Seering, W.P., 1991, "Using Input Command Pre-Shaping to Suppress Multiple Mode Vibration", *Proceedings of the IEEE International Conference on Robotics and Automation*, Vol.3, pp.2604-2609.
- [21] Jones, A.B., 1960, "A General Theory for Elastically Constrained Ball and Radial Roller Bearings Under Arbitrary Load and Speed Conditions", *ASME Journal of Basic Engineering*, pp.309-320.
- [22] Jones, S.D., Ulsoy, A.G., 1999 "An Approach to Control Input Shaping with Application to Coordinate Measuring Machines", *ASME Journal of Dynamic Systems, Measurement, and Control*, Vol.121, No.2, pp.242-247.
- [23] Jorgensen, B.R., and Shin, Y.C., 1998, "Dynamics of Spindle-Bearing Systems at High Speeds including Cutting Load Effects", *Journal of Manufacturing Science and Engineering, Transactions of the ASME*, Vol.120, No.2, pp.387-394.
- [24] Kraus, J., Blech, J., and Braun, S.G., 1987, "Insitu Determination of Rolling Bearing Stiffness and Damping by Modal Analysis", *Journal of Vibration, Acoustics, Stress, and Reliability in Design, Transactions of the ASME*, Vol.109, pp.235-240.
- [25] Kuo, C.B., 1987, *Automatic Control Systems*, Prentice Hall.
- [26] Lanari, L., Wen, J.T., 1992, "Asymptotically Stable Set Point Control Laws for Flexible Robots", *Systems and Control Lett.*, Vol. 19, pp.119-129.
- [27] Lee, H.G., Arimoto, S., Miyazaki, F., 1988, "Lypunov Stability Analysis for PDS Control of Flexible Multilink Manipulators", in *Proc. 27th IEEE Conf. Decision Contr.*, Austin TX, pp.75-80.

- [28] Lee, K., Ibaraki, S., Matsubara, A., Kakino, Y., Suzuki, Y., Arai, S., Braasch, J., 2002, "A Servo Parameter Tuning Method for High-Speed NC Machine Tools based on Contouring Error Measurement", *Laser Metrology and Machine Performance VI*, WIT Press, Southampton, UK.
- [29] Lim, H., Seo, J., Choi, C., 2000, "Position Control of XY Table in CNC Machining Center with Non-rigid Ballscrew", *Proceedings of the 2000 American Control Conference*, Chicago, pp.1542-1546.
- [30] Lim, T.C., and Singh, R., 1990, "Vibration Transmission Through Rolling Element Bearings, Part I: Bearing Stiffness Formulation", *Journal of Sound and Vibration*, Vol.139, No.2, pp.201-225.
- [31] Lin, M.C., Ravani, B., Velinsky, S.A., 1994, "Kinematics of the Ball Screw Mechanism", *ASME Journal of Mechanical Design*, Vol. 116, pp.849-855.
- [32] *MSC.ADAMS 2004*. MSC.Software Corporation, Santa Ana, California.
- [33] NSK Ltd, 2003, *Precision Machine Components*, NSK Catalog No. E3161.
- [34] Palmgren, A., 1959, *Ball and Roller Bearing Engineering*, S. H. Burbank.
- [35] Pislaru, C., Ford, D.G., Holroyd, G., 2004, "Hybrid Modelling and Simulation of a Computer Numerical Control Machine Tool Feed Drive", *Proceedings of the Institution of Mechanical Engineers*, Vol.218, Part I: J. Systems and Control Engineering, pp.111-120.
- [36] Pritschow, G., Rock, S., 2004, "'Hardware in the Loop' Simulation of Machine Tools", *CIRP Annals*, Vol.53, No.1, p.295.
- [37] Przemieniecki, J.S., 1968, *Theory of Matrix Structural Analysis*, McGraw-Hill, New York.
- [38] Reinhart, G., Weissenberger, M., 1999, "Multibody Simulation of Machine Tools as Mechatronic Systems for Optimization of Motion Dynamics in the Design Process", *Proceedings of the 1999 IEEE/ASME International Conference on Advanced Intelligent Mechatronics*, pp.605-610.
- [39] Rivin, E., 1999, *Stiffness and Damping in Mechanical Design*, Marcel Dekker, Inc.
- [40] Schafers, E., Hamann, J., Trondle, H., 2001, "Mechatronic Optimization, Analysis and Simulation of Machines", *Presentation given at the SPS/IPC/Drives 2001 Exhibition*, Siemens AG, A&D MCE.
- [41] Shigley, J.E., Mischke, C.R., and Budynas, R.G., 2004, *Mechanical Engineering Design*, McGraw Hill.
- [42] Smith, A.D., 1999, *Ph.D. Thesis: Wide Bandwidth Control of High-Speed Milling Machine Feed Drives*, University of Florida, Department of Mechanical Engineering, Florida.
- [43] Smith, M.H., Annaswamy, A.M., Slocum, A.H., 1995, "Adaptive Control Strategies for a Precision Machine Tool Axis", *Precision Engineering*, Vol.17, pp.192-206.

- [44] *SpindlePro*®. Manufacturing Automation Laboratory, University of British Columbia.
- [45] Symens, W., Van Brussel, H., Swevers, J., 2004, "Gain-Scheduling Control of Machine Tools with Varying Structural Flexibility", *CIRP Annals*, Vol.53, No.1, p.321.
- [46] Van Brussel, H., Sas, P., Istvan, N., De Fonseca, P., and Van den Braembussche, P., 2001, "Towards a Mechatronic Compiler," *IEEE/ASME Transactions on Mechatronics*, Vol.6, No.1, pp.90-105.
- [47] Varanasi, K., 2002, *M.Sc. Thesis: On the Design of a Precision Machine for Closed-Loop Performance*, Massachusetts Institute of Technology, Cambridge, MA.
- [48] Wei, C.C., Lin, J.F., 2003, "Kinematic Analysis of the Ball Screw Mechanism Considering Variable Contact Angles and Elastic Deformations", *ASME Journal of Mechanical Design*, Vol.125, pp.717-733.
- [49] Yeung, C., 2004, *M.A.Sc. Thesis: A Three-Axis Virtual CNC System*, University of British Columbia, Vancouver.
- [50] Yokoyama, T., 1990, "Vibrations of a Hanging Timoshenko Beam Under Gravity", *Journal of Sound and Vibration*, Vol.141, No.2, pp.245-258.
- [51] Zaeh, M.F., Oertli, T., Milberg, J., 2004, "Finite Element Modelling of Ball Screw Feed Drive Systems", *CIRP Annals*, Vol.53, No.1, p.289.

Appendix A

Beam Element, Current-Frame Rotation and Modal Damping Formulations

A.1 Beam Element Formulations

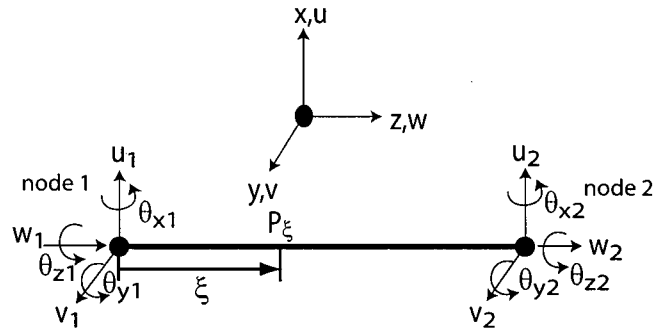


Figure A.1: Timoshenko Beam Element

Figure A.1 shows a two-noded Timoshenko beam element of length L_{Elm} . u , v and w indicate the displacements in the radial x , radial y and axial directions, while θ_x , θ_y and θ_z represent the rotations around the x , y and z (torsional) axes, respectively. The subscripts 1 and 2 respectively denote displacements and/or rotations belonging to node 1 and node 2. ξ is the non-dimensional position of the point P_ξ , measured from node 1. It assumes a minimum value of 0 when P_ξ is located at node 1, and a maximum value of 1 when it is located at node 2.

The stiffness and mass matrices [37,50] of the Timoshenko beam element, \mathbf{K}_{Elm} and \mathbf{M}_{Elm} , are given respectively in Eq.(A.1) and (A.2).

$$\begin{aligned}
m_1^i &= \frac{13 + \frac{7}{10}\Phi_j + \frac{1}{3}\Phi_j^2 + \frac{6}{5}(r_{Elm,i}^G/L_{Elm})^2}{(1+\Phi_j)^2}; & m_2 &= \frac{1}{3} \\
m_3^i &= \frac{\left(\frac{11}{210} + \frac{11}{120}\Phi_j + \frac{1}{24}\Phi_j^2 + \left(\frac{1}{10} - \frac{1}{2}\Phi_j\right)(r_{Elm,i}^G/L_{Elm})^2\right)L_{Elm}}{(1+\Phi_j)^2} \\
m_4 &= \frac{I_{Elm,zz}}{3A_{Elm}} \\
m_5^i &= \frac{\left(\frac{1}{105} + \frac{1}{60}\Phi_j + \frac{1}{120}\Phi_j^2 + \left(\frac{2}{15} + \frac{1}{6}\Phi_j + \frac{1}{3}\Phi_j^2\right)(r_{Elm,i}^G/L_{Elm})^2\right)L_{Elm}^2}{(1+\Phi_j)^2} \\
m_6^i &= \frac{\left(\frac{1}{140} + \frac{1}{60}\Phi_j + \frac{1}{120}\Phi_j^2 + \left(\frac{1}{30} + \frac{1}{6}\Phi_j + \frac{1}{6}\Phi_j^2\right)(r_{Elm,i}^G/L_{Elm})^2\right)L_{Elm}^2}{(1+\Phi_j)^2} \\
m_7 &= \frac{1}{6}; & m_8 &= \frac{I_{Elm,zz}}{6A_{Elm}} \\
m_9^i &= \frac{9 + \frac{3}{10}\Phi_j + \frac{1}{6}\Phi_j^2 + \frac{6}{5}(r_{Elm,i}^G/L_{Elm})^2}{(1+\Phi_j)^2} \\
m_{10}^i &= \frac{\left(\frac{13}{420} + \frac{3}{40}\Phi_j + \frac{1}{24}\Phi_j^2 + \left(\frac{1}{10} - \frac{1}{2}\Phi_j\right)(r_{Elm,i}^G/L_{Elm})^2\right)L_{Elm}}{(1+\Phi_j)^2}
\end{aligned} \tag{A.4}$$

$I_{Elm,ii}$ in the equations indicates the second moment of area of the element's cross section, while A_{Elm} is the cross sectional area of the element. The subscripts or superscripts, i and j are used to indicate the axis to which a parameter belongs (i.e. x or y axis). If i represents the x-axis, then j represents the y-axis, and vice versa. $I_{Elm,zz}$ is the polar second moment of area of the cross section. E , G and ρ , respectively represent the Young's modulus, shear modulus and density of the element. $r_{Elm,i}^G$ is the radius of gyration for the cross section, expressed as,

$$r_{Elm,i}^G = \sqrt{\frac{I_{Elm,ii}}{A_{Elm}}} \tag{A.5}$$

And Φ_j is a constant given by,

$$\Phi_j = \frac{12EI_{Elm,ii}}{k_i^s GA_{Elm} L_{Elm}^2} \quad (A.6)$$

k_i^s is the cross section factor, which takes a value of 9/10 for circular cross sections.

The Shape Function matrix ($T_{BS\xi-BSi}$) which is used to obtain the values of the displacements u_ξ , v_ξ and w_ξ , and rotations, $\theta_{x\xi}$, $\theta_{y\xi}$ and $\theta_{z\xi}$ at the point P_ξ from their values at node 1 and node 2 is given in Eq.(3.27)

The interpolation functions making up the elements of the shape function matrix are all functions of ξ . Their expressions are given in Eq.(A.7).

$$\begin{aligned} N_{uj1} &= \frac{1}{1+\Phi_j} \left(2\xi^3 - 3\xi^2 - \Phi_j \xi + (1+\Phi_j) \right) \\ N_{uj2} &= \frac{L_{Elm}}{1+\Phi_j} \left(\xi^3 - \left(2 + \frac{\Phi_j}{2} \right) \xi^2 + \left(1 + \frac{\Phi_j}{2} \right) \xi \right) \\ N_{uj3} &= -\frac{1}{1+\Phi_j} \left(2\xi^3 - 3\xi^2 - \Phi_j \xi \right) \\ N_{uj4} &= \frac{L_{Elm}}{1+\Phi_j} \left(\xi^3 - \left(1 - \frac{\Phi_j}{2} \right) \xi^2 - \frac{\Phi_j}{2} \xi \right) \\ N_{\theta j1} &= \frac{6}{(1+\Phi_j)L_{Elm}} (\xi^2 - \xi) \\ N_{\theta j2} &= \frac{1}{1+\Phi_j} \left(3\xi^2 - (4+\Phi_j)\xi + (1+\Phi_j) \right) \\ N_{\theta j3} &= -\frac{6}{(1+\Phi_j)L_{Elm}} (\xi^2 - \xi) \\ N_{\theta j3} &= N_{\theta j3} = \frac{1}{1+\Phi_j} \left(3\xi^2 - (2-\Phi_j)\xi \right) \\ N_{z1} &= N_{\theta z1} = 1 - \xi \\ N_{z2} &= N_{\theta z2} = \xi \end{aligned} \quad (A.7)$$

Just as in the previous case, the subscript j represents either the x or y-axis.

A.2 Current-Frame Rotation Formulations

The rotation matrix operators used to perform a rotation of a specified angle, θ around the x, y, or z axis of a Cartesian coordinate system are respectively denoted by $Rot_x(\theta)$, $Rot_y(\theta)$ and $Rot_z(\theta)$. Their expressions are given as,

$$\begin{aligned}
 Rot_x(\theta) &= \begin{bmatrix} 1 & 0 & 0 \\ 0 & \cos \theta & -\sin \theta \\ 0 & \sin \theta & \cos \theta \end{bmatrix} \\
 Rot_y(\theta) &= \begin{bmatrix} \cos \theta & 0 & \sin \theta \\ 0 & 1 & 0 \\ -\sin \theta & 0 & \cos \theta \end{bmatrix} \\
 Rot_z(\theta) &= \begin{bmatrix} \cos \theta & -\sin \theta & 0 \\ \sin \theta & \cos \theta & 0 \\ 0 & 0 & 1 \end{bmatrix}
 \end{aligned} \tag{A.8}$$

A current-frame rotation operation is one performed such that each subsequent rotation is based on the new coordinate system resulting from the preceding rotations. For instance, a rotation from a coordinate system (CS_1) to another coordinate system (CS_2) could involve a rotation of α about the x-axis of CS_1 , then another rotation of β about the y-axis of the new intermediate coordinate system resulting from the x-axis rotation. Then the rotation operation from CS_1 to CS_2 , T_{1-2} , can be represented by,

$$T_{1-2} = Rot_x(\alpha) \cdot Rot_y(\beta) \tag{A.9}$$

Generally, a rotation operation involving a sequence of current frame rotations from one coordinate system to another is performed by multiplying the respective rotation matrices in the same sequence as the rotations.

Another important fact about rotation operations is that a rotation matrix, T_{1-2} from an arbitrary coordinate system CS_1 to another CS_2 also represents a transformation matrix from CS_2 to CS_1 . In other words, a vector expressed in CS_2 can be transformed to CS_1 by pre-multiplying it by T_{1-2} .

A.3 Modal Damping Formulations

In order to obtain the damping matrix C_{model} for the second-order differential equation of the model in Eq.(3.44), first the un-damped homogenous equation, expressed as,

$$\mathbf{M}_{model}\ddot{\mathbf{d}} + \mathbf{K}_{model}\mathbf{d} = \mathbf{0} \quad (\text{A.10})$$

has to be solved in order to obtain the vector of eigen-values Λ , matrix of mode shapes (eigen-vectors) \mathbf{P} .

The natural frequencies, $(\omega_n)_k$ of the model are obtained by taking the square root of each of the elements, Λ_k of Λ , as,

$$(\omega_n)_k = \sqrt{\Lambda_k} \quad (\text{A.11})$$

while the k^{th} mode shape of the model, \mathbf{P}_k is extracted from the k^{th} column of \mathbf{P} .

The diagonal modal mass matrix, \mathbf{M}_q is obtained as from \mathbf{M}_{model} and \mathbf{P} as,

$$\mathbf{M}_q = \mathbf{P}^T \mathbf{M}_{model} \mathbf{P} \quad (\text{A.12})$$

This modal mass for the k^{th} mode, $(m_q)_k$ is obtained from the k^{th} element on the diagonal of \mathbf{M}_q . The mass-normalized mode shape matrix for the model, χ can be obtained from \mathbf{M}_q and \mathbf{P} as,

$$\chi = \mathbf{P} \mathbf{M}_q^{-1} \quad (\text{A.13})$$

Given the experimental/empirical modal damping ratios, ζ_k for each mode, each element, $(c_q)_k$ of the diagonal modal damping matrix, \mathbf{C}_q can be calculated from the corresponding natural frequency as,

$$(c_q)_k = 2\zeta_k (\omega_n)_k \quad (\text{A.14})$$

To calculate \mathbf{C}_{model} , \mathbf{C}_q is transformed using the mass-normalized mode shape matrix as,

$$\mathbf{C}_{model} = \chi^{-T} \mathbf{C}_q \chi^{-1} \quad (\text{A.15})$$

Appendix B

Determination of Parameters of Experimental Test-Bed

B.1 Ballscrew

The Figure B.1 shows a pictorial representation of the FE Model of the experimental test-bed's ballscrew. The measured dimensions of the ballscrew are summarized in Table B.1



Figure B.1: Pictorial Representation of FE Model of Ballscrew

Section	I.D [mm]	O.D [mm]	Length [mm]	No. of Elements
A	0.0	23.0	24.5	1
B	12.0	25.0	18.0	1
C	12.0	35.5	780	39
D	12.0	31.8	38.0	2
E	0.0	20.0	30.0	2
F	0.0	20.0	30.0	2

Table B.1: Dimensions of Ballscrew Sections

The O.D given for Section C, which represents the threaded sections, is the root diameter of the section. As explained in Section 3.3.1 of Chapter 3, the equivalent diameter used for the mass matrix obtained as 37.35 [mm]. The pitch, p , of the ballscrew is 10 [mm].

The ballscrew is assumed to be made of steel. Consequently, it has a density, $\rho = 7800$ [kg/m³], a Modulus of Elasticity, $E = 210$ [GPa], and a Poisson's ratio, $\nu = 0.27$.

B.2 Nut

The nut on the experimental test-bed and is shown in the figure below. Its mass is measured as, $m_{nut} = 1.49$ [kg]. In order to estimate its inertial properties, it is assumed to consist of two hollow cylinders as shown in Figure B.2. The flats on the flange, bolt holes and return tubes are not considered in the calculations. Based on this assumption, its inertia properties are approximated as $I_{xx,nut} = I_{yy,nut} = 2.56 \times 10^{-3}$ [kgm²], $I_{zz,nut} = 1.31 \times 10^{-3}$ [kgm²].

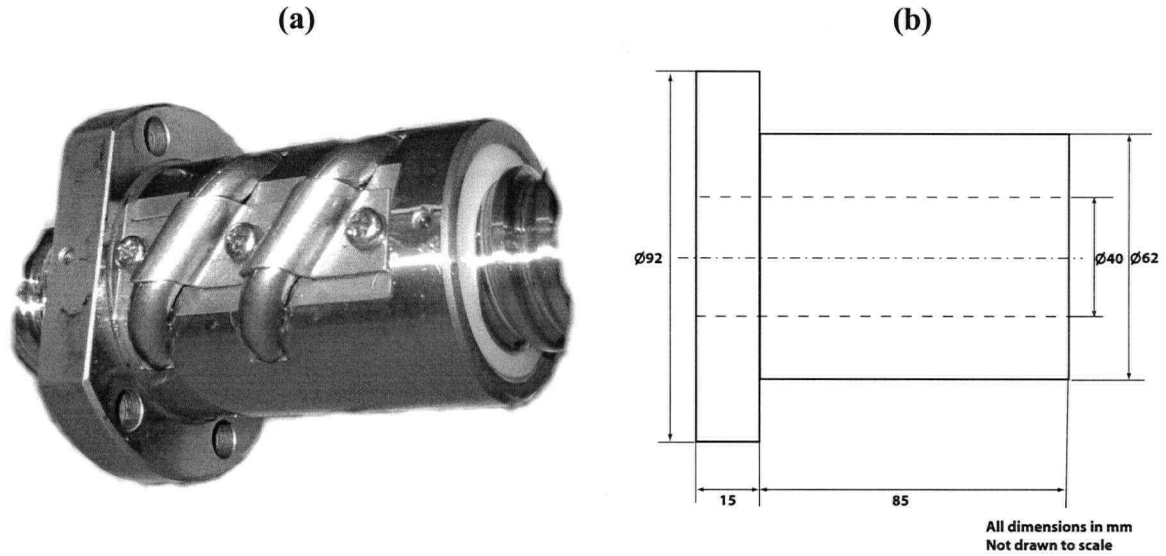


Figure B.2: Nut and Hollow-Cylinder Approximation for Calculating Its Inertias

B.3 Rotor and Table

The inertia for the test-bed's rotor is indicated in the motor's manufacturer's catalog as $I_{zz,rotor} = 5.98 \times 10^{-3}$ [kgm²].

The mass of the table, which is too cumbersome to weigh, is estimated from its CAD solid model shown in Figure B.3. It is assumed to be made of steel having a density of 7800 [kg/m³]. Its mass is calculated as $m_{table} = 250$ [kg].

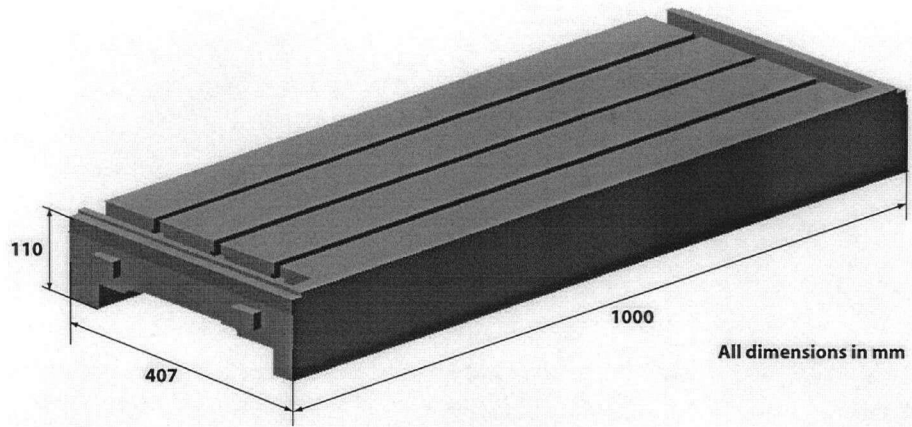


Figure B.3: Test-Bed's Table

B.4 Coupling

The coupling employed between the motor shaft and the ballscrew is the jaw-type coupling shown in Figure B.4. It consists of two jaws and a polyurethane insert. As explained in Section 3.3.3.1, the jaws can be modeled as lumped inertias while the insert is modeled as a torsional spring (see Figure 3.7).

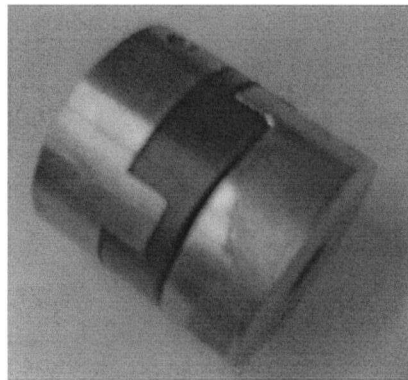


Figure B.4: Jaw-Type Coupling Between Motor Shaft and Ballscrew

For this coupling, the insert's torsional stiffness, k_T has not been provided by its manufacturers; therefore it has to be measured. The inertia of the jaws are obtained from their simple geometry and measured mass as, $J_1 = 3.09 \times 10^{-4}$ [kgm²] and $J_2 = 3.06 \times 10^{-4}$ [kgm²].

In order to measure the insert stiffness, a method based on FRF measurements has been devised. In this method, the 2-DOF model of the coupling shown in Figure 3.7 is used. A

simple modal analysis on the model gives analytical expressions for its two natural frequencies as,

$$f_{n1} = 0; \quad f_{n2} = \frac{1}{2\pi} \sqrt{\frac{k_T(J_1 + J_2)}{J_1 J_2}} \quad (\text{B.1})$$

Since the inertias J_1 and J_2 are already known, and the 2nd natural frequency, f_{n2} can be measured; k_T can easily be extracted from this expression.

For the coupling set shown above, the natural frequency f_{n2} is extracted from its FRF measured in the torsional direction between a point on J_1 and a point on J_2 as shown in Figure B.5. This value is $f_{n2} = 805$ [Hz].

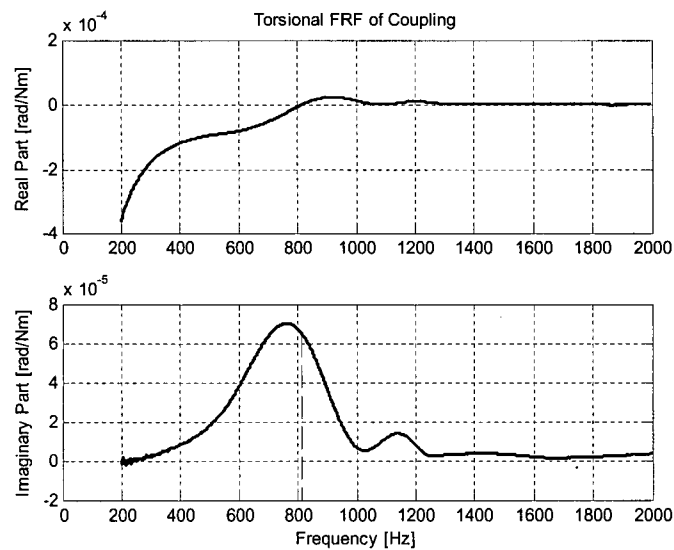


Figure B.5: Torsional FRF between a Point on J_1 to a Point on J_2

By substituting this value into Eq.(B.1), the insert's torsional stiffness is obtained as, $k_T = 3938$ [Nm/rad].

B.5 Bearings

At the end of the ballscrew proximal to the motor, two pairs of angular-contact bearings (NSK 7304B) are used to provide radial and axial support for the ballscrew, while on the end distal to the motor, a deep-groove ball bearing (SKF 6205-2RS1) is used to provide radial support. Their stiffness values have not been provided by the manufacturers.

In order to obtain the stiffness of these bearings, the model shown in Figure B.6, consisting of a rigid housing and rigid shaft connected by an angular contact bearing has been designed in SpindlePro[®] [44]. SpindlePro is a software developed in the Manufacturing Automation Laboratory at the University of British Columbia. It uses non-linear FE methods to calculate angular-contact bearing stiffness given the material, geometric and preload force properties of the bearing. The same model can be used for radial ball bearings by changing the ball-contact angle to zero.

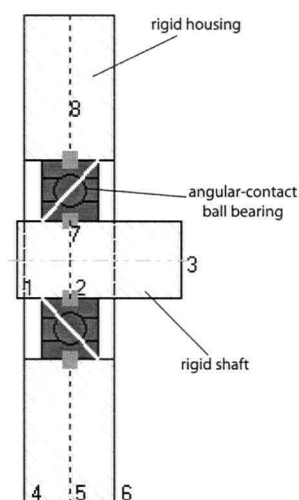


Figure B.6: Model of Angular-Contact Bearing generated using SpindlePro[®]

Table B.2 gives a summary of the parameters entered into the software for both bearings.

Parameter	Angular-Contact Bearing	Deep-Groove Bearing
Inner Diameter [mm]	20.00	25.00
Outer Diameter [mm]	52.00	52.00
Ball Diameter [mm]	9.40	7.94
Number of Balls	11	9
Ball Contact Angle [degrees]	40.00	0.00

Table B.2: Parameters used in SpindlePro[®] Bearing Models

For both bearings, the balls, inner rings and outer rings are assumed to be made of steel. Therefore, their material properties are the same as those used for the ballscrew in Section B.1.

The preload value on the angular-contact bearing is assumed to be about 700 [N] which corresponds to a medium-high preload as indicated in the manufacturer's catalogs for similar bearings. For this value, the axial stiffness is 1.35×10^8 [N/m] and the radial stiffness is 9.5×10^7 [N/m]. These values are doubled to obtain the stiffness for the test-bed because two similar angular-contact bearings are used together, probably in the back-to-back configuration, for greater rigidity. Hence, the stiffness values for the test-bed are $k_{B1ax} = 2.70 \times 10^8$ [N/m] and $k_{B1rad} = 1.9 \times 10^8$ [N/m], for the axial and radial directions, respectively.

On the deep-groove ball bearing, no nominal preload is applied since it is assumed to be floating. However, there is usually a considerable amount of friction between the bearing's outer ring and the housing. Hence, a little amount of preload is applied by this friction force. The preload value is assumed to be about 2 [N] for this set-up, resulting in a radial stiffness, k_{B2rad} of 4×10^7 [N/m].

B.6 Screw-Nut Interface

The preload type used in the test-bed's screw-nut interface is the oversize-ball preload. Apart from this, the only information available about the nut are, its measured length, $L_{nut} = 100$ [mm], its pitch, $p = 10$ [mm], its nominal radius, $R_{nut} = 20$ [mm] and the radius of its balls, $R_{ball} = 3.175$ [mm].

In order to obtain the interface stiffness matrix K_{SN} , as explained in Section 3.3.4, the number of balls in contact N_{Ball} , pitch angle, α , thread angle, β , ball stiffness, k_{Ball} , and the starting and ending azimuth angles for each ball are needed.

Considering the amount of unknown information and also the relatively short length of the nut, the rigid-ballscrew method is employed. It is assumed that the entire region within the interface is occupied by balls. The location of the screw and nut node, P is assumed to be at the centre of the nut. Hence, the starting and ending azimuth angle for each ball is calculated as,

$$\phi_{k,st} = -\frac{L_{nut}}{2p} 2\pi; \quad \phi_{k,end} = \frac{L_{nut}}{2p} 2\pi \quad (B.2)$$

In order words, the balls are assumed to start from the left end of the nut and move up to the right end.

N_{Ball} is calculated as,

$$N_{Ball} = \frac{s}{4R_{Ball}} \quad (B.3)$$

where s is the arc length of the helix formed by the path traveled by each ball. It is given by,

$$s = \left(\sqrt{R_{nut}^2 + r_g^2} \right) \cdot (\phi_{k,end} - \phi_{k,st}) \quad (B.4)$$

s is divided by $4R_{Ball}$ (Eq.(B.3)) representing twice the diameter of a ball, because in the oversize-ball preload mechanism, only one in every two balls is in contact. The other ball serves as a so-called spacer-ball. r_g in Eq.(B.4) is the ballscrew's gear reduction ratio given by Eq.(3.13).

α is calculated using Eq.(3.6) while β is measured approximately from the thread profile.

The ball stiffness k_{Ball} is estimated from the axial stiffness of the nut, as explained in Section 3.3.4.5. However, since the axial stiffness is also unknown, it is measured experimentally from FRF measurements. In order to do this, first, the free-free FE model of the ballscrew is developed, as explained in Section B.1. The mass of the nut, m_{nut} is then connected to it at a particular location using an axial spring k_{Ax} , whose stiffness is unknown. In order words, the nut is assumed to have a single stiffness in the axial direction. On the other hand, the FRF of the actual ballscrew with the nut at the same specified direction is measured. Then, iteratively, the stiffness k_{Ax} is adjusted until a good match is obtained between the FE model and actual model. This value is taken as the approximate axial stiffness of the nut.

The parameters estimated for the nut, based on the explanations above are summarized in Table B.3.

Parameter	α [°]	β [°]	$\phi_{k,st}$ [°]	$\phi_{k,end}$ [°]	N_{Ball}	k_{Ball} [N/ μ m]
Value	4.55	50	-1800	1800	100	20.7

Table B.3: Parameters used to Obtain Interface Stiffness Matrix for Test-Bed

Appendix C

Simulation Study on Cross-Coupling Terms of Screw-Nut Interface Stiffness Matrix

C.1 Purpose of Study

This study aims at investigating the effects the cross-coupling terms in the screw-nut interface stiffness matrix formulations presented in Chapter Three on the dynamics of a ballscrew drive axis. In particular, it tries to show how, as a result of these cross-coupling terms, the bending modes of the ballscrew give rise to displacements at the table which could affect its positioning accuracy. Furthermore, it shows how they give rise to complex mode shapes involving a combination of axial/torsional and bending deformations. This study is entirely based on simulations, and therefore is preliminary to a more detailed study including experiments.

C.2 Description of Simulation Test Set-up

The set-up used for this study is basically the same as the one described in Section 3.5.1, except for two modifications. Firstly, the table and nut are assumed to be lumped into a single rigid body having a simple geometry as shown in Figure C.1. This is done in order to simplify the calculation of moments of inertia. Secondly, the rigid-guideway assumption made in Chapter Three is relaxed, and the set-up is furnished with roller slides at its four corners (Figure C.1). The values for the inertia properties of the table, and stiffness values of the roller slides are summarized in Table C.1.

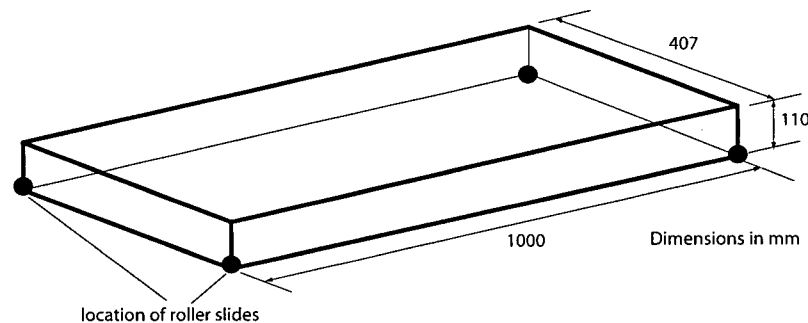


Figure C.1: Simplified Rigid-Body Model of Table and Nut

Parameter	Value
Roller Slide's Vertical Stiffness ($K_{x,gw}$) [$N/\mu m$]	500
Roller Slide's Lateral Stiffness ($K_{y,gw}$) [$N/\mu m$]	400
Mass of Table (m_{table}) [kg]	250
Moments of Inertia of Table ($I_{xx,table}, I_{yy,table}, I_{zz,table}$) [kgm^2]	24.2, 21.0, 3.7

Table C.1: Inertia Properties of Table and Stiffness Properties of Guideway

C.3 Effects of Cross-Coupling between the Bending Deformations

In order to show the effects of the cross-coupling terms, the natural frequencies and mode shapes of the set-up for selected modes are examined for two different cases. In Case A, the screw-nut interface matrix containing only the cross-coupling terms between the axial and torsional DOF (Eq.(3.46)) is considered, while in Case B, the screw-nut interface matrix containing the cross-coupling terms between axial, torsional and bending DOF (Eq.(3.45)) is employed on the set-up.

Figures C.2 and C.3 respectively show the 9th mode shape of the set-up for the Case A and Case B. This mode occurs at about 659 [Hz] in both cases.

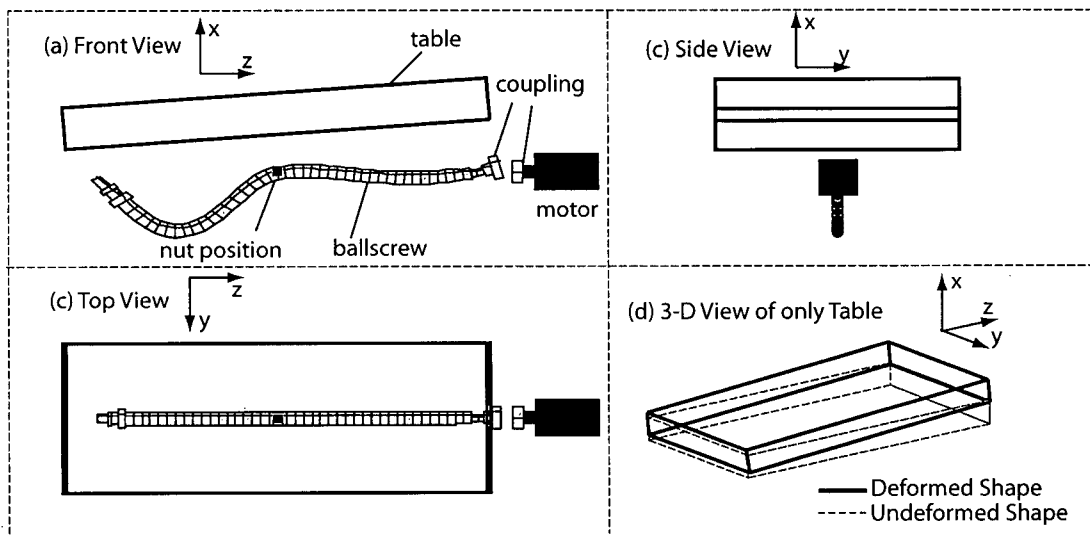


Figure C.2: 9th Mode Shape of Set-up for Case A at 659 [Hz]

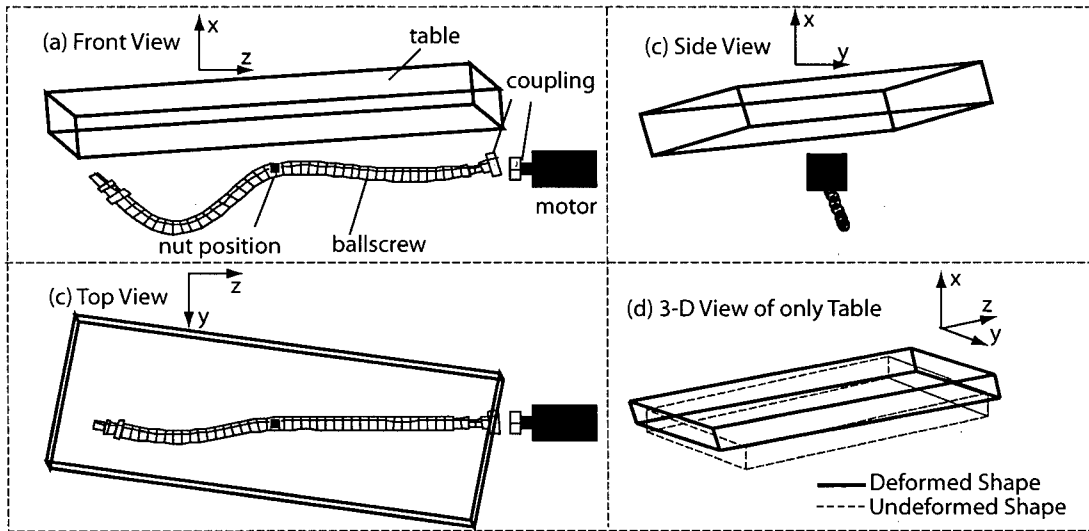


Figure C.3: 9th Mode Shape of Set-up for Case B at 659 [Hz]

As seen from the figures, in Case A (Figure C.2), the bending of the ballscrew occurs only in the x - z plane, giving rise to a pitching motion of the table. However, in Case B (Figure C.3), the cross-coupling terms between the x and y bending directions ($k_{\theta_{x,x}}$, $k_{\theta_{y,y}}$) force the ballscrew to also bend in the y - z plane. As a result, the table undergoes both a pitching and a yawing motion. These motions give rise to large displacements in the x , y and z directions, especially at the corners of the table. Such displacements can significantly affect the positioning accuracy of the table.

C.4 Effects of Cross-Coupling between the Axial/Torsion and Bending Deformations

The magnitude of the cross-coupling terms highly depends on the pitch of the ballscrew. Figure C.4 shows the variation of $k_{\theta_{x,x}}$, $k_{\theta_{y,y}}$, $k_{\theta_{x,z}}$, $k_{\theta_{x,\theta z}}$, expressed in terms of $k_{Ball} = 20.7$ [N/ μ m], with the ballscrew's pitch in [mm]. The figure shows that all four cross-coupling terms oscillate in value as the pitch changes. $k_{\theta_{x,x}}$ and $k_{\theta_{y,y}}$ alternate in peak value, such that when $k_{\theta_{x,x}}$ has a high value, $k_{\theta_{y,y}}$ is at a low value, and vice versa. The same trend is observed between $k_{\theta_{x,z}}$ and $k_{\theta_{x,\theta z}}$. Interestingly, the peak amplitude of $k_{\theta_{x,\theta z}}$ grows drastically as the pitch increases. From the figure, the maximum value of $k_{\theta_{x,\theta z}}$ occurs at a pitch of about 45 [mm]. Here, it takes on a value of $4.5 \times 10^{-4} \cdot k_{Ball}$, as opposed to its value of $1.65 \times 10^{-5} \cdot k_{Ball}$ at a pitch of 10 [mm]. The effect of this increase can be seen in Figures C.5 to C.8 showing the 19th mode of the set-up for Case A and Case B, at a pitch of 10 [mm] and 45 [mm].

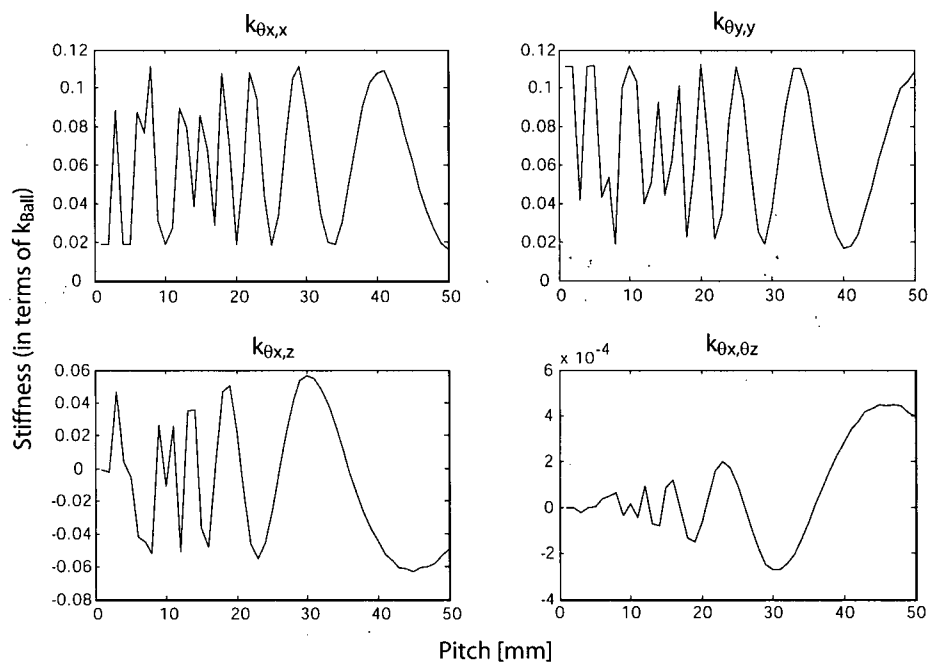


Figure C.4: Variation of Cross-Coupling Terms with Ballscrew's Pitch

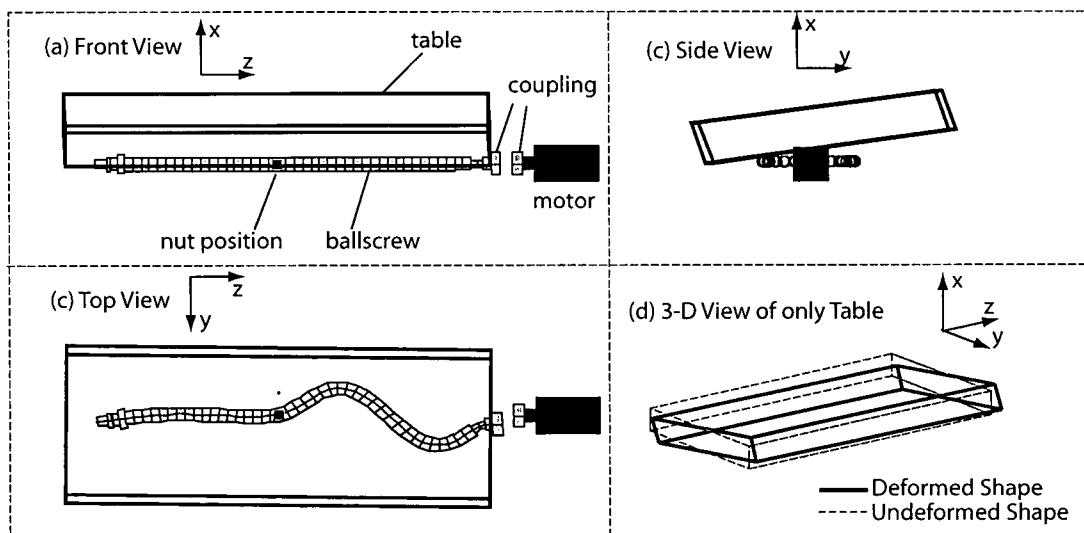


Figure C.5: 19th Mode Shape of Set-up for Case A at 1470 [Hz]; pitch = 10 [mm]

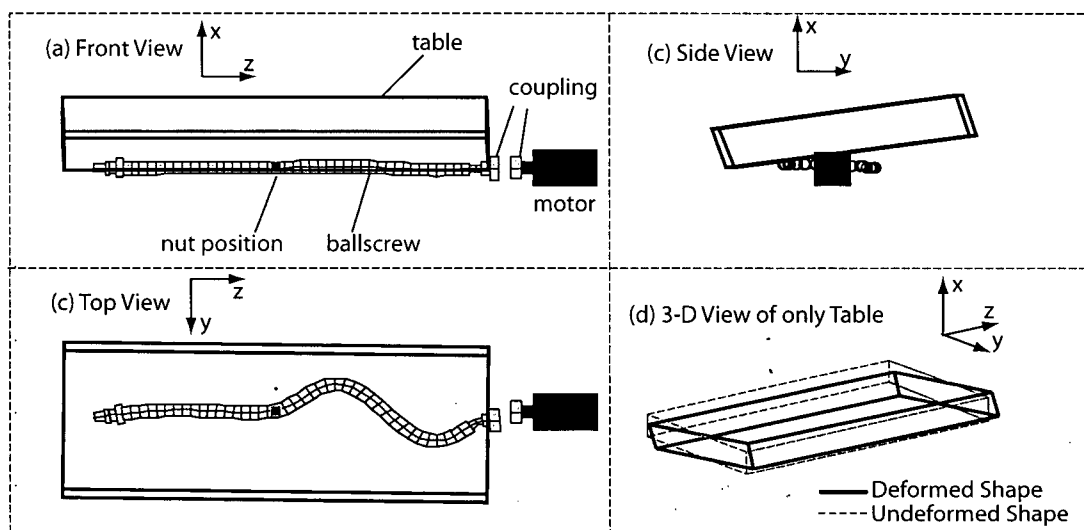


Figure C.6: 19th Mode Shape of Set-up for Case B at 1470 [Hz]; pitch = 10 [mm]

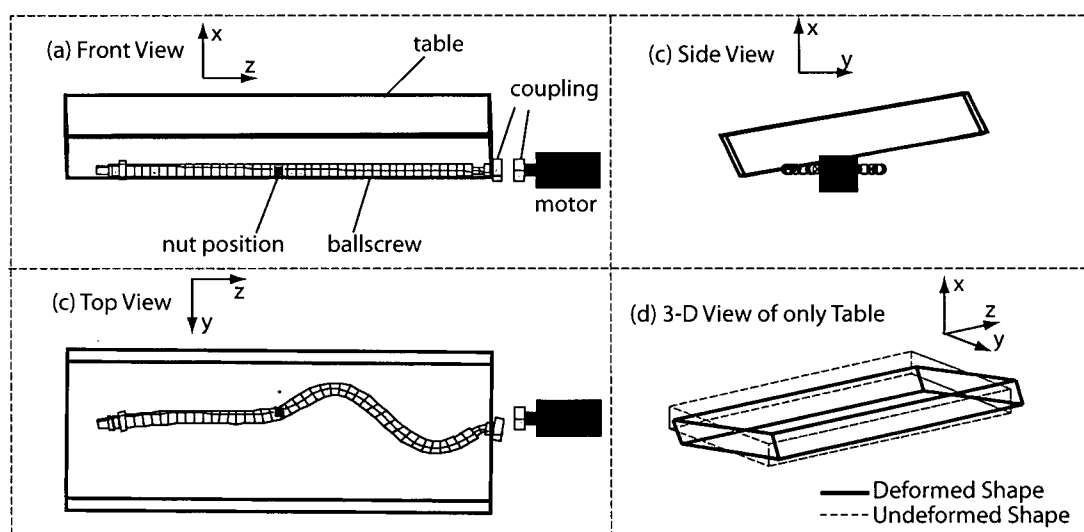


Figure C.7: 19th Mode Shape of Set-up for Case A at 1385 [Hz]; pitch = 45 [mm]

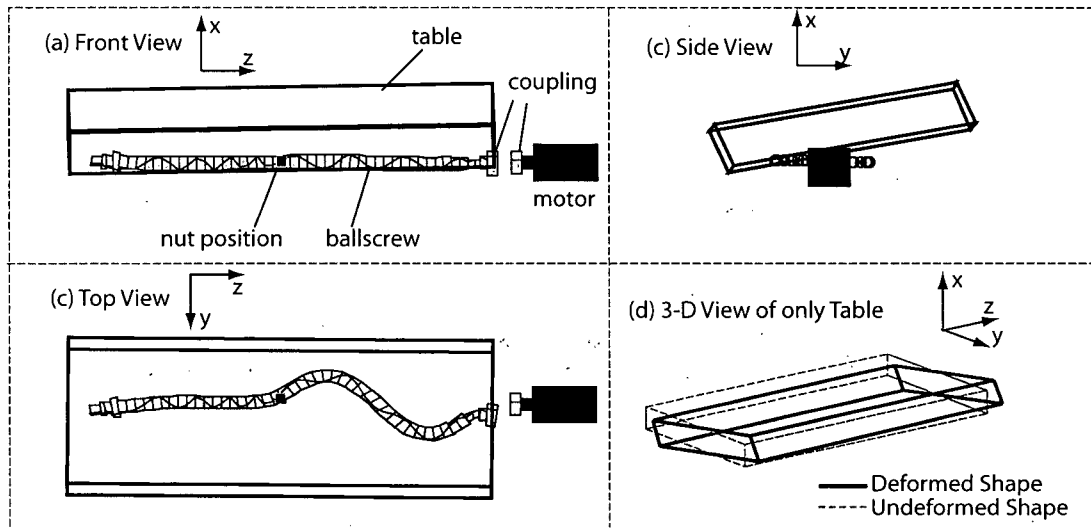


Figure C.8: 19th Mode Shape of Set-up for Case B at 1382 [Hz]; pitch = 45 [mm]

Figure C.5 shows that with a pitch of 10 [mm], in Case A, the ballscrew deforms in the y - z plane, leading to rolling and yawing motions of the table at 1470 [Hz]. The mode shape for the Case B (Figure C.6) having the same pitch is quite similar. The only difference here is that the ballscrew undergoes slight bending deformations in the x - y plane. Neither the table's motion nor the frequency of vibrations is affected significantly by this extra deformation.

In Figure C.7, it is observed that the increase of pitch angle from 10 to 45 [mm] leads to decrease in natural frequency from 1470 to 1385 [Hz], for Case A. At the same time, the rolling motion of the table is slightly amplified while some pitching motion is also added on. For Case B, in addition to bending deformations in the y - z plane, there is also some bending deformation in the x - y plane, as in the previous situation. Furthermore, due to the effect of the increase in k_{θ_x, θ_z} , the bending in the y - z plane gives rise to a torsional deformation of the ballscrew. As a result, there is a slight increase in the yawing motion and pitching motions of the table, in addition to its already existing rolling motion. Furthermore, the frequency of the vibrations predicted by Case B is 3 [Hz] lower than that predicted by Case A.

C.5 Summary

This short study has helped to show, through simulations, that the cross-coupling terms contained in the screw-nut interface matrix derived in this thesis play an important role in the dynamics of ballscrew feed drives. It shows that these cross-coupling terms give rise to

motions on the table and ballscrew which cannot be predicted by the stiffness matrix derived by previous researchers which does not include these terms. This study is by know means exhaustive nor conclusive; however it gives a motivation towards a more detailed study on this topic, including validation through experiments.